

eman ta zabal zazu



Universidad
del País Vasco

Euskal Herriko
Unibertsitatea

Spin orbitronics in metals

Miren Isasa Gabilondo

Supervisor: Prof. Fèlix Casanova

2015

Laburpena

Elektronikaren sorrerak sekulako iraultza eragin du gaur egungo gizartean. Etxeko gailu xumeenetik hasi eta teknologiarik berrienaz hornituriko industria guneetaraino, ez dago elektroiaren karga gabe dabilen gailu elektrikorik. Aurrekaririk gabeko aldaketa honen eragile nagusia 1947. urtean asmatutako transistorea izan zen. Orduztik, transistorearen etengabeko miniaturizazioak zirkuitu integratu baten barruan unitate logiko gehiago sartzea ahalbidetu du eta ondorioz, gailu txikiago eta konplexuagoak eraiki dira urtetik urtera. Dena den, miniaturizazioak oinarritzko bi muga dauzka: batetik, gailuen etengabeko txikitzeak izugarritzko energi galerak dakartza Joule efektuarengatik eta bestetik, atomoen tamainura hurbiltzen garen heinean fluktuazio kuantikoek garrantzia haundiagoa hartzen dute. Hau dela eta, oinarri fisiko guztiz desberdina duen teknologia berri baten beharrea gaude elektronikaren alorrean aurrera pausua emateko. Honetarako hautagaietako bat *spintronika* da.

Spintronikak, edo *spin-elektronikak*, elektroiaren kargaz gain, haren spinaz baliztatzea du helburu informazioa garraiatzeko. Spina propietate kuantiko bat da eta fisika klasikoan parekorik ez badu ere, maiz bere inguruan biraka dabilen esfera kargatu batekin alderatu ohi da. "Biraketa" honen momentu angeluarra momentu magnetiko batekin lotuta dago, eta konkretuki, elektroiaren spinak bi balio posible soilik hartu ditzake: goranzko-spina eta beheranzko-spina.

Spintronika 1980. hamarkadan sortu zen magnetoresistentzia erraldoiaren aurkikutzarekin (GMR, ingelesetik). GMR-ak erresistentzia aldaketa nabarmen bat iragartzen du multigeruza magnetiko/ez-magnetiko batean eremu magnetiko bat aplikatzearen ondorioz. Hamar urteren buruan iada GMR-aren lehenengo aplikazio teknologikoa merkatuan zen ordenagailuetako disko gogorren irakurgailu gisa. Arrakasta azkar honek bultzatuta, spintronikak sekulako gorakada izan zuen zientzialarien artean eta aplikazio berriak agertu ziren, esate baterako, memoria magnetiko iraunkorrak (MRAM, ingele-

setik). Aipaturiko gailu elektriko hauek spin polarizatutako karga korronteak erabiltzen dituzte. Dena den, funtzionalitate handiagoa lortzeko, bigarren belaunaldiko gailuak behar dira eta hauek spin korronte puruak, kargarik gabeak, erabiliko dituzte.

Bigarren belaunaldiko gailu spintronikoetan ezinbesteko hiru osagai daude: (i) spin korronte puruak sortzea eta detektatzea, (ii) spin korronte puru hauek ahalik eta distantzia luzeenean garraiatzea eta (iii) manipulatzeko. Spin korronteak sortzeko modu eranginkorretako bat intrintsekoki goranzko-spin eta beheranzko-spin kopuru desberdina duten materialak erabiltzea da. Hau adibidez material ferromagnetikoetan (FM-etan) ematen da, truke elkarrekintzaren eraginez. Arrazoi honengatik elementu FM-ak askotan erabili izan dira spin korronte iturri gisa, horretarako teknika desberdinak erabiliz, esate baterako, spin injekzio termikoa, erresonantzia ferromagnetikoaren bidezko pompaketa edota spin injekzio elektrikoak. Tesi honetan azkeneko metodo hau erabiliko dugu, izan ere errezena da elektronika konbentzionalarekin partekatzen.

Dena den, material FM-en erabilera ez da spin korronteak sortzeko modu bakarra. Izan ere, spin-orbita akoplamentu (SOC, ingelesetik) indartsua duten material ez magnetikoak (NM, ingelesetik) erabil daitezke spin korronteen sorrera, detekzio eta manipulaziorako. SOC elektroien momentu angeluar orbitala eta spinaren arteko elkarrekintza da. Ikerketa lerro honek (*Spin orbitronika* deritzonak) azken urteotan sekulako gorakada izan du, izan ere material FM-ak eta hauekin batera erabili behar diren eremu magnetikoak ekiditeak teknologikoki abantaila handia ekarri dezake. SOC-an oinarritutako efektu asko aztertu ditu orain arte egoera solidoaren fisikak, Spin Hall efektua (SHE), Rashba-Edelstein efektua (REE), SOC-ek eragindako torkeak edo skirmioiak, besteak beste. Tesi honetan, SHE eta REE metaletan aztertuko ditugu.

Behin spin korronte purua sortutakoan garraiatu egin behar da. Dena den, elektroien spinak irauli egingo dira spin erlaxazio prozesu desberdinak direla medio, esate baterako, materialen ez-purutasunengatik, ale mugengatik edo fonoiekin eduki ditzaketen elkarrekintzengatik (ikus 2.1.1 atala). Honegatik, spin korronteek spin erlaxazio denbora eta distantzia jakin bat dute. Elektroiak bere spina kontserbatzen duen denborari, hau da, spina irauli aurretik ematen den denbora horri, spin erlaxazio denbora (τ_{sf}) deritzo. Bestetik, irauli aurretik material NM-an garraia daitekeen distantziari spin difusio luzera esaten zaio (λ_{NM}), eta honela erlazonaturik daude: $\lambda_{NM} = \sqrt{D\tau_{sf}}$.

Tesi honetan aurretik aipaturiko hiru metodo hauek (material FM-ak, SHE eta REE) aztertuko ditugu metal desberdinetan spin korronteak sortu, garraiatu eta de-

tektatzeko. Tesi guztian zehar hiru gailu mota desberdin erabiliko ditugu, horietako bi nanometro eskalan fabrikatuko ditugu eta bestea eskala mikrometrikotan. 3. kapituluak fabrikazio prozedurei buruzko azalpen orokor bat biltzen du eta gailu mota bakoitzaren deskribapen zehatzago bat ematen da A, B eta C Eranskinetan.

Lehenik eta behin, spin balbula lateralak (LSV, ingelesetik) erabiliko ditugu. Hauek spin korronteak elektrikoki injektatzeko gailurik erabilienak dira. LSV-ak bi elektrodo FM-z eta biak konektazen dituen kanal NM batez osaturik daude (Ikusi 1.1 Irudia). Beraz, kasu honetan elektrodoaren truke elkarrekintza erabiliko dugu spin korronteak sortzeko. LSV-ek honela funtzionatzen dute: lehenik eta behin spin polarizaturiko korronte elektriko bat injektatzen da elektrodo FM-tik (injektorea) kanal NM-ra. Material NM-an goranzko eta beheranzko spindun elektroikopuru berdina dagoenez, spin desoreka edo pilaketa bat sortuko da NM-an, FM/NM gainazalek gertu. Spin desoreka honek ezingo du betirako iraun eta beraz pilaturiko spinak difusio bidez injektore FM-aren bi aldeetarantz hedatuko dira, kanal NM-an, karga garraiorik ez dugun aldean spin korronte puru bat sortuz. Sistema orekatu aurretik, bigarren elektrodo FM bat jartzen badugu (detektorea), injekzio prozesuaren antzera, spin pilaketa bat gertatuko da bigarren NM/FM gainazalean eta boltaia gisa neurtuko dugu detektorean. Detektatutako boltaia positiboa izango da injektorea eta detektorea egoera magnetiko paraleloan badaude, eta negatiboa aldiz egoera antiparalelo batean badaude. Egoera paralelo eta antiparaleloen arteko desberdintasun honek bermatzen du detektaturiko boltaia spin pilaketarekiko sentikorra dela. Honez gain, LSV-en geometria ez-lokalak spin korronte eta karga korronteak desakoplatzea ahalbidetzen du, korronte elektrikoa eta boltaiaren neurketa espazialki bananduta daudelako. LSV-en funtzionamenduaren inguruko deskribapen zehatzago bat ematen da 2.1.1 atalean. LSV-ak kanal NM-aren spin garraio ezaugarriak, hau da λ_{NM} , eta elektrodo FM-en spin injekzio ezaugarriak neurtzeko erabili ohi dira.

Tesi honetan permalloy (Py, $\text{Ni}_{80}\text{Fe}_{20}$) eta zilarrez (Ag) egindako LSV-ak erabili ditugu. Lan honen funtsa Ag-aren spin garraio ezaugarriak hobetzea izan da, spin difusio luzeago bat lortu nahiean. Hobekuntza hori Ag-a epitaxialki haztean ikusi dugu, Ag polikristalinoarekin alderatuz: lehenengoak ale muga gutxiago izatean, spinak distantzia luzeagoan hedatu daitezke, $\lambda_{Ag} = 823$ nm-tan zehar hain zuzen. Hau Ag polikristalinoaren balioarekin konparatuz, $\lambda_{Ag} = 449$ nm, ia bikoiztu egiten dela ikus daiteke. Hau guztia 4. kapituluaz aztertutakoa da.

SHE spin korronte puruak sortu eta detektatzeko beste modu bat da. Efektua

hontan datza: korrante elektriko bat SOC indartsua duen material batean zehar hedatzen denean, spin korrante puru bat sortuko da, hasierako korrante elektrikoaren norabide perpendikularrean. Azken urteotan efektu honek indar handia hartu du experimentalki metaletan neurtzea lortu delako. Hala ere, jatorriz elementu FM-etan aspaldi aurkitutako Hall efektu anomaloaren parekoa da. Beraz, elementu FM-tan Hall efektu anomaloa eragiten duten mekanismo berdinek eragingo dute SHE material NM-tan. Mekanismo hauek gehienetan bi taldetan sailkatu ohi dira: (i) efektu intrinsekoak eta (ii) efektu extrinsekoak (ikus 1.3 Irudia). Efektu intrinsekoak, izenak berak dioen moduan, material NM-aren banden egiturarekin lotura duten efektuak dira. Mekanismo extrinsekoak berriz materialaren ez-purutasunekin edo fonoiekin lotura dute. Dena den, gehienetan SHE ezin da mekanismo bakar bati lotu, bi efektuen arteko konbinazio bat izango baita.

SHE experimentalki detektatzea ez da batere erraza, izan ere spin korranteek, korrante elektrikoek ez bezela, ez dute neurtzeko moduko boltaiarik sortzen. Horregatik, gehienetan alderantzizko spin Hall efektua (ISHE, ingelesetik) aztertu ohi da. ISHE-a SHE-aren aurkako prozesua gertatzean datza. Spin korrante puru bat material NM batean hedatzean, betiere SOC indartsua badu, korrante elektriko perpendikular bat sortuko da. Korrante hau, boltaia moduan neurtu ahal izango dugu. SHE-aren adierazgarri den parametro esanguratsu bat spin Hall angelua da, θ_{SH} , eta honek spin korrantea karga korrante bilakatzeko eraginkortasuna neurtzen du.

Tesi honetan ISHE neurtzeko spin balbula lateraletan oinarritutako spin absortzio (SA) gailuak erabili ditugu (Ikus 5.1(a) Irudia). Aurretik esan bezala, SHE agertu dadin SOC indartsua duten metalak behar ditugu. Tamalez, SOC indartsua duten metalek gehienetan spin difusio luzera motzak dituzte. Honela, spin korranteak garraiatzeko ona den materiala ez da egokiena izango spin korranteak sortu eta detektatzeko, eta alderantziz. Horregatik, aurretik aipatutako Ag ez da material aproposa SHE aztertzeko. Tesi honetan spin korranteak detektatzeko aukeratutako material NM-ak platinoa (Pt) eta urrea (Au) izan dira (5. Kapitulu). Alde batetik, Pt aukeratu dugu, SHE-a aztertzeko materialik erabiliena bada ere, eztabaida handia dagoelako bere spin Hall angeluaren inguruan. Bestetik, Au aztertu dugu SOC indartsua badu ere, nahiko spin garraio propietate onak dituelako. SA gailua LSV-en oso antzekoa da (ikus 2.1.2 Atala). Kasu honetan ordea, elektrodo FM bat erabiltzen da spin korrantea sortzeko baina detektatzeko erabiltzen den elektrodoa SOC indartsua duen material NM-a da. Bi elektrodo hauek λ_{NM} luzea duen material NM batez loturik daude, kobrea (Cu) gure kasuan.

LSV-etan bezela, elektrodo FM-tik (Py) Cu-zko kanalera spin korrante puru bat injeztatuko da. Spin korrantea Cu kanalean zehar garraiatuko da eta Au edo Pt elektrodora iristean spin korrantea karga korrante bilakatuko da SHE-aren eraginez. Honela, Au edo Pt elektrodoan boltaia bat neurtu ahal izango dugu. Tesi honetan spin Hall angelua tenperaturaren menpe aztertu dugu eta honela, SHE eragiten duten mekanismo desberdinak aztertzekeo gai izan gara. Ikusiko dugun moduan, Pt-an efektu intrinsekoak dira nagusi, Au-n aldiz efektu extrinsekoak. Gainera, Au-ren kasuan fonoiengatik agertzen den efektu extrinsekoa hauteman dugu lehenengo aldiz.

SHE-arekin lotuta, azken urteotan aurkitu den magnetoresistentzia berri bat ere aztertu dugu tesi honetan, spin Hall magnetoresistentzia (SMR) deritzona (7. Kapitulua). Magnetoresistentzia berri hau, SOC indartsua duen metal NM bat eta material FM isolatzaile (FMI) batez osaturiko bi geruzetako gailuetan ematen da. Magnetoresistentzia aldaketa honela ulertu daiteke: material NM-an karga korrante bat hedatzen denean, SHE dela eta spin korrante bat sortuko da honekiko perpendikular, spinaren orientazio jakin batekin, \vec{s} (ikus 1.7(a) Irudia). Spin korrante hau NM/FMI gainazalera iristean, \vec{s} eta FMI-aren magnetizazioa (\vec{M}) perpendikularrak badira, spin nahaste konduktantzia (G_r) dela eta spin korrantea xurgatu egingo da gainazalean, spinei eragindako momentuaren ondorioz (ikus 1.7(b) Irudia). \vec{s} eta \vec{M} paraleloak direnean ordea, spin korrantea isladatu egingo da, eta material NM-ra itzuliko da ISHE-arengatik karga korrante bilakatuz (ikus 1.7(c) Irudia). Horregatik, $\vec{s} \perp \vec{M}$ denean erresistentzia altuago bat neurtuko da, $\vec{s} \parallel \vec{M}$ denean baino. Bere jatorria dela eta, erresistentzia aldaketa hau zeharo sentikorra da NM/FMI gainazaleko ezaugarriekiko.

SMR efektuak duen gainazalarekiko sentikortasun honengatik, tesi honetan batetik NM/FMI gainazaleko G_r neurtzeko eta bestetik FMI-aren gainazaleko magnetizazioa aztertzekeo erabili dugu. Horretarako, Pt aukeratu dugu metal NM gisa eta CoFe_2O_4 (CFO) FMI bezala. G_r aztertzekeo CFO-a bi orientazio kristalografiko desberdinetan hazi dugu, (001) eta (111) norabideetan hain zuzen. Ondoren, honen gainean Pt *in-situ* edo *ex-situ* prozesuen bidez hazi dugu. Ikusi dugunez, *in-situ* prozesuak Pt/CFO gainazalaren kalitate hobea eskaintzen digu eta ondorioz erresistentzia aldaketa handiagoak neurtu ditugu. Horrez gain, G_r (001) norabidean (111) norabidean baino handiagoa da. Teknika honen bitartez gainera, CFO-aren gainazaleko magnetizazioa neurtzeko gai izan gara erresistentzia aldaketa soilik neurtuz. Beraz, SMR-ak sekulako abantaila eskaintzen du magnetikoki gogorrek diren FMI-en gainazalako magnetizazioa modu erraz baten neurtzeko. Honetarako erabiltzen diren gailuak orain arte

ikusitako LSV eta SA gailuen guztiz desberdinak dira. Izan ere, mikrometro eskalan eraikitako Hall barrak erabiltzen ditugu.

Azkenik, tesi honetan spin korronteak sortu eta detektatzeko aztertu dugun beste baliabideetako bat alderantzizko Rashba-Edelstein efektua (IREE, ingelesetik) izan da. Hau, SHE-aren antzera SOC-arengatik ematen da. Fenomeno honetan 3D-ko spin korronteak 2D-ko karga korrontea sortarazten du norabide perpendikularrean eta funtsean SOC-ak 2D sistemetan eragiten duen spin banden zabaltzetik dator (ikus 1.8(a) Iru-dia). Beraz, kasu honetan, 2D sistema aproposak aurkitu beharko ditugu efektu hau gauzatzeko. Sistema hauen artean semimetalak daude eta talde honetakoa den bismutoa (Bi) erabili dugu tesi honetarako. ISHE neurtzeko erabili dugun SA gailu berdina erabiliko dugu orain ere, baina oraingoan detektorea Bi barra bat izango da. Bertan spin korrontea karga korronte bilakatzeko eraginkortasuna neurtuko dugu, alderantzizko Rashba-Edelstein luzerarekin, λ_{IREE} . λ_{IREE} tenperaturaren menpe ikertuz, efektuaren jatorria aztertzeko gai izan gara. Hau guztia 6. Kapituluaz aztertu dugu.

Gure ustez, tesi honetan aurkeztutako emaitzek interes handia dute spintronika eta spin orbitronikaren alorretan dabiltzan zientzialarientzat. Hemen aurkezturiko il-dotik segita aurkikuntza interesgarri ugari atera daitezke spin korronte puruak erabiliko dituzten gailu berrien garapenerako.

Abstract

Spintronics is a rapidly growing area of research which enables performing electronics with the spin of the electron. The interest on the field arised from its huge potential to overcome the problems of the continuous miniaturization that silicon-based electronics is facing . The first successful spintronic applications came with the hard-disk read heads and the magnetic random access memories, based on the giant magnetoresistance and tunnel magnetoresistance effects, respectively. These are known as first-generation spintronic devices and exploit spin-polarized currents where no direct spin manipulation is involved. However, for second-generation and more sophisticated spin-based devices, pure spin currents are needed, a flow of spin angular momentum without net charge flow.

A possible approach to generate and detect spin currents is using materials that intrinsically have different amount of spin-up and spin-down electrons, for example, ferromagnetic (FM) metals. In these materials, spin currents can be generated thermally, electrically or by spin pumping. The generated spin current is then injected into a non-magnetic (NM) channel where the spin current diffuses over a given distance and it is detected with a second FM metal using any of the reciprocal effects used for the injection. The prototypical device that involves the idea of spin injection, transport and detection is the lateral spin valve (LSV). It is the most common spintronic device and its non-local geometry, where the current excitation path and the voltage probes are spatially separated, enables to decouple charge from spin currents.

Another very promising approach is to use the spin Hall effect (SHE). This effect is the anomalous Hall effect, well known in ferromagnets, but which also occurs in materials with strong spin-orbit coupling (SOC). In this phenomenon, it is observed that when an unpolarized charge current flows in a metal with strong SOC, the spin-up and spin-down electrons are deflected in opposite direction. This deflection causes a

spin accumulation at the edges of the metal, resulting in a pure spin current in the transverse direction. From the SHE, the reciprocal effect can be deduced, in which a charge current is created from the flow of a pure spin current. This reciprocal effect is known as the inverse SHE (ISHE). The main technological advantage of using a NM metal to create and detect pure spin currents is that external magnetic fields and FM elements can be avoided.

In this work, we have studied both approaches for the generation and detection of pure spin currents. First, LSV devices have been fabricated using permalloy (Py, $\text{Ni}_{80}\text{Fe}_{20}$) as the FM electrodes and silver (Ag) for the NM channel. Here we show that a careful epitaxial growth of Ag largely suppress the grain boundary contribution and enables to enhance the spin transport properties compared to polycrystalline Ag.

The spin-to-charge current conversion is the core of this work and it has been studied in platinum (Pt), gold (Au) and bismuth (Bi) using the spin absorption technique in a LSV geometry. With this technique, we measured the spin Hall angle (the efficiency to convert spin into charge current) in Pt and Au. Moreover, its evolution with temperature allows us to identify the dominant scattering mechanisms behind the SHE. We have observed that, whereas the intrinsic mechanism dominates in Pt, extrinsic effects are more relevant in Au, including a previously ignored phonon contribution to skew scattering.

The spin-to-charge current conversion in Bi is more intriguing: in this case, we observe that spin currents are strongly absorbed at the metallic-Bi surface, creating a 2D charge current due to the inverse Rashba-Edelstein effect (IREE). By analyzing the IREE as a function of temperature, we are able to determine the origin of the effect, which arises from the spin-splitting of the non-monotonic dispersion of the surface states at the Fermi level. We further support the experimental evidence with a theoretical analysis.

Finally, we have studied the newly discovered spin Hall magnetoresistance (SMR) in Pt/ CoFe_2O_4 (CFO) bilayers. The SMR arises from the simultaneous effect of SHE and ISHE in the NM (Pt in our case) in combination with the interaction of the generated spin current with the ferromagnetic insulator (CFO in our case). Depending on the magnetization orientation of the FMI, this spin current will be absorbed or reflected at the NM/FMI interface yielding a change in the resistance. Due to the origin of the effect, the SMR is very sensitive to the quality of the NM/FMI interface. Therefore,

measuring the magnetoresistance of the NM material can give information not only about the spin-to-charge conversion properties of the NM spin Hall effect, but also about properties at the interface, such as the spin-mixing conductance (G_r). We have made a systematic analysis changing the Pt growth conditions, being *in-situ* or *ex-situ*, and the surface orientation of the CFO, being (001) or (111). From this analysis we observe that the change in magnetoresistance is larger for *in-situ* samples due to the optimal preparation conditions of the interface. Moreover, G_r is larger for the (001) orientation compared to the (111) orientation, which means that it is strongly affected by the atomic configuration of the magnetic atoms at the interface. Additionally, the magnetic properties of the CFO films are compared to the magnetoresistance of Pt/CFO bilayers. Data shows that field-dependent SMR, although reminiscent of the bulk magnetization process, contains distinctive features. We claim that they reflect the surface magnetization of CFO films, which, as typical of spinel ferrites, largely differs from bulk. Therefore, SMR can be used as a probe for complex surface magnetization that cannot be detected with standard techniques.

Contents

Laburpena	i
Abstract	vii
1 Introduction and state-of-the-art	1
1.1 Spintronics	1
1.1.1 Historical perspective	2
1.1.2 Spintronic devices	3
1.2 Spin orbitronics	5
1.2.1 Spin Hall effect	6
1.2.2 Rashba-Edelstein effect	21
1.2.3 Spin-orbit torques	22
1.3 This thesis	23
2 Multiterminal non-magnetic/ ferromagnetic structures	35
2.1 Non-local-based devices	35
2.1.1 Lateral spin valves	35
2.1.2 Spin absorption devices	44
2.1.3 Spin Hall devices	47

2.1.4	Inverse Rashba-Edelstein devices	51
2.2	Hybrid NM/FMI bilayers	52
3	Experimental techniques	59
3.1	Fabrication of devices	59
3.1.1	General procedure	59
3.1.2	Our devices	67
3.2	Characterization techniques	68
3.2.1	Electrical characterization of devices	68
3.2.2	X-ray diffraction	71
3.2.3	Scanning electron microscopy	73
4	Spin transport in Ag	77
4.1	Thin film growth and characterization	78
4.2	Device fabrication	78
4.3	Results	80
4.4	Conclusions	82
5	Spin transport and spin Hall effect in Au and Pt	85
5.1	Fabrication	86
5.2	Spin transport properties	86
5.3	Spin Hall effect	88
5.3.1	Possible role of spin memory loss	91
5.3.2	Mechanisms contributing to the SHE	93
5.4	Conclusions	97
6	Inverse Rashba-Edelstein effect in Bi	103

<i>CONTENTS</i>	xiii
6.1 Fabrication	104
6.2 Spin absorption at the interface	104
6.3 Inverse Rashba-Edelstein effect	105
6.3.1 Experimental characterization	105
6.3.2 Theoretical analysis	107
6.4 Is it possible to have inverse spin Hall effect?	110
6.5 Conclusions	111
7 Spin Hall magnetoresistance	115
7.1 Fabrication	116
7.2 Electrical characterization	117
7.3 Occurrence of SMR	117
7.4 Spin-mixing conductance	118
7.4.1 <i>Ex situ</i> vs <i>in situ</i>	120
7.4.2 (001) vs (111)	120
7.5 Ordinary magnetoresistance of Pt	122
7.6 Sensing CFO surface magnetization	127
7.7 Conclusions	129
8 Conclusions and future perspectives	135
Appendix A Fabrication parameters for LSVs	141
A.1 First step: NM channel	141
A.2 Second step: FM electrodes	143
Appendix B Fabrication parameters for SA devices	145
B.1 First step: FM electrodes	145

B.2	Second step: MS wire	146
B.3	Third step: NM channel	147
Appendix C	Fabrication parameters for FMI/NM bilayers	151
C.1	Ex-situ samples	151
C.2	In-situ samples	152
	List of publications	155
	Acknowledgements	157

Chapter 1

Introduction and state-of-the-art

The utilization of electron charge has revolutionized our everyday life, yielding a series of changes and advances that have modified all the branches of society. The key invention that enabled this revolution was the transistor, discovered in 1947, being a crucial device for the development of the field of electronics and later on the field of information technology. Since then, the continuous miniaturization of the transistor size has allowed packing more logics in a smaller integrated circuit, leading to more complex and smaller devices and to the corresponding progress that this brings. However, the decrease in the transistor size is reaching a limit in which intolerable ohmic energy dissipation values are achieved and quantum effects inevitably start to be present. At this stage, further significant progress can only be reached with a new class of technology based on completely new physics. One of the candidates is spintronics [1].

1.1 Spintronics

Spintronics, also known as *spin electronics*, takes advantage not only of the charge of the electron, but also of its spin degree of freedom to carry information. The spin is a quantum mechanical property that describes the intrinsic angular momentum associated with an electron. Although it does not have a classical analogue, it is often visualized as a spinning sphere of charge. The angular momentum of this "spinning" is associated with a magnetic moment, giving the spin a direction which can only take two possible values, the so-called "spin-up" and "spin-down" states.

1.1.1 Historical perspective

The birth of spintronics dates back to the late 1980s with the discovery of the giant magnetoresistance (GMR) by Albert Fert and Peter Grünberg [2, 3]. They observed that, under an applied external magnetic field, there was a large change in the electrical resistance of a multilayered metallic structure. This structure is commonly known as spin valve, and it is composed of alternating ferromagnetic and non-magnetic conductive layers. The electrical resistance through this multilayer depends on the relative magnetization of the ferromagnets. When the magnetizations of the ferromagnetic layers point parallel to each other, the resistance is lower due to the spin-dependent scattering of the minority electrons only. However, when the magnetizations of the ferromagnets are in an antiparallel state, both majority and minority electrons scatter, resulting in a higher resistance. These two resistance states can be used to detect ("read") small magnetic fields such as the ones created by the magnetic bits of a hard drive. Not even ten years after this discovery, the first technological application of the GMR was already in the market as hard-drive read heads.

This early success of spintronics encouraged the scientific community to keep on researching new phenomena that could exploit the spin degree of freedom in devices in order to improve their efficiency and expand their functionality [4]. In this effort, a similar system was constructed using an electrical insulator in between two ferromagnetic layers, which is known as a magnetic tunnel junction (MTJ). The effect arising in these type of devices is called tunneling magnetoresistance (TMR) [5, 6] and it is based on the fact that spin is conserved during tunneling. It was observed that the performance of a MTJ is much better than the one observed in all-metallic GMR devices, as it enabled higher resistance changes. One of the most important applications of MTJs came with non-volatile magnetic random access memories (MRAM), where information can be stored with the two resistance states ("0" and "1"), which can be written and read electrically. For reading, the magnetoresistance in the MTJ is measured. Writing is a more indirect process in which Oersted fields are used. These fields are generated by passing an electrical current through a conductor adjacent to the bit that needs to be written. If the generated field is high enough, it will switch the magnetization of one of the ferromagnetic layers in the MTJ. This is the way in which the information is written in a magnetic bit. The major problem of this approach is that the current needed for writing increases with decreasing the size of the device, limiting the downscaling.

An alternative to the writing problem came when the prediction of spin-transfer torque (STT) [7,8] was combined together with MRAM technology, giving rise to STT-MRAM. STT is an effect by which a spin-polarized current modifies the magnetization of a ferromagnetic layer. If a charge current is sent through a MTJ, the first ferromagnetic layer will spin polarize the charge current. This spin-polarized current will tunnel through the insulating layer and will transfer its angular momentum to the second ferromagnetic layer of the MTJ, exerting a torque that might be sufficiently strong to switch the magnetization. This makes the STT-MRAM a very promising approach to shrink the device dimensions, to have a faster switching between two memory states and to lower the power dissipation compared to the conventional MRAM [9].

All these cited devices exploit spin-polarized currents where no direct spin manipulation is involved. However, a second generation of spintronic devices is now envisioned in which pure spin currents, a diffusive flow of spins with no net charge flow, are used instead [10]. Emerging research devices include the recently proposed concept of all-spin logics [11], which uses magnets to represent non-volatile binary data while the communication between magnets is achieved using spin currents in spin coherent channels; or the long sought spin transistor [12], which presents variable current drivability controlled by the spin direction of the carriers and non-volatile information storage using the magnetization configuration. These features are very useful functionalities for energy-efficient, low-power circuit architectures unachievable by ordinary charge-based information processing.

1.1.2 Spintronic devices

To fulfill the impressive predictions explained above, a higher level of sophistication has to be achieved. In particular, several key ingredients are needed to operate a successful spintronic device: (i) to generate and detect pure spin currents, (ii) to transport these spin currents through long distances and (iii) being able to manipulate them.

The first attempt to create spin currents, relied on the optical spin injection technique [13–15]. This can be used in certain semiconducting materials, in which spin-polarized electrons are accumulated in the conduction band when they are optically excited from the valence band with a circularly polarized light [16] (see Fig. 1.1). However, an alternative approach is needed for the case of metals. A very convenient way to generate spin currents is using materials that intrinsically have different amount

of spin-up and spin-down electrons. This is the case of ferromagnetic materials that, due to exchange interaction, have different spin populations at the Fermi level. For this reason, ferromagnets have been widely used as a spin source and different approaches have been explored, such as thermal spin injection [17, 18], spin pumping [19, 20] or electrical spin injection [21–24] (see Fig. 1.1). The latter offers a more attractive platform to combine it with conventional electronics and, thus, exhaustive studies have led to a big progress in the field.

Once the spin current is created by any of these means, it is injected into a non-magnetic metal [21–28], a semiconductor [29–31] or to a carbon-based material [32, 33] where the spin current diffuses over a given distance and it is detected using any of the reciprocal effects used for injection (optical detection [14, 15, 34], electrical detection [21–24], spin-transfer torque [35, 36] or thermal detection [37, 38], see Fig. 1.1). Manipulating the spin information is also an important feature in spintronic devices, which can be done by applying a magnetic field, *via* Hanle effect [39, 40], or by electric fields [41]. The latter exhibits a fundamental limitation because, in order to achieve spin manipulation with electric fields, strong spin-orbit coupling is needed. However, the best materials for spin transport are those with the lowest spin-orbit interaction. Therefore, although there are few exceptions [42], transporting and electrically manipulating spins in the same environment remains elusive.

This basic idea of having a ferromagnetic injector, a non-magnetic channel and a ferromagnetic detector gives rise to a widely studied spintronic device: the lateral spin valve (LSV). This is a very powerful tool to characterize the spin transport properties of non-magnetic materials, as well as to determine the spin injection efficiency of different ferromagnetic metals. The particularity of this device is its geometry, as it enables to decouple the charge and spin currents by performing non-local measurements. This means that when the charge and spin current, that flow together in the ferromagnet as a spin-polarized current, reach the non-magnetic metal, they are separated and a pure spin current can be achieved in the non-magnet. This is a very important advantage because pure spin currents allow us to probe spin-dependent phenomena without the spurious effects that charge currents can bring. Further details on how LSVs work will be given in Chapter 2.

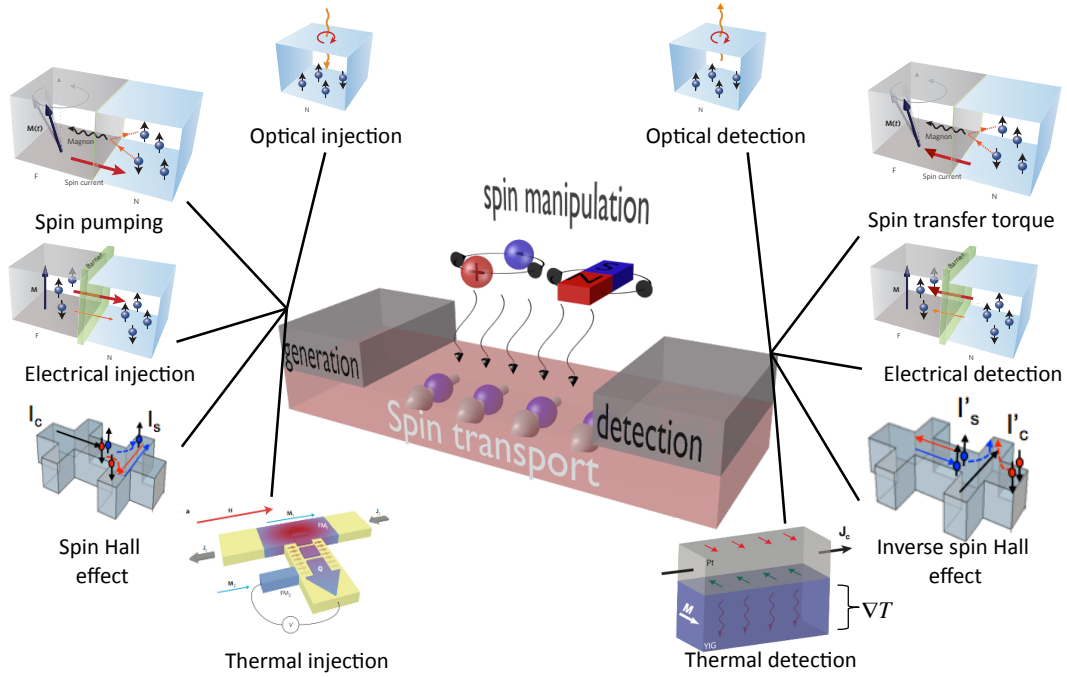


Figure 1.1: Sketch with key ingredients for the performance of a spintronic device: (i) Generation and detection of pure spin currents by different methods; (ii) Spin transport; (iii) manipulation of the transported spin information by electric or magnetic fields. Fig. adapted from Refs. [17], [37] and [43].

1.2 Spin orbitronics

An alternative approach to create, detect and manipulate spin currents is by exploiting the spin-orbit coupling (also known as spin-orbit effect or spin-orbit interaction). This is a relativistic effect in which a particle's motion interacts with its spin. This interaction will shift an atomic energy level due to the electromagnetic interaction between the electron's spin and the magnetic field generated by the electron's orbit around the nucleus. The splitting of the energy levels does not exclusively arise from electrons orbiting an atom but it can also be present when electrons are moving through a crystal lattice. In this case, the characteristic band structure of the solid will be affected by the atomic spin-orbit coupling, resulting in a splitting of the spin subbands. As we will see, this mechanism may allow us to control the spin degree of freedom in a solid, without the presence of external magnetic fields or ferromagnetic materials. Therefore, the non-magnetic material that remained as a passive element for spin current transport in conventional spintronics takes a more active functionality creating and detecting pure

spin currents. This novel direction of spintronics is known as *spin orbitronics* [44].

Spin-orbit effects have been studied for a long time in solid state physics [45, 46] and this has settled a solid basis for the current application of spin-orbit coupling into spintronics. The increasing interest of the scientific community is giving rise to very exciting phenomena that exploit the spin-orbit interaction, such as the spin Hall effect [47–51], the Rashba-Edelstein effect [52–54] or the spin-orbit torques [55–57]. In the following, we will make a more exhaustive description of these effects.

1.2.1 Spin Hall effect

The spin Hall effect (SHE) is a phenomenon that results from spin-orbit interaction. It predicts that if a charge current flows in a non-magnetic material with a strong spin-orbit coupling, a spin current, perpendicular to the original charge current, will be created. The SHE is currently gaining considerable attention. However, its origin is very closely related to the Hall effect in ferromagnets, *i.e.*, the anomalous Hall effect (AHE), known from the early 1880s.

Edwin H. Hall discovered in 1879 that in presence of an out-of-plane magnetic field, \vec{H} , the current density flowing in a conductor, \vec{j}_c , experiences a Lorentz force that pushes the electrons towards the edge of the conductor with a certain velocity [58]. This causes a charge imbalance between opposite edges that results in a measurable transverse electric field, \vec{E} , perpendicular to \vec{j}_c and \vec{H} (Fig. 1.2 (a)):

$$E_x = \rho_{xy} j_{c,y}, \quad (1.1)$$

where the transverse resistivity, ρ_{xy} , is proportional to the applied magnetic field:

$$\rho_{xy} = R_0 H \quad (1.2)$$

and R_0 is the Hall coefficient, a material dependent constant, which basically depends on the carrier concentration. Equation 1.1 can also be written in terms of the transverse conductivity, σ_{xy} , as:

$$j_{c,x} = \sigma_{xy} E_y \quad (1.3)$$

σ_{xy} and ρ_{xy} are related by the longitudinal resistivity, ρ_{xx} , or the longitudinal conductivity, σ_{xx} , in the following way:

$$\rho_{xy} = -\frac{\sigma_{xy}}{\sigma_{xy}^2 + \sigma_{xx}^2} \approx \frac{\sigma_{yx}}{\sigma_{xx}^2} = \sigma_{yx}\rho_{xx}^2 \quad (1.4)$$

Few years later, in 1881, Hall [59] discovered that for the particular case of ferromagnetic materials, there was an additional contribution to the transverse voltage that appears without the presence of a magnetic field, but was related to the magnetization of the ferromagnet, \vec{M} , the so-called anomalous Hall effect (AHE) (Fig. 1.2 (b)).

In 1929, a phenomenological equation for the Hall resistivity, which included both the Hall effect and the AHE, was proposed by Smith and Sears [60]:

$$\rho_{xy} = R_0 H + \rho_{AH} \quad (1.5)$$

where $\rho_{AH} = R_S \mu_0 M$, being R_S the anomalous Hall coefficient and M the out-of-plane magnetization of the system. Although this equation was successful to describe the observed AHE in many FM materials, it did not offer a microscopic interpretation of the effect.

The origin of this contribution was unclear for more than 70 years and it was a matter of debate, until Karplus and Luttinger pointed out its connection to spin-orbit coupling [61]. They suggested that electrons flowing through the ferromagnet acquire a transverse velocity between scattering events, being opposite for spins with different orientation. Since, in a ferromagnetic material, there are more spins of a given orientation, a spin-dependent transverse velocity gives rise to a transverse voltage. Nowadays, this mechanism is identified as the intrinsic mechanism of the AHE. Some years later, skew-scattering and side-jump scattering mechanisms were proposed by Smit [62] and Berger [63], respectively. In these cases, the transverse displacement is generated during the scattering with impurities and are thus extrinsic mechanisms.

It was only in 1971 that Dyakonov and Perel suggested that these mechanisms should also be present in non-magnetic materials [45]. However, as the amount of spin-up and spin-down electrons is the same in a non-magnetic material, there is no charge accumulation at the edges of the conductor, but only spin accumulation (Fig. 1.2 (c)). This effect results in a transverse spin current and was named by Hirsch as "spin Hall

effect" in 1999 [64]. In this case, the transverse resistivity will only depend on the spin-orbit coupling of the material:

$$\rho_{xy} = \rho_{SH} \quad (1.6)$$

For many years, the concept of SHE remained as a theoretical extension of the AHE for non-magnetic materials, and it did not get much attention until Hirsch revisited the SHE in 1999 [64]. This novel interest in the subject pushed the experimentalists, who observed evidences first in semiconductors [65], and shortly after in metals [66–68]. In this work we will focus on metals, as the SHE is expected to be stronger [49].

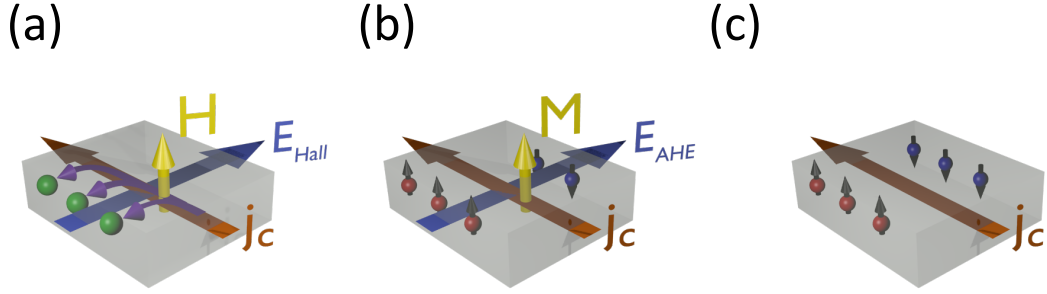


Figure 1.2: (a) The Hall effect, where electrons are deflected to an edge of the conductor due to an external magnetic field, creating a transverse Hall voltage. (b) The anomalous Hall effect in a ferromagnet, where spins with different orientations are deflected to opposite edges. This introduces an additional contribution to the transverse voltage because the number of spin up and spin down electrons is not the same, leading to a charge imbalance. (c) The spin Hall effect in a non-magnetic material, where, in absence of an external magnetic field, spins with different orientation are deflected to opposite edges due to spin-orbit coupling. As the number of spin-up and spin-down electrons is the same in a non-magnetic material, a spin accumulation is created, but not charge accumulation.

Phenomenological description of the SHE

Studying the physical origin behind the AHE has been a lively area of research since the 1950s. Nowadays, it is known that the spin-orbit interaction arises from a variety of mechanisms which can be either intrinsic or extrinsic. The main difference between both mechanisms is that if the displacement of spin-up and spin-down electrons occurs during a scattering event, it will be an extrinsic contribution, and if the displacement occurs in between scattering events, it will be an intrinsic contribution. Most of the work to determine the different contributions has been done for the AHE in ferromagnets. However, as the SHE borrows the physics from the AHE, it is possible to describe

both effects by the same mechanisms. The theoretical understanding of the AHE has been surrounded by a big controversy from the very beginning. Lately, a more unified description is emerging [69–71]. In the following, we are going to list and describe the different contributions acting on the AHE. Afterwards, we will focus on the studies which have been done for the SHE.

1. Intrinsic effects

This mechanism (Fig. 1.3(a)) was first proposed by Karplus and Luttinger [61] and it is closely related to the spin-dependent band structure of the material. Its contribution to the anomalous Hall resistivity scales with the resistivity of the material, ρ_{xx} , in the form of $\rho_{AH} = -\sigma_{AH}^{intr} \rho_{xx}^2$, where σ_{AH}^{intr} is a constant value. This clearly shows that the anomalous Hall conductivity will only depend on the band structure. What makes this contribution quite unique is that it is proportional to the integration of the Berry curvature of each occupied band over the Fermi sea [70]. Therefore, it can be reformulated in terms of Berry curvature [72].

2. Extrinsic effects

There are two different extrinsic mechanisms:

(a) Skew scattering

The skew-scattering mechanism was a contribution proposed by Smit [62], in which the idea of a spin-dependent scattering cross section was supported. This means that, when a given spin reaches the scatterer it will be scattered towards or away of the scattering center depending on the spin orientation (Fig. 1.3 (b)). Regarding its contribution to the anomalous Hall resistivity, it scales linearly with the residual charge resistivity, ρ_{xx0} , as $\rho_{AH} = a_{ss} \rho_{xx0}$. Note that ρ_{xx0} is the resistivity due to static impurities at low temperature.

(b) Side jump

The side-jump mechanism was introduced by Berger [63], where he suggested that, during the scattering, spin-up and spin-down electrons would be deflected to the same direction, but due to the spin-dependent acceleration or deceleration, electrons with opposite spin would be displaced to opposite directions. Therefore, consecutive scattering events would be capable of generating a transverse spin current (Fig. 1.3 (c)). Its contribution to the anomalous Hall resistivity is quite different to the skew scattering, as

it scales with the square of the residual charge resistivity: $\rho_{AH} = a_{sj}\rho_{xx0}^2$. Therefore, higher impurity concentrations would lead to a larger contribution of the side-jump mechanisms. However, it seems that distinguishing this contribution is a very challenging task, as side jump mechanism depends on details of disorder of a particular material which are usually unknown [70].

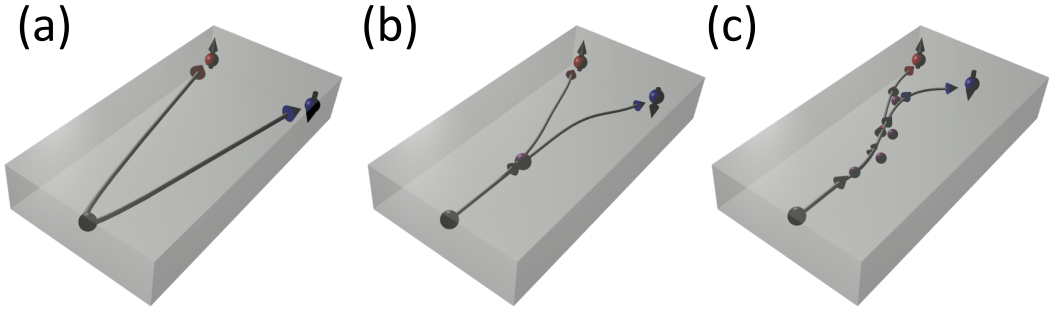


Figure 1.3: Contributions to the anomalous Hall effect. (a) Intrinsic contribution, where spin-up and spin-down electrons are displaced between scattering events. (b) Extrinsic skew-scattering contribution, where a scatterer deflects spin-up and spin-down electrons in opposite directions, creating a transverse spin current. (c) Extrinsic side-jump contribution, where consecutive scattering events are capable to generate a transverse spin current.

In general, the AHE cannot be ascribed to a particular mechanism, but it will be a combination of more than one mechanism acting simultaneously. Recently, a unified scaling law, where all the contributions are taken into account, has emerged [69]:

$$\rho_{AH} = a_{ss}\rho_{xx0} + a_{sj}\rho_{xx0}^2 - \sigma_{AH}^{intr}\rho_{xx}^2 \quad (1.7)$$

$$\sigma_{AH} = -a_{ss}\frac{\sigma_{xx}^2}{\sigma_{xx0}} - a_{sj}\frac{\sigma_{xx}^2}{\sigma_{xx0}^2} + \sigma_{AH}^{intr} \quad (1.8)$$

where a_{ss} , a_{sj} and σ_{AH}^{intr} are the skew-scattering, side-jump and intrinsic constants, respectively, ρ_{xx} (σ_{xx}) is the longitudinal resistivity (conductivity) and ρ_{xx0} (σ_{xx0}) is the residual resistivity (conductivity).

The same scaling law (Eqs. 1.7 and 1.8) can also be used to explain the origin of the SHE in metals. However, in this case the scaling will be given by ρ_{SH} or σ_{SH} . Long standing theoretical debates about the different contributions [73–75] have been, in most cases, further supported by experimental evidence [76–78].

For instance, it was theoretically predicted that the intrinsic SHE should be proportional to the spin-orbit coupling at the Fermi level, $\langle l \cdot s \rangle_{FS}$, so that:

$$\sigma_{SH}^{intr} \approx \frac{e}{4a} \frac{\langle l \cdot s \rangle_{FS}}{\hbar^2} \quad (1.9)$$

where a is the lattice constant. Therefore, according to Hund's rule, in transition metals with more than half filling of the d-bands, σ_{SH}^{intr} should be positive, as it is the case of Pt, Pd or Au (see Fig. 1.4). On the contrary, those metals with less than half filling of the d-orbitals, such as Ta or W, σ_{SH}^{intr} should be negative (see Fig. 1.4) [73]. This was experimentally observed by Morota and coworkers [76], where a large variety of transition metals were systematically studied.

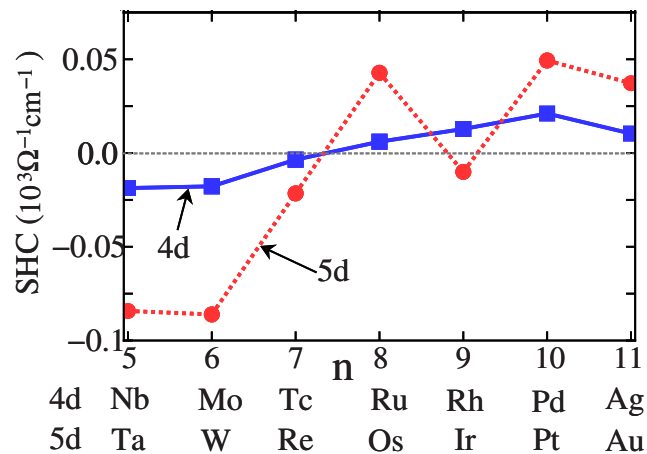


Figure 1.4: Intrinsic spin Hall conductivity values for different 4d and 5d transition metals calculated theoretically by taking account their realistic band structure with a tight-binding model. Taken from Ref. [73].

The extrinsic contributions, specially those related to the skew-scattering mechanisms, have also been analyzed by first-principles calculations. Gradhand and coworkers [75] observed that the spin Hall conductivity of a given host material could be easily tuned choosing the correct impurities for each host, as the magnitude of the effect depends on the difference between the spin-orbit couplings of the host material and the impurities. The most convenient cases to obtain a large SHE are those in which heavy atoms host light impurities, or the other way around, light atoms host heavy impurities. The latter has been experimentally proven [77, 78], where the SHE in a Cu host with Bi or Ir impurities was analyzed. In these works, they first showed that Cu itself does not

have a measurable SHE, however, when it is slightly doped with a heavy impurity (Ir or Bi), they can achieve a very efficient conversion of spin current into charge current, *i.e.*, a large SHE.

The extrinsic contributions related to side-jump mechanism are more difficult to determine because, as in the case for the AHE, this contribution depends on disorder details of a particular material. Since it is closely related to the impurity concentration, high enough concentration could make the side-jump mechanism dominate over the rest. However, to the best of our knowledge, this has not been reported yet.

Up to now, a complete analysis similar to the one done for the AHE by Tian *et al.* [69] or Hou *et al.* [71] is still missing for the SHE. However, in Chapter 5 of this thesis we will analyze the different contributions of the SHE in different metals.

Experimental quantification of the SHE

The experimental characterization of the SHE is quite difficult because spin currents do not give rise to a measurable voltage (see Fig. 1.2(c)). Therefore, the inverse spin Hall effect (ISHE) is usually studied instead. This is the reciprocal effect to the SHE and, therefore, it predicts that a spin current flowing through a non-magnetic conductor will create a transverse charge current:

$$\vec{j}_s = \frac{\sigma_{SH}}{\sigma_{xx}} \frac{\hbar}{2e} \vec{j}_c \times \vec{s} \quad (1.10)$$

$$\vec{j}_c = \frac{\sigma_{ISH}}{\sigma_{xx}} \frac{\hbar}{2e} \vec{j}_s \times \vec{s} \quad (1.11)$$

where $\sigma_{SH,ISH}$ are the spin Hall and inverse spin Hall conductivities. $\vec{j}_{c,s}$ are the charge and spin current densities and \vec{s} is the spin polarization. According to Onsager reciprocity relations [79], $\sigma_{SH} = \sigma_{ISH}$. In Eqs. 1.10 or 1.11, the parameter that quantifies the efficiency of a metal to convert spin current into charge current or viceversa is given by $\frac{\sigma_{SH}}{\sigma_{xx}}$ and it is known as the spin Hall angle:

$$\theta_{SH} = \frac{\sigma_{SH}}{\sigma_{xx}} = -\frac{\rho_{SH}}{\rho_{xx}}. \quad (1.12)$$

Usually, the spin current is created using different techniques where ferromagnetic materials are involved and this spin current is converted into a charge current due to

ISHE in the metal of interest. Note that, in a standard open circuit measurement, the charge current generated by the ISHE will result on a charge accumulation and, consequently in a measurable voltage.

In order to prepare the experimental set up to detect the SHE or its inverse, it is important to take into account the symmetry of the effect. From Eqs. 1.10 or 1.11, one can notice that the original spin (charge) current, the generated charge (spin) current due to ISHE (SHE) and the spin polarization will always be mutually perpendicular.

In the following, we are going to describe the different techniques.

1. Spin pumping

This technique takes the advantage of the magnetization dynamics of a ferromagnetic layer. Basically, it operates as follows. First, a magnetic field is applied so that all the spins in the ferromagnet are aligned along this direction (\hat{y} direction, in Fig. 1.5(a)). Then, the ferromagnet is brought into ferromagnetic resonance (FMR) with an *ac* magnetic field, causing its magnetization to precess and resulting in an emission of a *dc* spin current to the adjacent non-magnetic layer (along \hat{z} direction) [19, 20]. In this layer, due to the ISHE, a charge current perpendicular to the spin orientation and the spin current is created, giving rise to a charge accumulation and therefore to a measurable voltage (along \hat{x} direction) (Fig. 1.5(a)) [80, 81].

There are several advantages that make spin pumping a very interesting technique. One of the benefits is related to the geometry of the device. As only a ferromagnetic/non-magnetic bilayer is required for the detection of ISHE, complex fabrication processes can be avoided. Moreover, spin pumping allows the generation of spin currents over large areas and therefore large spin Hall voltages can be measured. Another strength of the technique is that, since the spin injection is achieved by magnetization dynamics, the conductivity-mismatch problem can be avoided. This problem is present when the spin injection arises from a charge transport through an interface formed by materials with considerably different conductivities [82]. Last but not least, ferromagnetic insulators (FMI) can be used to create the spin currents [83–86]. Using this type of materials ensures that the detected charge current can only have its origin in the ISHE of the NM layer, as electrical conduction is prevented along the FMI.

However, there are also some disadvantages for the spin-pumping technique that

should be taken into account. One of the most controversial aspects is that the quantification of the effect is still not clear [87]. Another issue is that, due to the proximity of the NM layer to the FM layer, a ferromagnetic ordering can appear in the atomic layers of the NM near the interface. This effect, known as magnetic proximity effect, will generate an additional damping to the magnetization dynamics [88, 89].

2. Spin-transfer torque

This technique is very similar to the spin-pumping technique, but it exploits the opposite effect. In this case, a *dc* charge current is sent through the non-magnetic layer (\hat{x} direction in Fig. 1.5(b)) and, due to the SHE, a *dc* spin current will be created (\hat{z} direction). When this spin current reaches the adjacent ferromagnet, the spin angular momentum from the non-magnetic material (pointing in \hat{y} direction) will be transferred and this will make the magnetization to precess [36] (Fig. 1.5(b)). The change in the magnetization is detected by FMR. As the spin-transfer torque (STT) changes the damping of the FMR, by measuring the resonance line shape one can determine the magnitude of the spin current that generated the torque. Given that the original charge current and the generated spin current due to SHE are known, the spin Hall angle can be determined.

As this technique is basically the opposite to the previously explained spin-pumping technique, they will share the same advantages and disadvantages. However, the spin-transfer torque has two additional drawbacks. One is that the detected line width is usually small. This makes STT a suitable technique just for metals with large spin Hall angles. The other issue is that the origin of the torque is currently a matter of debate among the scientific community. Some state that the torque is induced via SHE [55, 56], whereas others argue that it is due to Rashba effect [57]. This will be further explained in Section 1.2.3.

An alternative to the conventional STT is to use a microwave frequency (r.f.) charge current through the bilayer [35]. As a consequence, a r.f. spin current will be generated in the NM by the SHE and will result in an oscillating torque in the adjacent FM. This torque induces a magnetization precession that leads to a time varying anisotropic magnetoresistance (AMR) of the FM. From the mixing of this oscillating AMR and the r.f. charge current, a measurable *dc* voltage signal will be generated across the sample due to the spin-torque diode effect [35]. From this voltage, a quantitative measure of the spin current generated by the NM and,

consequently the spin Hall angle, can be obtained. This technique is known as spin-torque ferromagnetic resonance (ST-FMR) and its main advantage compared to conventional STT is that a better accuracy can be achieved when determining the spin Hall angle.

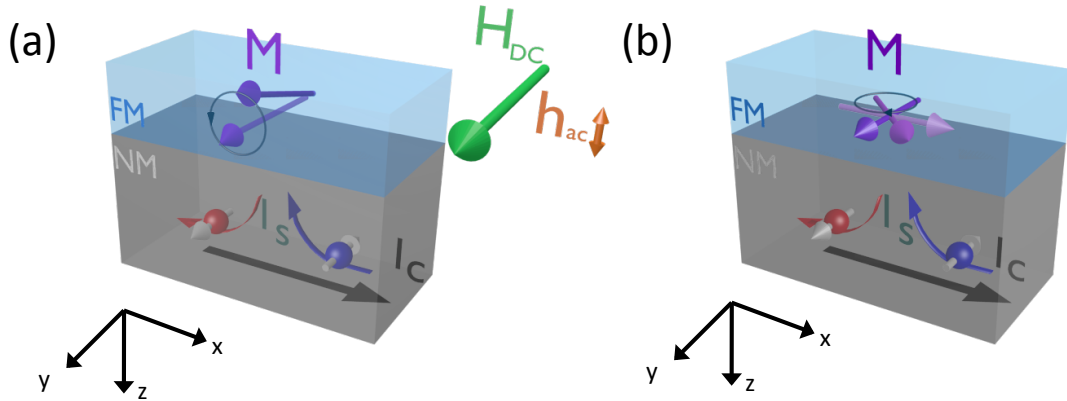


Figure 1.5: (a) Spin-pumping technique. In this case, ferromagnetic resonance induced by an *ac* field in the FM injects a *dc* spin current into the NM, which is converted into charge current due to ISHE. (b) Spin-transfer torque technique. This is the reciprocal technique, where a charge current through the NM will create a spin current due to SHE, that will induce the precession of the magnetization of the adjacent FM.

3. Electrical spin injection

Electrical spin injection was the first technique used to detect the SHE in metals [66]. In this technique, the idea is to drive a charge current through a ferromagnetic electrode, so that due to the spin polarization of the ferromagnet, a spin current (see Fig. 1.6) will be injected into the adjacent non-magnetic material, flowing in the \hat{x} direction. Depending on the spin transport properties of the non-magnetic metal, different approaches can be used to detect the ISHE. If the non-magnetic material has a relatively weak spin-orbit coupling and spin information can travel over long distances (>100 nm) then a Hall cross configuration is used (Fig. 1.6 (a)). In this case, the injected spins will have an out-of-plane polarization (\hat{z} direction) and, due to the ISHE, a charge current (flowing in the \hat{y} direction) will be detected in the Hall cross. This was successfully used to determine the SHE in aluminum [66]. Prompted by this first success, the technique was soon exploited to explore the effect on different metals. Seki *et al.* observed extremely large spin Hall angle values in gold [90], which suggests that gold could

be an excellent candidate to create a pure spin current *via* the SHE, then to transport it over a considerably long distance (~ 100 nm) and convert this spin current back to a charge current *via* ISHE. Therefore, external magnetic fields and ferromagnetic elements would be definitely avoided in this type of device. Mihajlovic *et al.* came out with the idea of an H-bar geometry, fully composed of gold [91] (Fig. 1.6 (b)). However, they could only estimate an upper bound value for the spin Hall angle, far from the giant value reported by Seki *et al.*

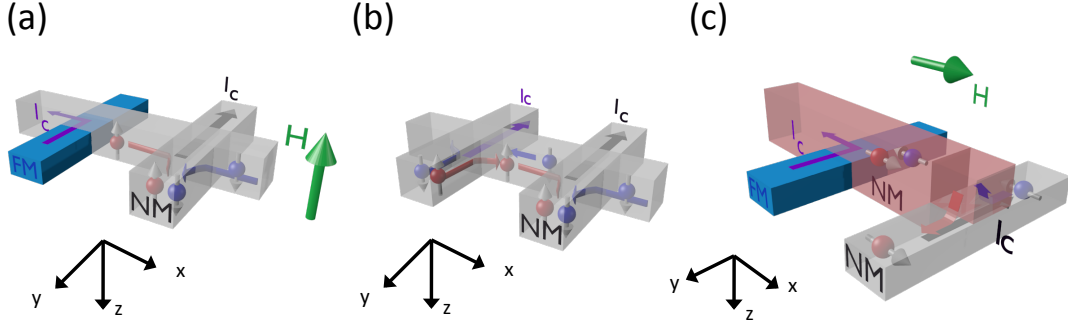


Figure 1.6: Electrical spin injection to quantify the spin Hall effect. (a) Hall-cross geometry: in this device the spin current created using a FM is injected into the metal with weak spin-orbit coupling. The generated voltage due to ISHE will be detected in the Hall bar. (b) H-bar geometry: this device does not need FM electrodes or externally applied magnetic fields. The spin current is created *via* SHE, transported and converted into a charge current due to ISHE. (c) Spin absorption geometry: three different metals are used: FM to create spin current, a NM metal to transport the spin current and the metal with strong spin-orbit coupling where the spin current will be converted into a charge current due to ISHE.

When the spin-orbit coupling of the non-magnetic material is so strong that the spin information cannot travel over long distances, a slightly different approach will be used. This alternative is to first inject a spin-polarized current with in-plane polarization (\hat{x} direction) from the ferromagnet into a metal which will carry the spin current over a long distance. This spin current will then be absorbed (in \hat{z} direction) into another metal with a strong spin-orbit coupling that will convert this spin current into charge accumulation and, therefore, a measurable voltage (in \hat{y} direction) [68] (Fig. 1.6 (c)). This is the approach that is going to be used in Chapter 5 to evaluate the SHE in different metals.

This technique requires nanometer scale devices and, therefore, the fabrication procedure is more challenging than in the spin-pumping or spin-transfer torque experiments.

4. Spin Hall magnetoresistance

The spin Hall magnetoresistance (SMR) is a recently discovered phenomena in which the SHE and its inverse act simultaneously in a non-magnetic conductor in close contact to a ferromagnetic insulator (FMI) [92]. It was observed that, depending on the magnetization of the FMI, the overall resistance of the non-magnetic material changed. The underlying physics is understood as follows: when a charge current flows through a non-magnetic metal with strong spin-orbit coupling (\hat{x} direction in Fig. 1.7), a transverse spin current will be created in the out-of-plane direction (\hat{z}) due to the SHE, with a spin polarization perpendicular to both the spin and the charge current (\hat{y} direction). In the absence of a FMI, the spin current will be reflected back at the interface, and if the non-magnetic is thin enough, due to ISHE will induce an additional charge current along the same direction as the original charge current (\hat{x} direction) (Fig. 1.7(a)).

If a FMI is placed below the NM metal, when the magnetization of the FMI is perpendicular to the spin polarization, part of the spin current will be absorbed *via* spin-transfer torque and, therefore, there will not be a reflected spin current (Fig. 1.7 (b)). This will turn out in a higher measured resistance. When the magnetization of the FMI and the spin polarization are parallel, the spin current will be reflected, inducing an additional charge current, as in the case where no FMI was placed (Fig. 1.7 (c)). This will result in a higher current, and therefore a smaller resistance will be measured. By analyzing the change in resistance, one can obtain information about the spin Hall angle of the non-magnetic material. This new magnetoresistance effect was shortly after supported by a theoretical description [93].

Despite the novelty of this technique, it has already been used in different materials with strong spin-orbit coupling such as platinum [92, 94–99], tantalum [100, 101] or palladium [102] using different FMIs as yttrium iron garnet (YIG) [92, 94, 95, 98, 100, 103] or other oxides (Fe_3O_4 [95, 96], NiFe_2O_4 [95], SrMnO_3 [104] or CoCr_2O_4 [97]). Moreover, the rich physics behind the SMR enables to study more phenomena apart from the SHE, such as the manipulation of pure spin currents [105, 106], studying the spin Seebeck effect [98, 107] or gaining more insight into the parameters that characterize the FMI/NM interface [99, 103].

Although this approach is now considered to be promising for determining many different phenomena, the origin of this effect was immersed in a big controversy at the very beginning. The disagreement raised from the possible magnetic proximity effects that the FMI could be inducing in the NM layer, in particular YIG in Pt.

Huang *et al.* [88] observed that the resistance of a Pt layer on top of YIG changed its resistance when a magnetic field was applied and they ascribed this effect to the anisotropic magnetoresistance (AMR). From the angular dependence of the AMR one expects to see a change in resistance when the relative orientation between the magnetization and the charge current direction are varied. However, from the angular dependence of the SMR (Fig. 1.7) it can be seen that the real origin for the change in resistance of the NM is the relative orientation between the magnetization of the FMI and the spin polarization \vec{s} . Therefore, their different angular dependence is a clear evidence of the different origin of both effects [108].

The main advantage of these devices is that they are usually in the micrometer scale, so even if they may need some fabrication step, the overall process is not as demanding as the one for electrical spin injection experiments. On the other hand, its main drawback is that, as it is very sensitive to the interface, a good interface quality is required to observe the effect [94, 109–112].

The SMR phenomenon was first observed in the course of this thesis. We have contributed with relevant results not discussed above that include the study of a different FMI as well as a novel functionality of SMR. All this will be analyzed in Chapter 7 of this thesis.

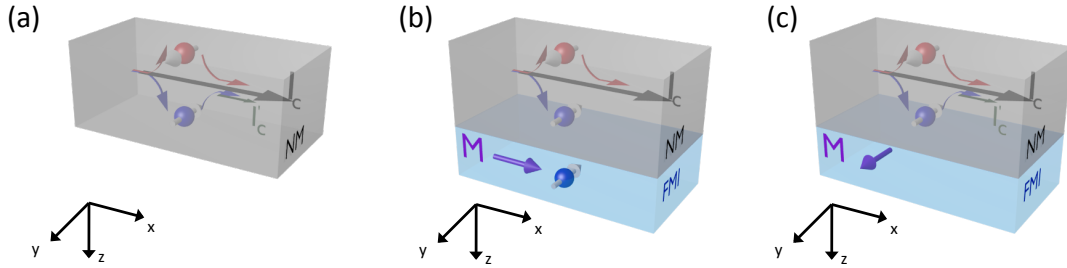


Figure 1.7: Schematic representation of the SMR. (a) A charge current \vec{J}_c is flowing in a NM layer with strong spin-orbit coupling along \hat{x} . A spin current \vec{J}_s along \hat{z} with spin polarization \vec{s} along \hat{y} is created due to SHE. In absence of an adjacent FMI layer, the spin current is reflected back at the surfaces, generating an additional charge current due to ISHE. When one of the surfaces is in contact with a FMI, the spin current will be absorbed at the NM/FMI interface if the magnetization in the FMI is perpendicular to the spin polarization of the spin current (b), or it will be reflected if the magnetization is parallel to the spin polarization (c). The difference in resistance between (b) and (c) leads to SMR.

Currently, there is a big controversy with the different spin Hall angles of metals obtained from each experimental technique (see Table 1.1). The trend is that

spin-pumping and spin-transfer torque experiments yield higher spin Hall angle values, whereas those values obtained by electrical spin injection are lower [87].

Table 1.1: Reported values of spin Hall angle for different metals and using different methods (spin-pumping = SP, spin-transfer torque = STT, spin-torque ferromagnetic resonance = ST-FMR, Hall Cross geometry = HC, Hall bar geometry = HB, spin absorption = SA and spin Hall magnetoresistance = SMR). Temperatures and resistivities are included.

Material	T(K)	$\rho(\mu\Omega \text{ cm})$	$\theta(\%)$	Method	Ref.
Pt	10	12.35	2.1 ± 0.5	SA	[76]
	293	41.32	4.0 ± 0.5	SP	[80]
	293	23.25	1.2 ± 0.2	SP	[113]
	293	25	2.7 ± 0.3	SP	[114]
	293	41.66	1.3 ± 0.2	SP	[115]
	293	98.04	2.012 ± 0.003	SP	[116]
	293	15.63	~ 8	STT	[36]
	293	20	6.8 ± 0.5	ST-FMR	[35]
	293	27.78	2.2 ± 0.4	ST-FMR	[117]
	300	32.79	11 ± 8	SMR	[95]
	293	40.82	3 ± 4	SMR	[100]
	293	83.33	~ 4	SMR	[33]
	Au	4.5	2.07	< 2.3	HB
10		4	0.21 ± 0.07	SA	[118]
293		3.97	0.35 ± 0.03	SP	[115]
293		5	0.25	SP	[114]
293		14.29	0.335 ± 0.006	SP	[116]
293		18.88	1.6 ± 0.1	SP	[116]
295		2.7	~ 11	HC	[90]
297		3.89	< 2.7	HB	[91]
Bi	3	4048	> 0.8	SA	[119]
	300	-	1.9	SP	[120]
	300	132	1.58	SP	[53]
	300	667	2	SP	[121]
Al	4.2	5.88	0.02 ± 0.01	HC	[66]
Nb	10	91	-0.87 ± 0.20	SA	[76]
Ta	10	333.3	-0.37 ± 0.11	SA	[76]
	293	187	-12 ± 4	ST-FMR	[55]
	300	185	-11 ± 1	ST-FMR	[122]
	293	1250	-2 ± 1.5	SMR	[100]
Mo	10	35.7	-0.80 ± 0.18	SA	[76]
	293	21.4	-0.05	SP	[115]
Pd	10	45.5	1.2 ± 0.4	SA	[76]
	293	25	0.64 ± 0.1	SP	[115]
	293	41.67	1.2 ± 0.2	SP	[114]
	293	27.03	0.8 ± 0.2	ST-FMR	[117]
	293	50.76	~ 1	ST-FMR	[123]
W	293	263	-33 ± 6	ST-FMR	[124]
$\text{Cu}_{88}\text{Ir}_{12}$	10	50	2.1 ± 0.6	SA	[77]
$\text{Cu}_{99.5}\text{Bi}_{0.5}$	10	11.4	-11 ± 4	SA	[78]

1.2.2 Rashba-Edelstein effect

The Rashba-Bykov effect is a momentum-dependent splitting of the spin subbands that results from the spin-orbit interaction in a two-dimensional electron gas (2DEG) where the spacial-inversion symmetry is lost in the surface (Fig. 1.8 (a)) [125,126]. Rashba semiconductor heterostructure interfaces are the perfect example of a 2DEG with lack of inversion symmetry [127]. However, there is a wider variety of systems that fulfill these conditions, such as noble metal surfaces [128], group V semimetals [129] and their alloys [130,131].

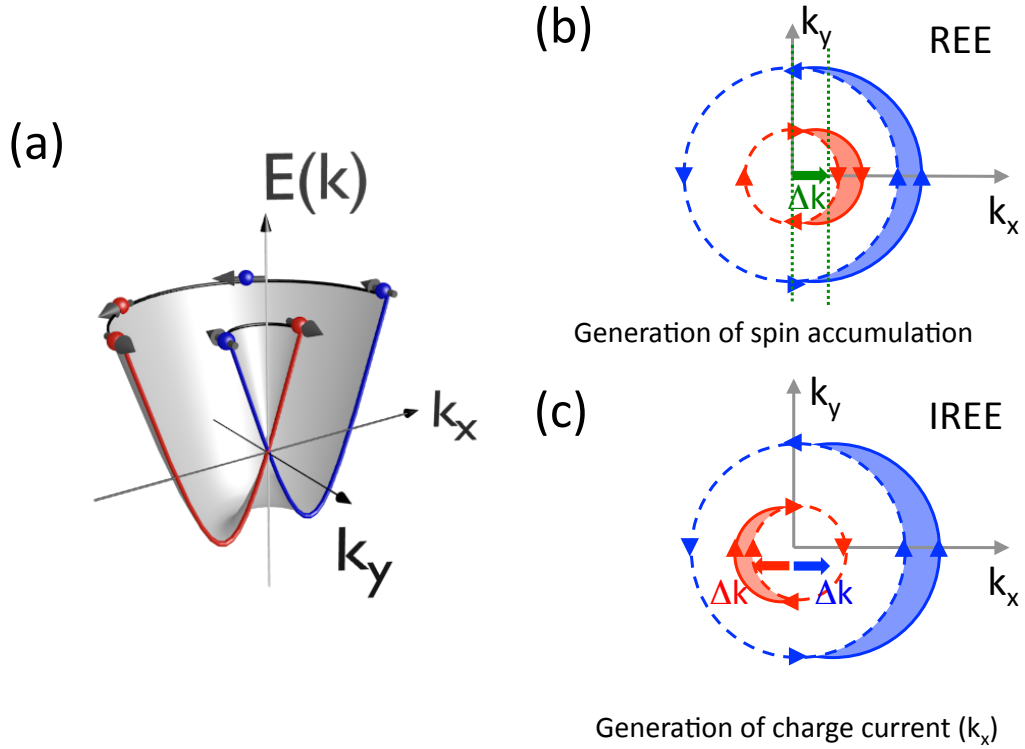


Figure 1.8: (a) Rashba effect: spin split energy dispersion curves of a 2DEG with inversion symmetry breaking. (b) Schematic representation of the Rashba-Edelstein effect where a spin accumulation (μ_s) is generated when injecting a charge current (Δk). (c) Inverse Rashba-Edelstein effect where a charge current is created (Δk) when injecting a spin current (J_s).

Let us assume that we have an electron moving with momentum \vec{k} in a 2DEG. The interaction of \vec{k} with the electron spin, \vec{s} is described by the Rashba Hamiltonian:

$$H_R = \alpha_R (\vec{s} \times \vec{k}) \cdot \hat{z}, \quad (1.13)$$

where \hat{z} is the unit vector perpendicular to the 2DEG and α_R is the Rashba coefficient, which depends on the spin-orbit coupling strength. This interaction leads to energy-momentum dispersion curves of the type shown in Fig. 1.8(a).

Edelstein was the first one to show that a charge current that feels this structural asymmetry generates a transverse spin accumulation (Fig. 1.8(b)) [132, 133]. This is known as the Rashba-Edelstein effect (REE). In a similar way, if we are able to inject spins in a 2DEG, due to the inverse Rashba-Edelstein effect (IREE), a charge accumulation will be created (Fig. 1.8(c)). This effect has been recently experimentally proven in different systems, such as silver/bismuth [52, 53] and silver/antimony [54]. In fact, the IREE can be regarded as a spin-to-charge conversion similar to the ISHE, but for the particular case where the spin-to-charge conversion is an interface driven effect. This can be a more efficient way to convert spin to charge than bulk SHE.

In Chapter 6 of this thesis, we will demonstrate and analyze the IREE in a Cu/Bi interface.

1.2.3 Spin-orbit torques

Spin-transfer torques (STTs) are being studied to control the orientation of a magnetic layer by applying a spin-polarized current instead of an external magnetic field. As seen before, STTs have been strongly studied for exciting applications such as writing in STT-MRAMs. In these devices, one of the FM layers of the MTJ is used as a spin polarizer to create a spin current that switches the magnetization of the second FM layer.

However, the great advances in the field have enabled to create spin currents without the need of a ferromagnetic polarizer by exploiting the spin-orbit coupling. This results in a great technological advantage, mainly for two reasons. First, the currents needed to exert the torque are no longer sent through the MTJ and, therefore, the possibility to break the junction disappears. Second, exploiting spin-orbit interactions results in much more efficient torques.

Different materials with strong spin-orbit coupling such as heavy metals [134] or topological insulators [135] have been used to generate spin currents by passing an in-plane charge current to switch the magnetization of an adjacent FM. Now, what comes to debate is the origin of these spin currents, which can be either coming from the

bulk SHE [55, 136] of the NM material or from the Rashba-type fields arising from the NM/FM interface [57]. Lately, it has been suggested that the spin-orbit torque may arise from different competing effects [56, 137, 138].

Despite this big controversy about its origin, what it is clear is the potential technological application that spin-orbit torques may bring for applying this physics to improve the functionality of current MRAMs.

1.3 This thesis

This work will study the spin transport and spin-to-charge current conversion properties in different metals: silver (Ag), platinum (Pt), gold (Au) and bismuth (Bi). The work will thus be divided into two main parts.

First, the spin transport properties will be studied in three metals with very different spin-orbit interactions: (i) a metal which does not have a particularly strong spin-orbit interaction but where the spin currents can diffuse over long distances, *i.e.*, Ag; (ii) a very widely studied metal which has a very strong spin-orbit coupling but where spins cannot diffuse over 10 nm, *i.e.*, Pt; and (iii) an intermediate metal, with a rather strong spin-orbit coupling and a fairly long path for spins to diffuse, *i.e.*, Au.

The second part will focus on the spin-to-charge current conversion exploiting the spin-orbit interaction of the heaviest metals: Pt, Au and Bi. We will see that, whereas the ISHE in Au and Pt is the responsible to convert spin current into charge current, the IREE is the responsible for the conversion in Bi. In each case, for ISHE and IREE, we will analyze which is the physical origin behind the effect.

The work is divided in 8 chapters.

Chapter 1 is an introduction to the topic where the main ideas and concepts that are going to be used throughout this thesis are introduced. These are lateral spin valves, the spin Hall effect, the inverse Rashba-Edelstein effect and the spin Hall magnetoresistance.

Chapter 2 introduces the theory related to the spin injection, transport and detection for the different devices that are going to be used through this thesis.

Chapter 3 describes the fabrication and characterization methods of the devices.

After some introductory remarks and experimental techniques, we will move to the discussion of the main results of this thesis.

Chapter 4 is a study of spin transport properties of Ag using lateral spin valves. In this chapter, the optimum growth conditions of Ag for transporting spin information over long distances are studied.

Chapter 5 investigates the spin transport properties of Pt and Au using a device structure which is based on a lateral spin valve, but it is slightly changed (spin absorption device). A conventional LSV would not allow to determine the spin transport properties of metals with strong spin-orbit coupling, as the spin currents in these metals do not diffuse over long distances (<100 nm). After analyzing the spin transport properties of Pt and Au, we will study the SHE in these metals using electrical spin injection. By analyzing the temperature dependence of the effect we are able to determine the different mechanisms contributing to each material.

Chapter 6 explores the newly discovered IREE in Bi. Moreover, we are able to experimentally determine the underlying physics behind this effect. This experimental proof is further evidenced by a theoretical analysis.

Chapter 7 exploits the spin Hall magnetoresistance to study the interface properties of Pt/CoFe₂O₄ bilayers and the surface magnetization of CoFe₂O₄. For this purpose, we make a systematic analysis changing Pt growth conditions and the surface orientation of CoFe₂O₄.

Chapter 8 finishes with some concluding remarks and points out future work.

References

- [1] Emerging Research Devices and Emerging Research Materials chapters of the 2013 edition of the International Roadmap for Semiconductors. <http://www.itrs.net/Links/2013ITRS/Home2013.htm>
- [2] M. N. Baibich, J. M. Broto, A. Fert, F. Nguyen Van Dau and F. Petroff, *Phys. Rev. Lett.* **61**, 2472 (1988).
- [3] G. Binasch, P. Grünberg, F. Saurenbach, and W. Zinn, *Phys. Rev. B* **39**, 4828 (1989).
- [4] S. D. Bader and S. S. P. Parkin, *Annu. Rev. Condens. Matter Phys.* **1**, 71 (2010).
- [5] J. S. Moodera, L. R. Kinder, T. M. Wong and R. Meservey, *Phys. Rev. Lett.* **74**, 3273 (1995).
- [6] T. Miyazaki and N. Tezuka, *J. Magn. Magn. Mater.* **139**, L231 (1995).
- [7] J. C. Slonczewski, *J. Magn. Magn. Mater.* **159**, L1 (1996).
- [8] L. Berger, *Phys. Rev.* **54**, 9353 (1996).
- [9] R. Sbiaa, H. Meng and N. S. Piramanayagam, *Phys. Status Solidi RRL* **5**, 413 (2011).
- [10] *Spin Current*, edited by S. Maekawa, S. O. Valenzuela, E. Saitoh and T. Kimura (Oxford University Press, Oxford, 2012).
- [11] B. Behin-Aein, D. Datta, S. Salahuddin, and S. Datta, *Nature Nanotech.* **5**, 266 (2010)
- [12] S. Datta and B. Das, *Appl. Phys. Lett.* **56**, 665 (1990).
- [13] J. M. Kikkawa and D. D. Awschalom, *Nature* **397**, 139 (1999).

- [14] R. Fiederling, M. Keim, G. Reuscher, W. Ossau, G. Schmidt, A. Waag and L. W. Molenkamp, *Nature* **402**, 787 (1999).
- [15] Y. Ohno, D. K. Young, B. Beschoten, F. Matsukura, H. Ohno and D. D. Awschalom, *Nature* **402**, 790 (1999).
- [16] M. I. Dyakonov and V. I. Perel, *Optical orientation*, edited by F. Meier and B. P. Zakharchenya (Elsevier, Amsterdam, 1984).
- [17] A. Slachter, F. L. Bakker, J. -P. Adam and B. J. van Wees, *Nature Phys.* **6**, 879 (2010).
- [18] K. Uchida, J. Xiao, H. Adachi, J. Ohe, S. Takahashi, J. Ieda, T. Ota, Y. Kajiwara, H. Umezawa, H. Kawai, G. E. W. Bauer, S. Maekawa and E. Saitoh, *Nature Mater.* **9**, 894 (2012).
- [19] A. Brataas, G. E. W. Bauer and P. J. Kelly, *Phys. Rep.* **427**, 157 (2006).
- [20] D. C. Ralph and M. D. Stiles, *J. Magn. Magn. Mater.* **320**, 1190 (2008).
- [21] M. Johnson and R. H. Silsbee, *Phys. Rev. Lett.* **55**, 1790 (1985).
- [22] F. J. Jedema, A. T. Filip and B. J. van Wees, *Nature* **410**, 345 (2001).
- [23] Y. Ji, A. Hoffmann, J. S. Jiang and S. D. Bader, *Appl. Phys. Lett.* **85**, 6218 (2004).
- [24] S. O. Valenzuela, D. J. Monsma, C. M. Marcus, V. Narayanamurti and M. Tinkham, *Phys. Rev. Lett.* **94**, 196601(2005).
- [25] S. O. Valenzuela and M. Tinkham, *Appl. Phys. Lett.* **85**, 5914 (2004).
- [26] T. Kimura, Y. Otani and J. Harmle, *Phys. Rev. B* **73**, 132405 (2006).
- [27] F. Casanova, A. Sharoni, M. Erekhinsky and I. K. Schuller, *Phys. Rev. B* **79**, 184415 (2009).
- [28] P. Laczkowski, L. Vila, V. -D. Nguyen, A. Marty, J. -P. Attané, H. Jaffrès, J. -M. George and A. Fert, *Phys. Rev. B* **85**, 220404(R) (2012).
- [29] X. Lou, C. Adelmann, S. A. Crooker, E. S. Garlid, J. Zhang, K. S. Madhukar Reddy, S. D. Flexner, C. J. Palmstrom and P. A. Crowell, *Nature Phys.* **3**, 197 (2007).

- [30] O. M. J. van t' Erve, A. T. Hanbicki, M. Holub, C. H. Li, C. Awo-Affouda, P. E. Thompson and B. T. Jonker, *Appl. Phys. Lett.* **91**, 212109 (2007).
- [31] J. Li and I. Appelbaum, *Phys. Rev. B* **84**, 165318 (2011).
- [32] L. E. Hueso, J. M. Pruneda, V. Ferrari, V. Burnell, J. P. Valdés-Herrera, B. D. Simons, P. B. Littlewood, E. Artacho, A. Fert and N. D. Mathur, *Nature* **445**, 410 (2007).
- [33] N. Tombros, C. Jozsa, M. Popinciuc, H. T. Jonkman and B. J. van Wees, *Nature* **448**, 571 (2007).
- [34] C. H. Li, G. Kioseoglou, O. M. J. van' t Erve, P. E. Thompson and B. T. Jonker, *Appl. Phys. Lett.* **95**, 172102 (2009).
- [35] L. Liu, T. Moriyama, D. C. Ralph and R. A. Buhrman, *Phys. Rev. Lett.* **106**, 036601 (2011).
- [36] K. Ando, S. Takahashi, K. Harii, K. Sasage, J. Ieda, S. Maekawa and E. Saitoh, *Phys. Rev. Lett.* **101**, 036601 (2008).
- [37] J. Flipse, F. L. Bakker, A. Slachter, F. K. Dejene, and B. J. van Wees, *Nature Nanotech.* **7**, 166 (2012).
- [38] J. Flipse, F. K. Dejene, D. Wagenaar, G. E. W. Bauer, J. Ben Youssef and B. J. van Wees, *Phys. Rev. Lett.* **113**, 027601 (2014).
- [39] F. J. Jedema, H. B. Heershe, A. T. Filip, J. J. Baselmans, and B. J. van Wees, *Nature* **416**, 713 (2002).
- [40] J. -C. Rojas Sánchez, P. Laczkowski, W. F. Savero Torres, M. Cubukcu, V. D. Nguyen, L. Notin, C. Beigné, C. Vergnaud, A. Marty, M. Jamet, L. Vila and P. Attané, *Appl. Phys. Lett.* **102**, 132408 (2013).
- [41] F. Matsukura, Y. Tokuna and H. Ohno, *Nature Nanotech.* **10**, 209 (2015).
- [42] H. C. Koo, J. H. Kwon, J. Eom, J. Chang, S. H. Han, and M. Johnson, *Science* **325**, 1515 (2009).
- [43] I. Zutic and H. Dery, *Nature Mater.* **10**, 647 (2011).
- [44] T. Kuschel and G. Reiss, *Nature Nanotech.* **10**, 22 (2015).

- [45] M. I. Dyakonov and V. I. Perel, *Phys. Lett. A* **35**, 459 (1971).
- [46] Y. A. Bychkov and E. I. Rashba, *JEOT Lett.* **39**, 78 (1984).
- [47] S. O. Valenzuela, *Int. J. Mod. Phys. B* **23**, 2413 (2009).
- [48] G. Vignale, *J. Supercond. Nov. Magn.* **23**, 3 (2010).
- [49] A. Hoffmann, *IEEE Trans. Magn.* **49**, 5172 (2013).
- [50] J. Sinova, S. O. Valenzuela, J. Wunderlich, C. H. Back and T. Jungwirth, *arXiv: 1411.3249v1* (2014).
- [51] T. Jungwirth, J. Wunderlich and K. Olejnik, *Nature Mater.*, **11**, 382 (2012).
- [52] J. C. Rojas-Sanchez, L. Vila, G. Desfonds, S. Gambarelli, J. P. Attané, J. M De Teresa, C. Magén and A. Fert, *Nature Comm.* **4**, 2944 (2013).
- [53] S. Sangiao, J. M. De Teresa, L. Morellón, I. Lucas, M. C. Martínez-Velarte and M. Viret, *Appl. Phys. Lett.* **103**, 032406 (2015).
- [54] W. Zhang, M. B. Jungfleisch, W. Jiang, J. E. Pearson and A. Hoffmann, *J. Appl. Phys.* **117**, 17C727 (2015).
- [55] L. Liu, C.-F. Pai, Y. Li, H. W. Tseng, D. C. Ralph and R. A. Buhrman, *Science* **336**, 555 (2012).
- [56] K. Garello, I. M. Miron, C. O. Avci, F. Freimuth, Y. Mokrousov, S. Blügel, S. Auffret, O. Boulle, G. Gaudin, and P. Gambardella, *Nature Nanotech.* **8**, 587 (2013).
- [57] I. M. Miron, T. Moore, H. Szabolcs, L. D. Buda-Prejbeanu, S. Auffret, B. Rodmacq, S. Pizzini, J. Vogel, J. Bonfim, A. Schuhl and G. Gaudin, *Nature* **476**, 189 (2011).
- [58] E. H. Hall, *Amer. J. Math.* **2**, 287 (1879).
- [59] E. H. Hall, *Philos. Mag.* **10**, 301 (1880); E. H. Hall, *Philos. Mag.* **12**, 157 (1881).
- [60] A. W. Smith and R. W. Sears, *Phys. Rev.* **34**, 1466 (1929).
- [61] R. Karplus and J. M. Luttinger, *Phys. Rev.* **95**, 1154 (1954).
- [62] J. Smit, *Physica* **24**, 39 (1958).
- [63] L. Berger, *Phys. Rev. B* **2**, 4559 (1970).

- [64] J. E. Hirsch, *Phys. Rev. Lett.* **83**, 9 (1999).
- [65] Y. K. Kato, R. C. Myers, A. C. Gossard and D. D. Awschalom, *Science* **306**, 1910 (2004).
- [66] S. O. Valenzuela and M. Tinkham, *Nature* **442**, 176 (2006).
- [67] E. Saitoh, M. Ueda, H. Miyajima and G. Tatara, *Appl. Phys. Lett.* **88**, 182509 (2006).
- [68] T. Kimura, Y. Otani, T. Sato, S. Takahashi and S. Maekawa, *Phys. Rev. Lett.* **98**, 156601 (2007).
- [69] Y. Tian, L. Ye and X. Jin, *Phys. Rev. Lett.* **103**, 087206 (2009).
- [70] N. Nagaosa, J. Sinova, S. Onoda, A. H. Mac Donald and N. P. Ong, *Rev. Mod. Phys.* **82**, 1539 (2010).
- [71] D. Hou, G. Su, Y. Tian, X. Jin, S. A. Yang, and Q. Niu, *Phys. Rev. Lett.* **114**, 217203 (2015).
- [72] G. Sundaram and Q. Niu, *Phys. Rev. B* **59**, 14915 (1999).
- [73] T. Tanaka, H. Kontani, M. Naito, T. Naito, D. S. Hirashima, K. Yamada, and J. Inoue, *Phys. Rev. B* **77**, 165117 (2008).
- [74] G. Y. Guo, *J. Appl. Phys.* **105**, 07C701 (2009).
- [75] M. Gradhand, D. V. Fedorov, P. Zahn, and I. Mertig, *Phys. Rev. Lett.* **104**, 186403 (2010).
- [76] M. Morota, Y. Niimi, K. Ohnishi, D. H. Wei, T. Tanaka, H. Kontani, T. Kimura, and Y. Otani, *Phys. Rev. B* **83**, 174405 (2011).
- [77] Y. Niimi, M. Morota, D. H. Wei, C. Deranlot, M. Basletic, A. Hamzic, A. Fert and Y. Otani, *Phys. Rev. Lett.* **106**, 126601 (2011).
- [78] Y. Niimi, Y. Kawanishi, D. H. Wei, C. Deranlot, H. X. Yang, M. Chshiev, T. Valet, A. Fert and Y. Otani, *Phys. Rev. Lett.* **109**, 156602 (2012).
- [79] L. Onsager, *Phys. Rev.* **37**, 405 (1931).
- [80] A. Azevedo, L. H. Vilela-Leao, R. L. Rodriguez-Suarez, A. F. L. Santos and S. M. Rezende, *Phys. Rev. B* **83**, 144402 (2011).

- [81] O. Mosendz, J. E. Pearson, F. Y. Fradin, G. E. W. Bauer, S. D. Bader and A. Hoffmann, *Phys. Rev. Lett.* **104**, 046601 (2010).
- [82] K. Ando, S. Takahashi, J. Ieda, H. Kurebayashi, T. Trypiniotis, C. H. W. Barnes, S. Maekawa and E. Saitoh, *Nature Mater.* **10**, 655 (2011).
- [83] Y. Kajiwara, K. Harii, S. Takahashi, J. Ohe, K. Uchida, M. Mizuguchi, H. Umezawa, H. kawai, K. Ando, K. Tajanashi, S. Maekawa and E. Saitoh, *Nature* **464**, 262 (2010).
- [84] L. H. Vilela-Leao, C. Salvador, A. Azevedo and S. M. Rezende, *Appl. Phys. Lett.* **99**, 102505 (2011).
- [85] B. Heinrich, C. Burrowes, E. Montoya, B. Kardasz, E. Girt, Y.-Y. Song, Y. Sun and M. Wu, *Phys. Rev. Lett.* **107**, 066604 (2011).
- [86] V. Castel, N. Vlietstra, J. Ben Youssef and B. J. van Wees, *Appl. Phys. Lett.* **101**, 132414 (2012).
- [87] L. Liu, A. Buhrman and D. C. Ralph, *arXiv*: 1111.3702v3 (2012).
- [88] S. Y. Huang, X. Fan, D. Qu, Y. P. Chen, W. G. Wang, J. Wu, T. Y. Chen, J. Q. Xiao and C. L. Chien, *Phys. Rev. Lett.* **109**, 107204 (2012).
- [89] Y. Sun, H. Chang, M. Kabatek, Y.-Y. Song, Z. Wang, M. Jantz, W. Schneider, M. Wu, E. Montoya, B. Kardasz, B. Heinrich, S. G. E. te Velthuis, H. Schultheiss and A. Hoffmann, *Phys. Rev. Lett.* **111**, 106601 (2013).
- [90] T. Seki, Y. Hasegawa, S. Mitani, S. Takahashi, H. Imamura, S. Maekawa, J. Nitta and K. Takanashi, *Nature Mater.* **7**, 125 (2008).
- [91] G. Mihajlovic, J. E. Pearson, M. A. Garcia, S. D. Bader and A. Hoffmann, *Phys. Rev. Lett.* **103**, 166601 (2009).
- [92] H. Nakayama, M. Althammer, Y.-T. Chen, K. Uchida, Y. Kajiwara, D. Kikuchi, T. Ohtani, S. Geprägs, M. Opel, S. Takahashi, R. Gross, G. E. W. Bauer, S. T. B. Goennenwein and E. Saitoh, *Phys. Rev. Lett.* **110**, 206601 (2013).
- [93] Y. -T. Chen, S. Takahashi, H. Nakayama, M. Althammer, S. T. B. Goennenwein, E. Saitoh and G. Bauer, *Phys. Rev. B* **87**, 144411 (2013).
- [94] N. Vlietstra, J. Shan, V. Castel, B. J. van Wees, and J. Ben Youssef, *Phys. Rev. B* **87**, 184421 (2013).

- [95] M. Althammer, S. Meyer, H. Nakayama, M. Schreier, S. Altmannshofer, M. Weiler, H. Huebl, S. Geprägs, M. Opel, R. Gross, D. Meier, C. Klewe, T. Kuschel, J.-M. Schmalhorst, G. Reiss, L. Shen, A. Gupta, Y.-T. Chen, G. E. W. Bauer, E. Saitoh, and S. T. B. Goennenwein, *Phys. Rev. B* **87**, 224401 (2013).
- [96] Z. Ding, B. L. Chen, J. H. Liang, J. Zhu, J. X. Li, and Y. Z. Wu, *Phys. Rev. B* **90**, 134424 (2014).
- [97] A. Aqueel, N. Vlietstra, J. A. Heuver, G. E. W. Bauer, B. Noheda, B. J. van Wees, and T. M. Plastra, *arXiv*: 1507.01352.
- [98] N. Vlietstra, J. Shan, B. J. van Wees, M. Isasa, F. Casanova, J. Ben Youssef, *Phys. Rev. B* **90**, 174436 (2014).
- [99] M. Weiler, M. Althammer, M. Schreier, J. Lotze, M. Perpeintner, S. Meyer, H. Huebl, R. Gross, A. Kamra, J. Xiao, Y. T. Chen, H. J. Jiao, G. E. W. Bauer, S. T. B. Goennenwein, *Phys. Rev. Lett.* **111**, 176601 (2013).
- [100] C. Hahn, G. de Loubens, O. Klein, M. Viret, V. V. Naletov, and J. Ben Youssef, *Phys. Rev. B* **87**, 174417 (2013).
- [101] Y. Yang, B. Wu, K. Yao, S. Shannigrahi, B. Zong, and Y. Wu, *J. Appl. Phys.* **115**, 17C509 (2014).
- [102] T. Lin, C. Tang, H. M. Alyahyaei, and J. Shi, *Phys. Rev. Lett.* **113**, 037203 (2014).
- [103] N. Vlietstra, J. Shan, V. Castel, J. Ben Youssef, G. E. W. Bauer and B. J. van Wees, *Appl. Phys. Lett.* **103**, 032401 (2013).
- [104] J. H. Han, C. Song, F. Li, Y. Y. Wang, G. Y. Wang, Q. H. Yang, and F. Pan, *Phys. Rev. B* **90**, 144431 (2014).
- [105] E. Villamor, M. Isasa, S. Velez, A. Bedoya-Pinto, P. Vavassori, L. E. Hueso, F. S. Bergeret and F. Casanova, *Phys. Rev. B* **91**, 020403(R) (2015).
- [106] F. K. Dejene, N. Vlietstra, D. Luc, X. Waintal, J. Ben Youssef and B. J. van Wees, *Phys. Rev. B* **91**, 100404(R) (2015).
- [107] M. Schreier, N. Roschewsky, E. Dobler, S. Meyer, H. Huebl, R. Gross and S. T. B. Goennenwein, *Appl. Phys. Lett.* **103**, 242404 (2013).

- [108] B. F. Miao, S. Y. Huang, D. Qu, and C. L. Chien, *Phys. Rev. Lett.* **112**, 236601 (2014).
- [109] C. Burrowes, B. Heinrich, B. Kardasz, E. A. Montoya, E. Girt, Y. Sun, Y. -Y. Song and M. Wu, *Appl. Phys. Lett.* **100**, 092403 (2012).
- [110] L. Qiu, K. Ando, K. Uchida, Y. Kajiwara, R. Takahashi, H. Nakayama, T. An, Y. Fujikawa and E. Saitoh, *Appl. Phys. Lett.* **103**, 092404 (2013).
- [111] Y. Ando, K. Ichiba, S. Yamada, E. Shikoh, T. Shinjo, K. Hamaya and M. Shiraishi, *Phys. Rev. B* **88**, 140406(R) (2013).
- [112] M. B. Jungfleisch, V. Lauer, R. Neb, A. V. Chmak and B. Hillebrands, *Appl. Phys. Lett.* **103**, 022411 (2013).
- [113] Z. Feng, J. Hu, L. Sun, B. You, D. Wu, J. Du, W. Zhang, A. Hu, Y. Yang, D. M. Tang, B. S. Zhang, and H. F. Ding, *Phys. Rev. B* **85**, 214423 (2012).
- [114] V. Vlaminck, J. E. Pearson, S. D. Bader and A. Hoffmann, *Phys. Rev. B* **88**, 064414 (2013).
- [115] O. Mosendz, V. Vlaminck, J. E. Pearson, F. Y. Fradin, G. E. W. Bauer, S. D. Bader and A. Hoffmann, *Phys. Rev. B* **82**, 214403 (2010).
- [116] H. Y. Hung, G. Y. Luo, Y. C. Chiu, P. Chang, W. C. Lee, J. G. Lin, S. F. Lee, M. Hong and J. Kwo, *J. Appl. Phys.* **113**, 17C507 (2013).
- [117] K. Kondou, H. Sukegawa, S. Mitani, K. Tsukagoshi, and S. Kasai, *Appl. Phys. Express* **5**, 073002 (2012).
- [118] Y. Niimi, H. Suzuki, Y. Kawanishi, Y. Omori, T. Valet, A. Fert and Y. Otani, *Phys. Rev. B* **89**, 054401 (2014).
- [119] J. Fan and J. Eom, *Appl. Phys. Lett.* **92**, 142101 (2008).
- [120] D. Hou, Z. Qiu, K. Harii, Y. Kajiwara, K. Uchida, Y. Fujikawa, H. Nakayama, T. Yoshino, T. An, K. Ando, X. Jin, and E. Saitoh, *Appl. Phys. Lett.* **101**, 042403 (2012).
- [121] H. Emoto, Y. Ando, E. Shikoh, Y. Fuseya, T. Shinjo, and M. Shiraishi, *J. Appl. Phys.* **115**, 17C507 (2014).

- [122] G. Allen, S. Manipatruni, D. E. Nikonov, M. Doczy and I. A. Young, *Phys. Rev. B* **91**, 144412 (2015).
- [123] K. Ando and E. Saitoh, *J. Appl. Phys.* **108**, 113925 (2010).
- [124] C. F. Pai, L. Liu, H. W. Tseng, D. C. Ralph and R. A. Buhrman, *Appl. Phys. Lett.* **101**, 122404 (2012).
- [125] Y. A. Bychkov and E. I. Rashba, *J. Phys. C: Solid State Phys.* **17**, 6039 (1984).
- [126] Y. A. Bychkov and E. I. Rashba, *JEPT Lett.* **39**, 78 (1984).
- [127] J. Nitta, T. Akazaki, H. Takayangi and T. Enoki, *Phys. Rev. Lett.* **78**, 1335 (1997).
- [128] S. LaShell, B. A. McDouglas, E. Jensen, *Phys. Rev. Lett.* **77**, 3419 (1996).
- [129] K. Sugawara, T. Sato, S. Souma, T. Takahashi, M. Arai and T. Sasaki, *Phys. Rev. Lett.* **96**, 046411 (2006).
- [130] C. R. Ast and H. Höchst, *Phys. Rev. Lett.* **87**, 177602 (2001).
- [131] Y. M. Koroteev, G. Bihlmayer, J. E. Gayone, E. V. Chulkov, S. Blügel, P. M. Echenique, Ph. Hofmann, *Phys. Rev. Lett.* **93**, 046403 (2004).
- [132] V. M. Edelstein, *Solid State Commun.* **73**, 233 (1990).
- [133] K. Shen, G. Vignale, and R. Raimondi, *Phys. Rev. Lett.* **112**, 096601 (2014).
- [134] A. R. Mellnik, J. S. Lee, A. Richardella, J. L. Grab, P. J. Mintum, M. H. Fischer, A. Vaezi, A. Manchon, E.-A. Kim, N. Samarth and D. C. Ralph, *Nature* **511**, 449 (2014).
- [135] Y. Fan, P. Upadhyaya, X. Kou, M. Lang, S. Takei, Z. Wang, J. Tang, L. He, L. Chang, M. Montazeri, G. Yu, W. Jiang, T. Nie, R. N. Schwartz, Y. Tserkovnyak and K. L. Wang, *Nature Mater.* **13**, 699 (2014).
- [136] L. Liu, O. J. Lee, T. J. Gudmundsen, D. C. Ralph and R. A. Buhrman, *Phys. Rev. Lett.* **109**, 096602 (2012).
- [137] C. O. Avci, K. Garello, C. Nistor, S. Godey, B. Ballesteros, A. Mugarza, A. Barla, M. Valvidares, E. Pellegrin, A. Ghosh, I. M. Miron, O. Boulle, S. Auffret, G. Gaudin, and P. Gambardella, *Phys. Rev. B* **89**, 214419 (2014).

- [138] J. Kim, J. Shina, M. Hayashi, M. Yamanouchi, S. Fukami, T. Suzuki, S. Mitani and H. Ohno, *Nature Mater.* **12**, 240 (2013).

Chapter 2

Multiterminal non-magnetic/ ferromagnetic structures

In this chapter, we discuss the basic physical concepts that are needed to understand the work on spin-dependent transport of the upcoming chapters. First, we will describe the theory for spin injection, transport and detection in a lateral spin valve and its extension for spin absorption devices. Afterwards, we will discuss how to characterize each type of device to obtain their particular parameters: spin transport and injection properties in a lateral spin valve and spin transport and spin-to-charge conversion efficiency in a spin absorption device. Finally, we will move to a completely different type of device: hybrid non-magnetic metal/ferromagnetic insulator bilayers. Here, we will explain how to characterize the spin Hall magnetoresistance and the different parameters that one can obtain from this effect.

2.1 Non-local-based devices

2.1.1 Lateral spin valves

Lateral spin valves (LSVs) are spintronic devices consisting of two ferromagnetic (FM) electrodes bridged by a non-magnetic (NM) channel (Figs. 2.2(a) and 2.3(a)). Their non-local geometry, in which the current excitation and voltage measurement paths are spatially separated, enables the creation of pure spin currents. Therefore, spurious effects coming from the charge, such as anisotropic magnetoresistance or anomalous Hall

effect, can be ruled out. In the following, the theory behind the spin current injection, transport and detection will be described in detail.

Electrical spin injection and spin accumulation

Electron transport in a diffusive channel is a result of a gradient in the electrochemical potential, μ , which includes the kinetic and the potential energy of a particle. The kinetic energy is the chemical potential (μ_{ch}) which is, by definition, the necessary energy to add one particle to the system. For simplicity, the chemical potential of a particle at the Fermi level is set to zero. For small variations from the equilibrium, the chemical potential is the density of the excess electrons, n , divided by the density of states (DOS) at the Fermi level, $N(E_F)$, $\mu_{ch} = n/N(E_F)$. Moreover, the potential energy is the result of putting the electrons to an external electric field, \vec{E} . Hence, $\mu = \mu_{ch} - eV$, where e is the electron charge and V is the electric potential. As μ is the quantity that describes the thermodynamic equilibrium, a gradient in μ is the driving force for electron transport, which leads to a current density:

$$\vec{j}_c = \frac{\sigma}{e} \vec{\nabla} \mu, \quad (2.1)$$

where σ is the electrical conductivity. The electron transport can result from both a spatial variation in the electronic density ($\vec{\nabla} \mu_{ch} \propto \vec{\nabla} n$) or due to an electric field ($\vec{E} = -\vec{\nabla} V$)

Let us assume that we have a charge current flowing through a FM metal. FM materials, unlike NM materials, have different density of states for the spin-up and spin-down electrons at the Fermi level created by the band shifting due to exchange interaction (Fig. 2.1 (a)). If we consider that the mean free path of the electrons is much shorter than the length over which the spin information is preserved, the conduction through a FM can be described in terms of a two-channel model. This model was introduced by Mott [1,2] and can be visualized as spin-up electrons traveling through a channel with conductivity σ_{\uparrow} , whereas the spin-down electrons travel through a parallel channel with conductivity σ_{\downarrow} . Therefore, the conductivities for spin-up and spin-down electrons are different:

$$\sigma_{\uparrow,\downarrow} = \frac{1}{3} N_{\uparrow,\downarrow}(E_F) e^2 v_{F\uparrow,\downarrow} l_{e\uparrow,\downarrow}, \quad (2.2)$$

where $N_{\uparrow,\downarrow}(E_F)$ are the spin-dependent DOS at the Fermi level, $v_{F\uparrow,\downarrow}$ are the spin-dependent Fermi velocities and $l_{e\uparrow,\downarrow}$ are the spin-dependent electron mean free paths.

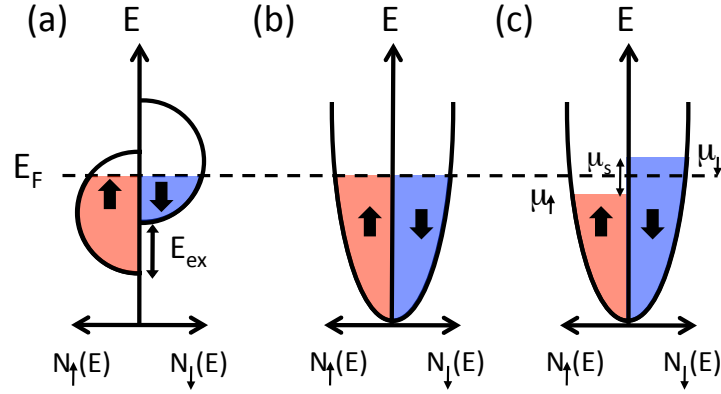


Figure 2.1: (a) Schematic representation of the DOS of 3d spin sub-bands in a FM metal. The bands are shifted with respect to each other due to exchange interaction (E_{ex}). (b) Schematic representation of the s spin sub-bands in a NM metal without spin accumulation. (c) Schematic representation of the s spin sub-bands in a NM metal near the interface with spin accumulation.

Given the different conductivities for the spin-up and -down electrons, the current density in the FM will be distributed over two channels:

$$\vec{j}_{\uparrow,\downarrow} = \frac{\sigma_{\uparrow,\downarrow}}{e} \vec{\nabla} \mu_{\uparrow,\downarrow}, \quad (2.3)$$

where \vec{j}_{\uparrow} are the spin-up and \vec{j}_{\downarrow} spin-down current densities, respectively and $\mu_{\uparrow,\downarrow}$ is the electrochemical potential for spin-up and spin-down electrons. The sum of both results in the total charge current density:

$$\vec{j}_c = \vec{j}_{\uparrow} + \vec{j}_{\downarrow}, \quad (2.4)$$

whereas the spin current density is defined as

$$\vec{j}_s = \vec{j}_\uparrow - \vec{j}_\downarrow. \quad (2.5)$$

The spin current can thus be visualized as a sum of two charge currents with opposite spins flowing in the opposite direction. From Eq. 2.5, it can be deduced that the current in a FM is spin polarized, with a spin polarization given by

$$\alpha_{FM} = \frac{\sigma_\uparrow - \sigma_\downarrow}{\sigma_\uparrow + \sigma_\downarrow}. \quad (2.6)$$

In a LSV, when a charge current is applied between the first FM electrode and one end of the NM channel (Fig. 2.2(a)), a spin-polarized current will be injected into the NM. Since the conductivities for spin-up and spin-down electrons in a NM metal are the same (Fig. 2.1(b)), a spin imbalance will be created at the NM close to the FM/NM interface. This non-equilibrium spin population at the interface is known as spin accumulation, μ_s , and it is defined as the difference in electrochemical potential for spin-up and spin-down electrons, $\mu_s = \mu_\uparrow - \mu_\downarrow$ (Fig. 2.1(c)). This can also be seen in the left side of Fig. 2.2(b). The continuity of μ_\uparrow and μ_\downarrow at the FM/NM interface is shown to be the responsible for the spin accumulation.

Spin transport

The spin accumulation at the NM channel will decay away from the interface via spin-flip scattering events with the environment to restore the equilibrium conditions. This is known as the spin relaxation process. For the particular case of metals, in absence of magnetic impurities, Elliott and Yafet stated that this spin-flip event occurred due to the spin-orbit interactions [3,4]. If we consider the local atomic electric field induced by the lattice ions, the Bloch states become linear combination of spin-up and spin-down states, mixing the majority spin states into the minority states and vice versa. Elliott showed that the spin-relaxation time, the time between spin-flip scattering events τ_{sf} , is proportional to the momentum-relaxation time, τ_e :

$$1/\tau_{sf} = a/\tau_e, \quad (2.7)$$

being a the spin-flip probability. τ_e can be calculated using $\tau_e = 3/\rho_N N(E_F) e^2 v_F^2$, where ρ_N is the resistivity of the NM.

The decay of the spin accumulation can be described by the one-dimensional spin-dependent diffusion equation developed by Valet and Fert [5]:

$$D \frac{\partial^2 \mu_s}{\partial^2 x} = \frac{\mu_s}{\tau_{sf}}, \quad (2.8)$$

where $D = 1/\rho_N N(E_F) e^2$ is the diffusion coefficient. The solution to Eq. 2.8 in the NM channel, where this spin accumulation diffuses, is given by:

$$\mu_s = \mu_+ e^{-x/\lambda_N} + \mu_- e^{x/\lambda_N}, \quad (2.9)$$

where μ_+ and μ_- are constants to be determined with spin and charge current continuity conditions at both FM/NM interfaces and $\lambda_N = \sqrt{D\tau_{sf}}$ is the spin-diffusion length of the NM channel. This parameter quantifies the distance over which a spin current can propagate without losing its spin polarization. From Eq. 2.7 and the definitions of D and τ_e , the spin diffusion length dependence on the resistivity of the NM channel is expected to be $\lambda_N \propto 1/\rho_N$.

The exponential decay expected from Eq. 2.9 is reflected in Fig. 2.2(b) (middle part). Note that μ is discontinuous at the first FM/NM interface and zero throughout the middle part of the NM channel, since due to the non-local configuration there is no electric current flowing through there, but just a pure spin current.

Electrical spin detection

If a second FM electrode is placed before the equilibrium condition is fully restored, in a similar way to the injection process, the continuity in μ_\uparrow and μ_\downarrow in the second NM/FM interface leads to the discontinuity in μ ($\Delta\mu$ in the right side of Fig. 2.2(b)). This will generate a measurable voltage ($V_s = \Delta\mu/e$), which is proportional to the spin accumulation at the interface between the second FM and the NM channel.

An expression for the detected voltage, V_s , can be derived solving Eq. 2.8 with

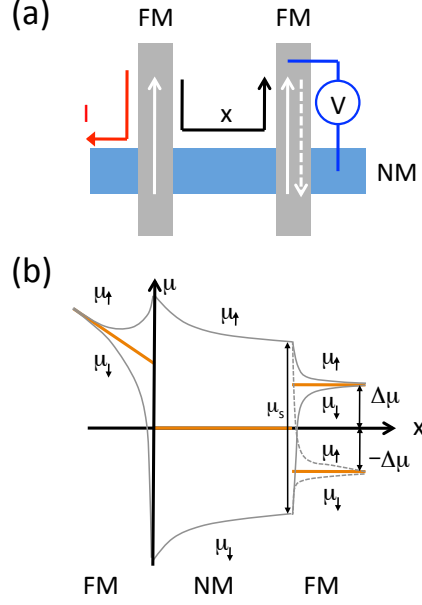


Figure 2.2: (a) Schematic representation of a LSV, where the FM injector, NM channel and the FM detector are shown, together with the non-local measurement scheme. (b) Evolution of the electrochemical potential (orange line) along \hat{x} direction. Electrochemical potential of spin-up and spin-down electrons (grey line). The solid (dashed) line represents the electrochemical potential when both FM have a parallel (antiparallel) magnetization. Figure adapted from Ref. [6].

the following boundary conditions: i) continuity of μ_{\uparrow} and μ_{\downarrow} at the interface and ii) conservation of spin-up and spin-down currents (j_{\uparrow} , j_{\downarrow}) across the interface. Applying these continuity conditions, in its most general form, the measured voltage at the second FM/NM interface is given by [7]:

$$V_s = I \frac{2R_N \left[\frac{P_{I1}}{1-P_{I1}^2} \frac{R_{I1}}{R_N} + \frac{\alpha_{F1}}{1-\alpha_{F1}^2} \frac{R_{F1}}{R_N} \right] \left[\frac{P_{I2}}{1-P_{I2}^2} \frac{R_{I2}}{R_N} + \frac{\alpha_{F2}}{1-\alpha_{F2}^2} \frac{R_{F2}}{R_N} \right] e^{-L/\lambda_N}}{\left[1 + \frac{1}{1-P_{I1}^2} \frac{R_{I1}}{R_N} + \frac{1}{1-\alpha_{F1}^2} \frac{R_{F1}}{R_N} \right] \left[1 + \frac{1}{1-P_{I2}^2} \frac{R_{I2}}{R_N} + \frac{1}{1-\alpha_{F2}^2} \frac{R_{F2}}{R_N} \right] - e^{-2L/\lambda_N}}, \quad (2.10)$$

where α_{Fi} and λ_N are the previously defined spin polarization at the injector ($i=1$) or at the detector ($i=2$) and the spin diffusion length of the non magnetic channel. P_{Ii} is the spin polarization at the i interface, R_{Ii} is the resistance of the i interface, L is the edge-to-edge distance in between both ferromagnets and $R_{N,Fi}$ are the spin resistances for the NM channel and the FM electrodes, respectively. P_{Ii} is a phenomenological description that accounts for the spin injection efficiency of the interface and it can be

defined as [7–9]:

$$P_{Ii} = \frac{R_{Ii}^{\downarrow} - R_{Ii}^{\uparrow}}{R_{Ii}^{\downarrow} + R_{Ii}^{\uparrow}}, \quad (2.11)$$

where $R_{Ii}^{\downarrow, \uparrow}$ are the spin-dependent interface resistances at i . An important parameter that appears in Eq. 2.10 is the spin resistance. This is related to the opposition of the material to let the spin current flow. Therefore, spin currents will not tend to go through materials with high spin resistances. The most general definition of the spin resistance, regardless of the material being a FM or a NM, is $R_S = \frac{\rho \lambda^2}{V}$ where ρ is the electrical resistivity of the material, λ is the spin diffusion length and V is the volume of the material where the spin current diffuses [10, 11]. For the case of a FM, as they usually have very short spin diffusion length, the spin current decays very close to the FM/NM interface, so $V = w_F w_N \lambda_F$, where w_F and w_N are the width of the FM and the NM metal, respectively. Therefore, the spin resistance in the FM is defined as:

$$R_F = \frac{\rho_F \lambda_F}{w_F w_N}. \quad (2.12)$$

For the case of NM metals used in lateral spin valves, the spin diffusion length is much larger than the channel dimensions ($\lambda_N > w_N, t_N$). The spin current will thus diffuse over a distance λ_N to both sides of the FM/NM interface, so that V is defined as $V = w_N t_N 2\lambda_F$, where t_N is the thickness of the NM metal. The spin resistance is defined as:

$$R_N = \frac{\rho_N \lambda_N}{2w_N t_N}. \quad (2.13)$$

Usually, the detected voltage is normalized by the injected current, which results in a magnitude called non-local resistance, $R_{NL} = \frac{V_s}{I}$. Strictly speaking, this is not a real resistance, since the charge current injection path is spatially separated from the voltage detection. The value of this resistance can be positive or negative depending on the relative magnetization of the injector and the detector. When both electrodes are in a parallel configuration (P), the FM detector will be sensitive to the injected excess

spin population, and the measured voltage will be positive. If they are in an antiparallel (AP) configuration, the detector will be sensitive to the opposite spin orientation of the injected ones, and therefore a negative voltage of the same magnitude will be detected (see right side of Fig. 2.2(b)). The relative magnetization between the injector and the detector can be controlled by sweeping an external magnetic field in the direction of the easy axis of the electrodes. Figure 2.3(b) shows the characteristic shape of a non-local spin valve measurement. The fact that we can detect a contrast between P and AP in the measured voltage ensures that what we are sensitive to the spin accumulation. Therefore, possible artifacts coming from charge or other effects can be ruled out. The change from a positive to a negative R_{NL} is defined as the spin signal, $\Delta R_{NL} = \frac{V_s(P) - V_s(AP)}{I}$, and it is tagged in Fig. 2.3(b). The spin signal, in the most general case, can be written as:

$$\Delta R_{NL} = \frac{4R_N \left[\frac{P_{I1}}{1-P_{I1}^2} \frac{R_{I1}}{R_N} + \frac{\alpha_{F1}}{1-\alpha_{F1}^2} \frac{R_{F1}}{R_N} \right] \left[\frac{P_{I2}}{1-P_{I2}^2} \frac{R_{I2}}{R_N} + \frac{\alpha_{F2}}{1-\alpha_{F2}^2} \frac{R_{F2}}{R_N} \right] e^{-L/\lambda_N}}{\left[1 + \frac{1}{1-P_{I1}^2} \frac{R_{I1}}{R_N} + \frac{1}{1-\alpha_{F1}^2} \frac{R_{F1}}{R_N} \right] \left[1 + \frac{1}{1-P_{I2}^2} \frac{R_{I2}}{R_N} + \frac{1}{1-\alpha_{F2}^2} \frac{R_{F2}}{R_N} \right] - e^{-2L/\lambda_N}}. \quad (2.14)$$

Equation 2.14 is valid for any kind of FM/NM interface. However, we are going to simplify the equation to two limiting cases: (i) transparent FM/NM interface and (ii) tunneling FM/NM interface.

- Transparent FM/ NM interface

In this kind of interface, there is a negligible interface resistance as there is an ohmic contact in between the FM and the NM metal and, therefore, $R_I \ll R_F, R_N$. Moreover, the spin resistance of the FM is usually smaller than the spin resistance of the NM, so that we can write $R_I \ll R_F \ll R_N$. Taking these two conditions into account and assuming that the FM injector and detector are made of the same material, so that $\alpha_{F1} = \alpha_{F2} = \alpha_F$ and $R_{F1} = R_{F2} = R_F$, Eq. 2.14 can be simplified in the following way:

$$\Delta R_{NL} = \frac{2R_N \alpha_F^2}{\left[\frac{(1-\alpha_F^2)R_N}{R_F} + 1 \right]^2 e^{L/\lambda_N} - \left[\frac{(1-\alpha_F^2)R_N}{R_F} \right]^2 e^{-L/\lambda_N}}. \quad (2.15)$$

From the previous equations it can be seen that the magnitude of the spin signal,

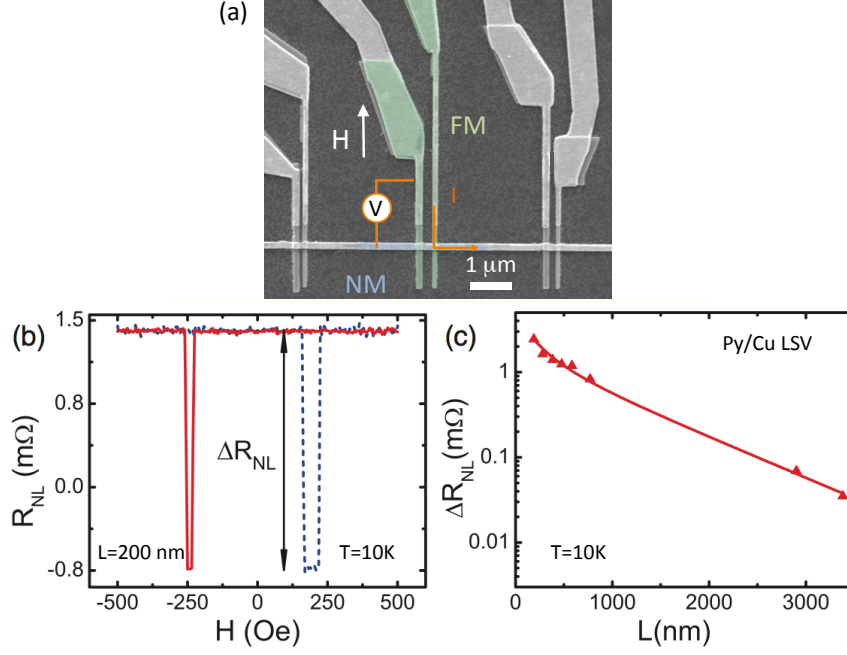


Figure 2.3: (a) Scanning electron microscope (SEM) image of various LSVs with different inter electrode distances, L . (b) Non-local resistance measured as a function of the applied magnetic field in a Py/Cu LSV with transparent interfaces at 10 K for $L=200\text{ nm}$. The red solid (blue dashed) line represent the decreasing (increasing) field from positive (negative) field values towards negative (positive) values. The spin signal, ΔR_{NL} , is represented in the figure as the change from positive to negative resistance values. (c) ΔR_{NL} as a function of L for Py/Cu LSVs with transparent interfaces at 10 K. Solid line is a fit of the data to Eq. 2.15. Figure adapted from Ref. [21].

i.e., the spin injection efficiency, is basically controlled by the R_N/R_F ratio. If the spin resistance of the NM channel is much higher than the spin resistance of the FM, there will be an amount of spins that will flow back to the FM and, therefore, a smaller spin signal will be detected in the second FM. This lack of efficiency injecting the spins is known as the *conductivity mismatch* [12]. This occurs in most systems, because FM metals have lower spin resistance than NM materials but it is specially critical in the case of semiconductors, which have even higher resistivities than NM metals.

- Tunneling FM/ NM interface

The conductivity mismatch problem can be solved if the interface resistance between FM/NM verifies $R_I \gg R_N \gg R_F$, for example using a tunnel barrier [13]. Taking these conditions into consideration and assuming $P_{I1} = P_{I2} = P_I$, Eq. 2.14 can be simplified as:

$$\Delta R_{NL} = 2P_I^2 R_N e^{-L/\lambda_N}. \quad (2.16)$$

As can be seen, the spin signal will now depend on R_N , but no longer on the R_N/R_F ratio.

The drawback of using tunnel barriers is that the spin current that can be injected is limited, as too high current densities may break the tunnel barrier. Additionally, it is known that the spin polarization (P_I) of a tunnel barrier decreases with increasing the applied bias [14]. This occurs because P_I in a tunnel barrier is proportional to the difference between spin-up and spin-down DOS at the FM metal, which is smaller above the Fermi level. On the contrary, α_F is constant for the case of a transparent interface as the DOS above the Fermi level are not accessible [6].

An alternative way to overcome the conductivity mismatch problem is by using FM materials with high spin polarization (α_F) or high resistivity (ρ_F). As can be seen in Eq. 2.15, enhancing these parameters will bring a considerable increase of the detected spin signal. This can be achieved using Heusler alloys, as shown by different groups [15–17].

There are two main properties that one can quantify from a LSV: (i) the spin transport of the NM channel, which is given by the spin diffusion length, λ_N ; and (ii) the spin injection efficiency, characterized by the spin polarization at the interface, P_I , if we have a tunnel barrier or by the spin polarization of the FM, α_F , if we have a transparent contact. These two parameters are obtained by fitting the spin signal, ΔR_{NL} , as a function of L to Eq. 2.16 or 2.15, respectively (see, for instance, Fig. 2.3(c)). Therefore, a very important requirement to detect a spin signal in a LSV is that the FM injector and detector should be separated by a distance of the order of the spin diffusion length of the channel ($L \sim \lambda_N$). This is not a problem for metals with long spin diffusion length such as copper [6, 18–22], aluminum [6, 8, 14, 23, 24] or silver [25–27], where successful studies have been carried out.

2.1.2 Spin absorption devices

In metals with strong spin-orbit coupling (SOC), the spin diffusion length decreases considerably, even below 100 nm, being impossible to fabricate LSV devices with sepa-

ration between FM electrodes of this scale. The spin absorption (SA) technique is an alternative to this problem, by which the spin diffusion length is determined with a device based on a LSV [28].

The SA technique compares the spin signal measured in a conventional LSV to the spin signal measured on an identical LSV with a middle wire, the metal to study (MS), placed in between the injector and the detector (see Figs. 2.4(a) and 2.4(b)). The conventional LSV is a well known system, where a channel with a long spin diffusion length is chosen. If the MS has a low spin resistance, according to the conventional spin diffusion theory [29], it will provide an additional spin relaxation path and, therefore, part of the spin current diffusing in the channel will be absorbed into the middle wire. This will inevitably modify the detected voltage at the second FM electrode, which can be written as [9, 30]:

$$V_s^{abs} = 4IR_N\hat{\alpha}_1\hat{\alpha}_3 \frac{(r_2 - 1)e^{-L/\lambda_N}}{r_1r_2r_3 - r_1e^{-2(L-d)/\lambda_N} - r_2e^{-2L/\lambda_N} - r_3e^{-2d/\lambda_N} + 2e^{-2L/\lambda_N}} \quad (2.17)$$

with

$$r_k = \frac{1}{1 - P_{Ik}^2} \frac{R_{Ik}}{R_N} + \frac{1}{1 - \alpha_{Fk}^2} \frac{R_{Fk}}{R_N} + 1,$$

$$\hat{\alpha}_k = \frac{P_{Ik}}{1 - P_{Ik}^2} \frac{R_{Ik}}{2R_N} + \frac{\alpha_{Fk}}{1 - \alpha_{Fk}^2} \frac{R_{Fk}}{2R_N},$$

where $k=1,2,3$ refer to the FM injector, middle MS wire and FM detector, respectively; d is the distance from the FM injector to the MS (see Fig. 2.4(a)) and the rest of the parameters are the same as the ones defined in Eq. 2.10. Note that this equation is the most general case in which we are not considering if the middle MS wire is a ferromagnetic metal or not.

As the detected voltage changes due to the presence of the middle MS wire, then the measured spin signal will also change. In fact, as can be seen in Fig. 2.4(c), the spin signal that is detected in the LSV with the middle MS wire (ΔR_{NL}^{abs}) is smaller than the spin signal in the conventional LSV (ΔR_{NL}^{ref}). By normalizing ΔR_{NL}^{abs} to ΔR_{NL}^{ref} , if we assume that the middle MS wire is not a FM metal, we have transparent interfaces and the middle MS wire is located in the middle of both electrodes ($d = L/2$), we obtain:

$$\eta = \frac{\Delta R_{NL}^{abs}}{\Delta R_{NL}^{ref}} = \frac{Q_M \left\{ \sinh\left(\frac{L}{\lambda_N}\right) + Q_F e^{L/\lambda_N} + \frac{Q_F^2}{2} e^{L/\lambda_N} \right\}}{\left(\cosh\left(\frac{L}{\lambda_N}\right) - 1 \right) + Q_M \sinh\left(\frac{L}{\lambda_N}\right) + Q_F \left[e^{L/\lambda_N} \left(1 + \frac{Q_F}{2} \right) (1 + Q_M) - 1 \right]} \quad (2.18)$$

where Q_F and Q_M are defined as $Q_F = \frac{R_F}{(1-\alpha_F^2)R_N}$ and $Q_M = \frac{R_M}{R_N}$, being R_N , R_F and $R_M = \frac{\rho_M \lambda_M}{w_N w_M \tanh[t_M/\lambda_M]}$ the spin resistance of the NM channel, the FM and the middle MS wire, respectively.

η is related to the efficiency of the middle wire to absorb the spin current propagating through the channel. For example, having $\eta \approx 1$ means that the spin resistance of the middle wire is larger than the spin resistance of the channel and, thus, the spin currents will not be absorbed. Since all the parameters in Eq. 2.18 are known, except for the spin diffusion length of the middle wire, this can be easily calculated.

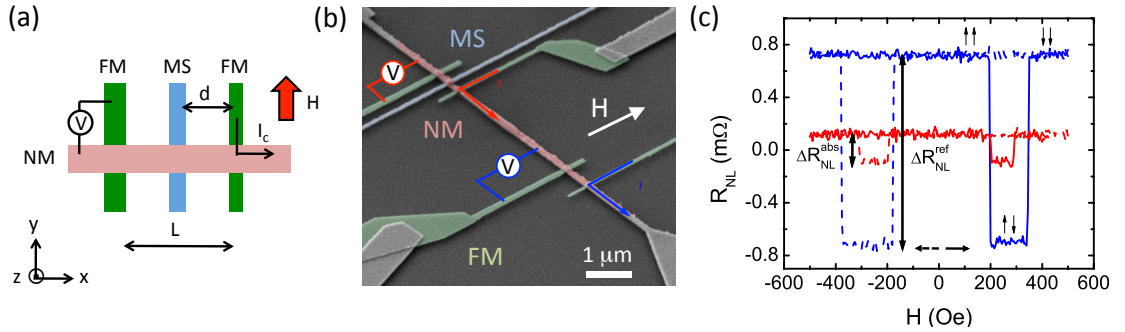


Figure 2.4: (a) Schematic representation of a LSV with a middle MS wire. The distance between the electrodes, L , the distance between the injector and the MS wire, d , the measurement configuration, the different materials (FM, NM and MS) and the applied magnetic field, H , are depicted. (b) SEM image of two LSVs. One of them is a conventional LSV and the other one has the metal to be studied (MS) in the middle of the FM electrodes. The magnetic field, the materials and the non-local measurement configuration are depicted. (c) Non-local resistance measured as a function of the field for the LSV without the middle MS wire in between the FMs (blue line) and the measurement in the LSV with the middle MS wire (red line). In this particular case the FM is Py, the NM is Cu, the middle MS wire is Pt $d= 320$ nm , $L= 630$ nm and $T=10$ K.

The SA technique enables determining the spin diffusion length of metals with strong SOC by just using two LSVs (the reference and the absorption one), provided that we have a reliable characterization of the FM and NM used in the LSVs.

2.1.3 Spin Hall devices

The same devices explained in the previous section (Section 2.1.2) can be used to determine the spin Hall effect (SHE) and its inverse (ISHE) [30–32]. The only consideration that has to be taken into account is that the measurement set up should be slightly changed, so that the external magnetic field is now applied in plane, perpendicular to the easy axis of the FM electrodes and the voltage is measured in the middle MS wire (Fig. 2.5(a) and Fig. 2.6 (a)). This way, when a charge current is injected from the FM electrode, the spin accumulation built at the FM/NM interface will diffuse away creating a pure spin current in the NM channel with the spins polarized in \hat{x} direction (Fig. 2.5(b)). When this spin current is absorbed into the middle MS wire ($-\hat{z}$ direction) it will be converted into a charge current in \hat{y} direction due to the ISHE, which will result on a measurable voltage (Fig. 2.6(b)).

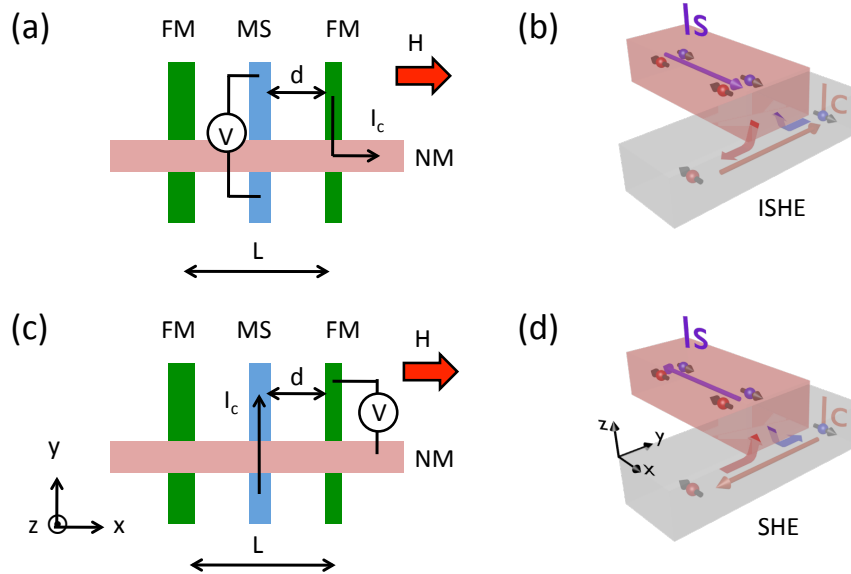


Figure 2.5: (a) Schematic representation of a spin Hall device. The geometrical parameters, different materials, the direction of the applied field and the measurement configuration to detect the ISHE are shown. (b) Schematic representation of the ISHE, where the conversion of a spin current, I_s , into a charge current, I_c , is shown. (c) Same as (a) but in this case the measurement set up is to detect the SHE. (d) Schematic representation of the SHE, where the conversion from charge current, I_c , into spin current, I_s , is depicted.

Note that only the x component of the spin polarization, \vec{s} , will contribute to the SHE. Therefore, when we sweep the applied field, while we are above the saturation field ($|H| > H_s$) we will have all the spins fully aligned along \hat{x} and, therefore, the largest measurable voltage will be detected at the middle MS wire. This is represented by the

flat regions in Fig. 2.6 (b) (red line), where the detected voltage is normalized to the injected current yielding a non-local resistance ($R_{ISHE} = \frac{V}{I_c}$). When we sweep the field below H_s ($|H| < H_s$) the spins will tend to align along the easy axis of the FM and, thus, the x component of \vec{s} will decrease. As can be seen in Fig. 2.6(b) (red line), the measured R_{ISHE} will decrease with decreasing the applied magnetic field. This behavior can be further confirmed by anisotropic magnetoresistance measurements of the FM electrode (Fig. 2.6 (c)). The change in R_{ISHE} between the two saturated regions at large negative and positive H is twice the spin-to-charge conversion signal ($2\Delta R_{SCC}$).

Reciprocally, the SHE can also be measured in the same device. In this case, a charge current is sent through the middle MS wire and this will create a spin accumulation at the MS/NM interface (Fig. 2.5(c)). This spin accumulation will be transferred through the NM and detected by the FM electrode (Fig. 2.5(d)). Therefore, the middle MS wire is acting in this case as a spin current source, whereas the FM electrode is the detector. If we plot the change in the detected voltage normalized to the injected current (R_{SHE}) when we sweep the magnetic field (blue line in Fig. 2.6 (b)), the charge-to-spin signal that we measure has the same magnitude of that reported for the ISHE, as expected from Onsager's reciprocal relations [31].

The spin Hall conductivity σ_{SH} is the spin current response to an electric field (see Section 1.2.1) and, for our device geometry, can be calculated from the detected spin-to-charge conversion signal as [30,32]:

$$\sigma_{SH} = \frac{1}{\rho_M^2} \frac{w_M}{x_M} \left(\frac{I_c}{\bar{I}_s} \right) \Delta R_{SCC}, \quad (2.19)$$

where w_M and ρ_M are the width and the electrical resistivity of the middle MS wire, respectively. I_c is the current injected at the FM electrode to create the pure spin current through the NM and \bar{I}_s is the spin current that is absorbed into the MS and therefore contributes to the ISHE. They are both related by:

$$\frac{\bar{I}_s}{I_c} = \frac{\lambda_M}{t_M} \frac{(1 - e^{-t_M/\lambda_M})^2}{1 - e^{-2t_M/\lambda_M}} \frac{I_s(z=0)}{I_c}, \quad (2.20)$$

where $I_s(z=0)$ is the effective spin current that reaches the MS wire and, in the most

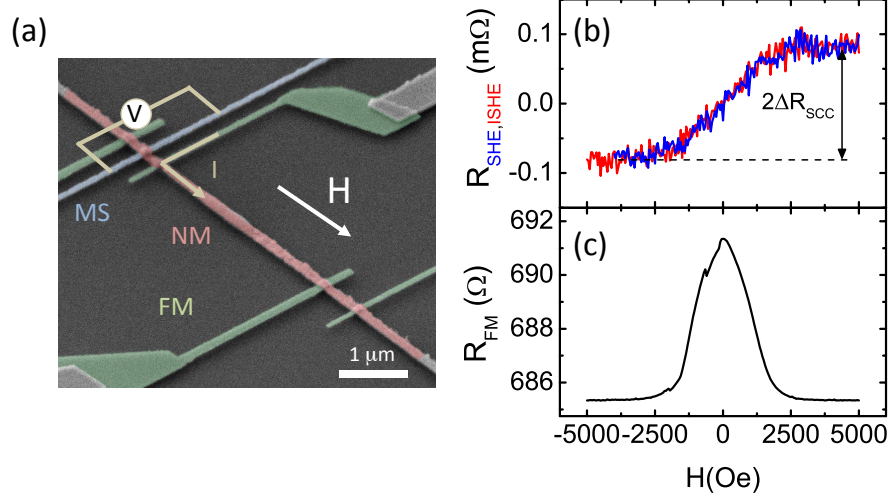


Figure 2.6: (a) SEM image of a spin Hall device. It is the same device used to measure the spin absorption, with a different measurement set-up. The magnetic field direction, the materials and the non-local measurement configuration are shown. (b) Non-local resistance measurement of the inverse spin Hall effect (red line) and spin Hall effect (blue line). The change in resistance from positive to negative fields gives the spin-to-charge conversion signal ($2\Delta R_{\text{SCC}}$) which is proportional to the spin Hall angle (Eq. 2.24). As expected from the Onsager's reciprocal relations, the magnitude of the SHE is the same as the magnitude of the ISHE. In this particular case, the SHE and ISHE are measured in Pt. (c) Anisotropic magnetoresistance of the FM electrode used for spin injection. The magnetic field is applied as shown in (a).

general case (Fig. 2.5 (a)) is given by:

$$\frac{I_s(z=0)}{I_c} = \frac{\alpha_F(Q_F \sinh\{(L-d)/\lambda_N\} + \frac{Q_F^2}{2} e^{(L-d)/\lambda_N})}{A} \quad (2.21)$$

with

$$A = \cosh(L/\lambda_N) - \cosh\{(L-2d)/\lambda_N\} + Q_F \sinh(d/\lambda_N) e^{(L-d)/\lambda_N} + Q_M \sinh(L/\lambda_N) + Q_F Q_M e^{d/\lambda_N} + Q_F e^{d/\lambda_N} \sinh\{(L-d)/\lambda_N\} + \frac{Q_F^2}{2} e^{L/\lambda_N} + Q_F^2 \frac{Q_M}{2} e^{L/\lambda_N}.$$

For the particular case where only one FM electrode is present in the device (Fig. 2.7), $I_s(z=0)/I_c$ is defined as:

$$\frac{I_s(z=0)}{I_c} = \frac{\alpha_F Q_F e^{d/\lambda_N}}{(Q_M + 1)(Q_F + 1)e^{2d/\lambda_N} - 1}. \quad (2.22)$$

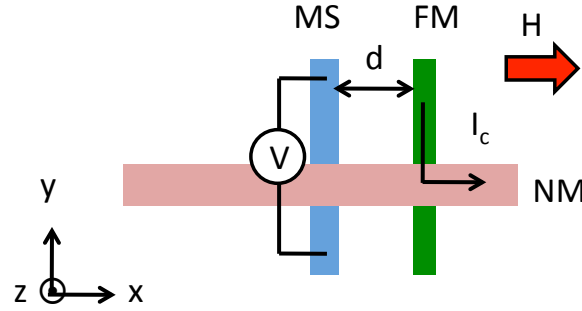


Figure 2.7: Schematic representation of a spin Hall device with only one FM electrode. The geometrical parameters, direction of the applied magnetic field and the measurement configuration to detect the ISHE are shown.

x_M in Eq. 2.19 is the shunting coefficient, which is a correction factor that takes into account the current that is shunted through the NM, due to the lower resistivity of the NM channel compared to the resistivity of the MS wire. This correction factor can be obtained from a different measurement in which the resistance of the MS wire is measured with and without a NM wire in between the voltage probes, as shown in Fig. 2.8.

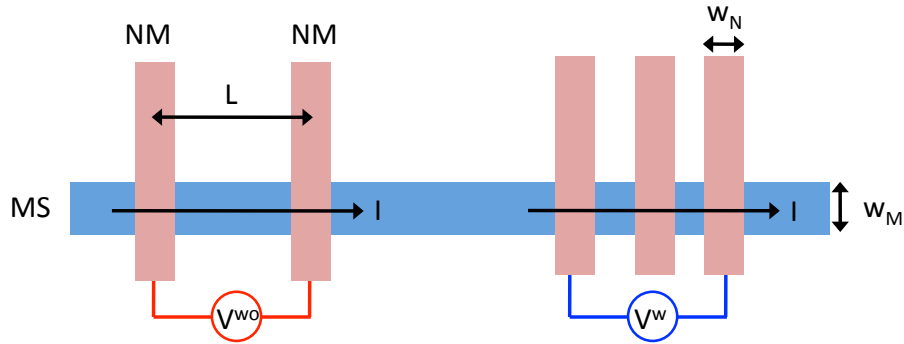


Figure 2.8: Schematic representation of the two necessary devices to estimate the shunting coefficient. The device in the left is the reference, whereas the one in the right, with the middle NM wire in between the voltage probes, measures the voltage drop due to the additional wire. Both devices have the same dimensions, where L is the separation between the voltage probes and w_N and w_M are the widths of the NM metal and MS, respectively. Note that all the NM are of the same width.

The shunting coefficient can be obtained by [32]:

$$\frac{V^w}{V^{w/o}} = \frac{L + 2w_N(x_M - 1)}{L + w_N(x_M - 1)}, \quad (2.23)$$

where V^w and $V^{w/o}$ are the voltages measured with and without the NM wire, respectively (see Fig. 2.8). Alternatively, it can be calculated using a finite elements 3D modeling which considers the resistivity and geometry of the MS wire and NM channel. This modeling allows us to calculate all the contributions coming from the lateral spreading of the current and the shunting effects around the contacts [30].

As explained in Section 1.2.1, the spin Hall angle, θ_{SH} , is intimately related to σ_{SH} . Therefore, we can deduce its value from Eq. 2.19:

$$\theta_{SH} = \frac{\sigma_{SH}}{\sigma_M} = \frac{w_M}{x_M} \frac{1}{\rho_M} \left(\frac{I_c}{\bar{I}_s} \right) \Delta R_{SCC}. \quad (2.24)$$

These two parameters, θ_{SH} and σ_{SH} , are essential to fully characterize the spin Hall effect.

2.1.4 Inverse Rashba-Edelstein devices

The inverse Rashba-Edelstein effect (IREE) is similar to the ISHE, but, in this case, we have that a three dimensional (3D) spin current will be converted into a two dimensional (2D) charge current in the surface of a 2D electron gas (2DEG) (Fig. 2.9). The parameter that determines the efficiency of the spin-to-charge current conversion is given by the inverse Rashba-Edelstein length, λ_{IREE} .

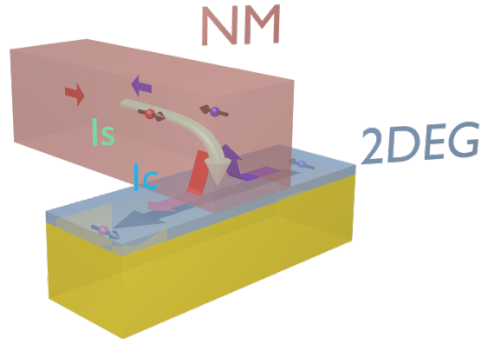


Figure 2.9: Schematic representation of the detection of the IREE, where a 3D spin current (I_s) is injected from a NM channel into a 2D electron gas (2DEG), creating a 2D charge current (I_c).

The device geometry that we use to detect this effect is the same as the one for the spin Hall effect (Fig. 2.6 (a)). However, the equations are slightly modified, as the spin-to-charge current conversion is not happening in the bulk any longer, but it will be an interfacial effect. Therefore, from the analogy with Eq. 2.24, λ_{IREE} is defined as:

$$\lambda_{IREE} = \frac{w_M}{x_M} \frac{1}{R_{sheet}} \frac{I_c}{I_s(z=0)} \Delta R_{SCC}, \quad (2.25)$$

where I_c is the injected charge current to create the 3D spin current and $\bar{I}_s(z=0)$ is the spin current reaching the 2DEG (defined in Eq. 2.21 or Eq. 2.22). In this case, instead of using the bulk resistivity, ρ_M , we use the sheet resistance of the 2DEG, R_{sheet} . Note that the origin of the spin-to-charge current conversion (ΔR_{SCC}) is not due to the bulk ISHE, but due to the IREE. The rest of the parameters (w_M and x_M) are the same as defined for the ISHE.

2.2 Hybrid NM/FMI bilayers

The spin Hall magnetoresistance (SMR), as explained in Section 1.2.1, is a newly discovered effect occurring at hybrid NM/FMI bilayers. It is manifested as a change in resistance of the NM depending on the magnetization direction of the FMI. Therefore, the SMR can be assessed by performing angle-dependent magnetoresistance (ADMR) measurements. For this purpose, the NM layer, grown on top of a FMI, is patterned into a Hall bar geometry (see sketches in Fig. 2.10). This geometry enables to perform ADMR measurements on longitudinal (Fig. 2.10(a-c)) and traverse configuration (Fig. 2.10(d)). The measured longitudinal, ρ_L , and transverse, ρ_T , resistivities in the NM/FMI bilayer due to SMR are described by the following equations [33, 34]:

$$\rho_L = \rho_N + \Delta\rho_1(1 - m_t^2), \quad (2.26)$$

$$\rho_T = \Delta\rho_1 m_j m_t + \Delta\rho_2 m_n, \quad (2.27)$$

where $\vec{m}(m_j, m_t, m_n) = \vec{M}/M_s$ are the cosine directors of the magnetization \vec{M} along the \hat{j} -, \hat{t} - and \hat{n} -directions; M_s is the saturation magnetization of the FMI; ρ_N is the electrical resistivity of the bulk NM layer; $\Delta\rho_1$ is the change in resistance due to the

SMR; and $\Delta\rho_2$ accounts for a Hall-like contribution to SMR. They are defined as:

$$\frac{\Delta\rho_1}{\rho_N} \approx \theta_{SH}^2 \frac{\lambda_N}{t_N} \frac{2\lambda_N G_r \tanh^2 \frac{t_N}{2\lambda_N}}{\sigma_N + 2\lambda_N G_r \coth \frac{t_N}{\lambda_N}}, \quad (2.28)$$

$$\frac{\Delta\rho_2}{\rho_N} \approx -\theta_{SH}^2 \frac{\lambda_N}{t_N} \frac{2\lambda_N G_i \tanh^2 \frac{t_N}{2\lambda_N}}{(\sigma_N + 2\lambda_N G_r \coth \frac{t_N}{\lambda_N})^2}, \quad (2.29)$$

where $\sigma_N = 1/\rho_N$, θ_{SH} , λ_N , and t_N are the electrical conductivity, the spin Hall angle, the spin diffusion length and the thickness of the NM metal, respectively, and $G_{\uparrow,\downarrow} = G_r + iG_i$ is the spin-mixing conductance at the NM/FMI interface, composed of a real, G_r , and an imaginary part, G_i . G_r is associated with the spin-transfer torque along $(\vec{m} \times \vec{\mu}_s) \times \vec{m}$, where \vec{m} is the magnetization direction of the FMI and the vector notation in $\vec{\mu}_s$ refers to the spin polarization of the spin accumulation at the interface. Therefore, G_r governs the efficiency of the spin injection [35–37]. G_i describes the precession of the spin accumulation $\vec{\mu}_s$ around \vec{m} and it is thus described by an "effective-field" torque pointing towards $\vec{\mu}_s \times \vec{m}$. G_i is usually an order of magnitude smaller than G_r and this makes it difficult to determine experimentally. However, SMR offers a promising platform to measure G_i [38].

Figure 2.10 shows the typical ADMR measurements, which are usually done at sufficiently high magnetic fields where the FMI magnetization is saturated, so that the magnetization follows the applied magnetic field. The measurements are done at three relevant H -rotation planes (α , β and γ), defined in sketches of Fig. 2.10. As expected from Eq. 2.26, the longitudinal resistance $R_L(\gamma)$ does not show any angular dependence (see Fig. 2.10(a)). Note that, if conventional anisotropic magnetoresistance ($\text{AMR} \approx \cos^2(\gamma)$) [39] was present in the NM due to a proximity effect with the FMI, a clear resistance change would be observed in this configuration. $R_L(\beta)$, plotted in Fig. 2.10(b), shows maxima for $\beta=0^\circ$ and 180° ($\vec{H} \parallel \hat{n}$) and minima for $\beta=90^\circ$ and 270° ($\vec{H} \parallel \hat{t}$) and can be described by $R_L(\beta) \approx \cos^2(\beta)$. This dependence agrees with the SMR prediction (Eq. 2.26) and excludes again AMR, which does not contribute since \vec{m} is always perpendicular to \vec{j}_c [39]. Similarly, $R_L(\alpha)$ data shown in Fig. 2.10(c) can also be described by $R_L(\alpha) \approx \cos^2(\alpha)$. In this configuration, both AMR [39] and SMR (Eq. 2.26) might contribute, but, as argued above, AMR has been found to be negligible and the observed α -dependence can be safely ascribed to SMR. The transverse resistance $R_T(\alpha)$, shown in Fig. 2.10(d), displays a $\cos(\alpha) \sin(\alpha)$ dependence, with maxima at 45°

and 225° (\vec{H} at 45° and 225° of \vec{j}_c) and minima at 135° and 315° . This behavior is fully consistent with Eq. 2.27. The ADMR for the other rotation planes, $R_T(\beta)$ and $R_T(\gamma)$, are not shown because the ordinary Hall effect in NM will be dominant over both the SMR ($\Delta\rho_1$) and the anomalous Hall-like term ($\Delta\rho_2$) in Eq. 2.27.

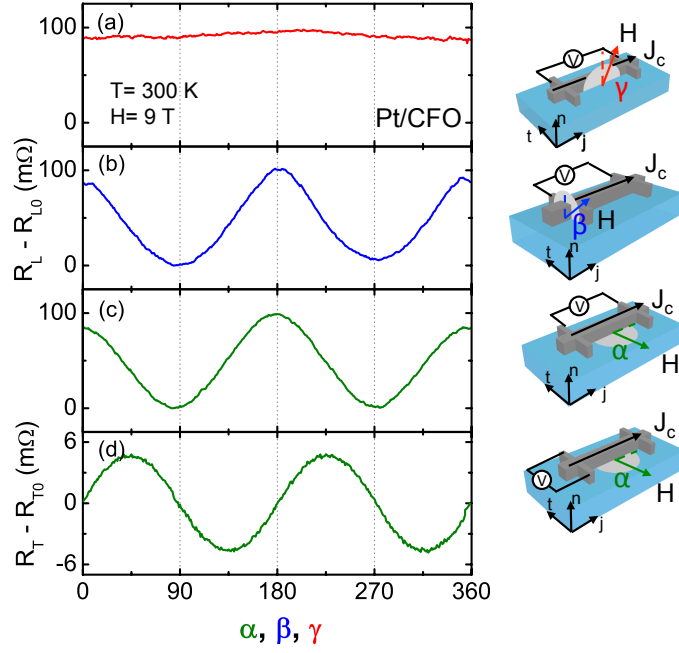


Figure 2.10: (a) Angle-dependent magnetoresistance measurements for a Pt/CoFe₂O₄(CFO) sample at 300 K and 9 T. $R_{L,T}$ is the measured resistance and $R_{L0,T0}$ is the subtracted background resistance. A schematic representation of the measurement set-up is placed next to each plot. (a-c) Longitudinal angle-dependent measurements where the magnetic field is rotated in three different planes (α , β and γ angles). (d) Transverse measurements where the field is varied in plane (angle α).

From Eq. 2.28, different parameters related to the NM metal, such as λ_N or θ_{SH} can be obtained by performing simpler measurements than those using LSVs. Moreover, one can also qualify the spin-mixing conductance of the NM/FMI interface which is a very important parameter on other many effects such as spin pumping and spin Seebeck effect [40].

References

- [1] N. F. Mott, *Proc. Roy. Soc. A* **153**, 699 (1936).
- [2] J. F. Gregg, I. Petej, E. Jouguelet and C. Dennis, *J. Phys. D: Appl. Phys.* **35**, R121 (2002).
- [3] J. Elliott *Phys. Rev.* **96**, 266 (1954).
- [4] Y. Yafet, in *Solid State Physics*, edited by F. Seitz and D. Turnbull (Academic, New York, 1963), pp. 1-98.
- [5] T. Valet and A. Fert, *Phys. Rev. B* **48**, 7099 (1993).
- [6] F. Casanova, A. Sharoni, M. Erekhinsky and I. K. Schuller, *Phys. Rev. B* **79**, 184415 (2009).
- [7] S. Takahashi and S. Maekawa, *Phys. Rev. B* **67**, 052409 (2003).
- [8] F. J. Jedema, M. S. Nijboer, A. T. Filip, and B. J. van Wees, *Phys. Rev. B* **67**, 085319 (2003).
- [9] H. Idzuchi, Y. Fukuma, and Y. Otani, *Phys. E* **68**, 239 (2015).
- [10] A. Fert and H. Jaffrès, *Phys. Rev. B* **64**, 184420 (2001).
- [11] A. Fert, J. -M. George, H. Jaffrès and R. Mattana, *IEEE Trans. Electron. Devices* **54**, 921 (2007).
- [12] G. Schmidt, D. Ferrand, L. W. Molenkamp, A. T. Filip and B. J. van Wees, *Phys. Rev. B* **62**, R4790 (2000).
- [13] E. I. Rashba, *Phys. Rev. B* **62**, R16267 (2000).

- [14] S. O. Valenzuela, D. J. Monsma, C. M. Marcus, V. Narayanamurti, and M. Tinkham *et al.*, *Phys. Rev. Lett* **94**, 196601(2005).
- [15] Y. K. Takahashi, S. Kasai, S. Hirayama, S. Mitani, and K. Hono, *Appl. Phys. Lett.* **100**, 052405 (2012).
- [16] G. Bridoux, M. V. Costache, J. Van de Vondel, I. Neumann, and S. O. Valenzuela, *Appl. Phys. Lett.* **99**, 102107 (2011).
- [17] K. Hamaya, N. Hashimoto, S. Oki, S. Yamada, M. Miyao and T. Kimura, *Phys. Rev. B* **85**, 100404(R) (2012).
- [18] F. J. Jedema, A. T. Filip, and B. J. van Wees, *Nature* **410**, 345 (2001).
- [19] T. Kimura, Y. Otani, and J. Harmle, *Phys. Rev. B* **73**, 132405 (2006).
- [20] T. Kimura, T. Sato and Y. Otani, *Phys. Rev. Lett.* **100**, 066602 (2008).
- [21] E. Villamor, M. Isasa, L. E. Hueso, and F. Casanova, *Phys. Rev. B* **87**, 094417 (2013).
- [22] E. Villamor, M. Isasa, L. E. Hueso, and F. Casanova, *Phys. Rev. B* **88**, 184411 (2013).
- [23] S. O. Valenzuela, and M. Tinkham, *Appl. Phys. Lett* **85**, 5914 (2004).
- [24] J. C. Rojas-Sánchez, P. Laczkowski, W. F. Savero-Torres, M. Cubukcu, V. D. Nguyen, L. Notin, C. Beigné, C. Vergnaud, A. Marty, M. Jamet, L. Vila, and J. P. Attané, *Appl. Phys. Lett* **102**, 132408 (2013).
- [25] R. Godfrey and M. Johnson, *Phys. Rev. Lett* **96**, 136601 (2006).
- [26] G. Mihajlović, J. E. Pearson, S. D. Bader, and A. Hoffmann, *Phys. Rev. Lett.* **104**, 237202 (2010).
- [27] Y. Fukuma, L. Wang, H. Idzuchi, S. Takahashi, S. Maekawa and Y. Otani, *Nature Mater.* **10**, 527 (2011).
- [28] T. Kimura, J. Hamrle and Y. Otani, *Phys. Rev. B* **72**, 014461 (2005).
- [29] A. Fert and S. F. Lee, *Phys. Rev. B* **53**, 6554 (1996).
- [30] Y. Niimi, H. Suzuki, Y. Kawanishi, Y. Omori, T. Valet, A. Fert, and Y. Otani, *Phys. Rev. B* **89**, 054401 (2014).

- [31] T. Kimura, Y. Otani, T. Sato, S. Takahashi and S. Maekawa, *Phys. Rev. Lett.* **98**, 156601 (2007).
- [32] Y. Niimi, M. Morota, D. H. Wei, C. Deranlot, M. Basletic, A. Hamzic, A. Fert and Y. Otani *Phys. Rev. Lett.* **106**, 126601 (2011).
- [33] H. Nakayama, M. Althammer, Y.-T. Chen, K. Uchida, Y. Kajiwara, D. Kikuchi, T. Ohtani, S. Geprägs, M. Opel, S. Takahashi, R. Gross, G. E. W. Bauer, S. T. B. Goennenwein and E. Saitoh, *Phys. Rev. Lett.* **110**, 206601 (2013).
- [34] Y. -T. Chen, S. Takahashi, H. Nakayama, M. Althammer, S. T. B. Goennenwein, E. Saitoh and G. E. W. Bauer, *Phys. Rev. B* **87**, 144411 (2013).
- [35] X. Jia, K. Lui, K. Xia, and G. E. W. Bauer, *Europhys. Lett.* **96**, 17005 (2011).
- [36] Z. Qiu, K. Ando, K. Uchida, Y. Kajiwara, R. Takahashi, H. Nakayama, T. An, Y. Fujikawa, and E. Saitoh, *Appl. Phys. Lett.* **103**, 092404 (2013).
- [37] M. Jungfleisch, V. Lauer, R. Neb, A. V. Chumak, and B. Hillebrands, *Appl. Phys. Lett.* **103**, 022411 (2013).
- [38] N. Vlietstra, J. Shan, V. Castel, J. Ben Youssef, G. E. W. Bauer and B. J. van Wees, *Appl. Phys. Lett.* **103**, 032401 (2013).
- [39] T. R. McGuire and R. I. Potter, *IEEE Trans. Magn.* **11**, 1018 (1975).
- [40] M. Weiler, M. Althammer, M. Schreier, J. Lotze, M. Pernpeintner, S. Meyer, H. Huebl, R. Gross, A. Kamra, J. Xiao, Y. -T. Chen, H. J. Jiao, G. E. W. Bauer and S. T. B. Goennenwein, *Phys. Rev. Lett.* **111**, 176601 (2013).

Chapter 3

Experimental techniques

In this chapter, we will give a general overview of the techniques which have been used to fabricate and characterize our devices. As described in Chapter 2, we will deal with two main types of device throughout this thesis: non-local devices and NM/FMI bilayers. Although they both share a common fabrication procedure, the details for each device are different. Therefore, the fabrication and characterization features for each type of device will be provided in their respective chapters.

3.1 Fabrication of devices

3.1.1 General procedure

The fabrication of devices consists of several consecutive steps that translate the design of a given device into a real structure. The patterning of the design can be done either by electron-beam lithography (eBL) or by photolithography, by irradiating a sensitive resist with electrons or light, respectively. The choice of the technique will depend on the feature size that we want to pattern, being eBL the tool that provides the highest resolution for patterning nanostructures. Throughout this thesis, given the nanometer size of the structures, we have chosen to use eBL and, thus, this is the process that is going to be briefly described. However, it is worth mentioning that photolithography has also been used for patterning macroscopic contacts.

The most basic fabrication procedure is composed of the following steps: spin-

coating of the electron-sensitive resist (positive or negative), irradiation of the resist with an electron beam, developing of the exposed patterns, deposition or etching of the material and resist lift-off (See Fig. 3.1). These steps are described in detail below.

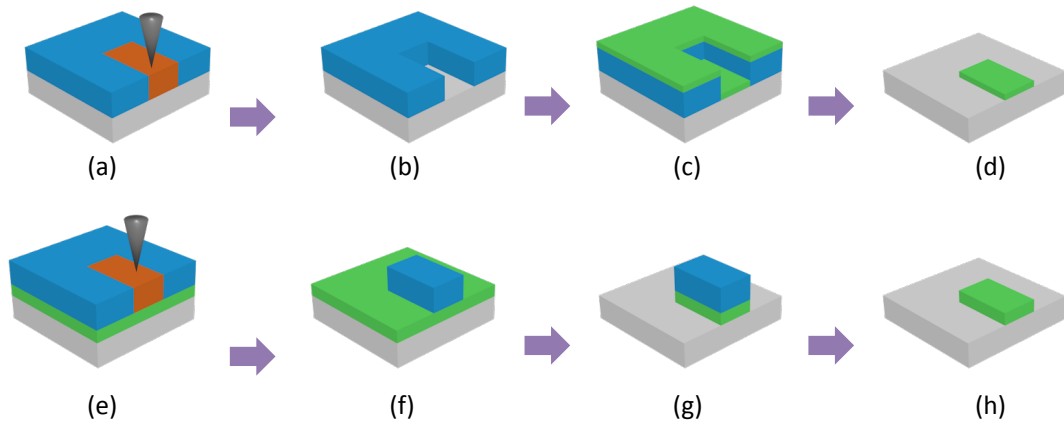


Figure 3.1: The main steps involved in the fabrication process using positive resist (a-d) or negative resist (e-h). (a) Exposure of the pattern on top of a positive resist. (b) Developing of the exposed part. (c) Material deposition. (d) Lift-off of the resist. (e) Exposure of the pattern on top of negative resist. (f) Developing process. Only the exposed part remains after this step. (g) Etching of the material that is not protected by the resist. (h) Lift-off to remove the resist.

Spin-coating

It consists on covering a substrate with an electron-sensitive polymer, commonly known as resist. Generally, the resist is classified in two main groups depending on the effect of the e-beam exposure: positive resist or negative resist. When the positive resist is irradiated with an electron beam, the polymer chain is modified (chain scission) and fragmented into smaller pieces (Fig. 3.1(a)), which are dissolved when immersed in a solvent (developing process). As a result the exposed area will be removed (Fig. 3.1(b)). The opposite occurs for the negative resist, where the polymer chain is cross-linked in the exposed area, creating an insoluble network (Fig. 3.1(e)). Therefore the exposed part remains after the developing (Fig. 3.1 (f)).

The lateral resolution of a resist, and, thus, the quality of the patterned nanostructure, is defined by its sensitivity to the electron beam, by its thickness and by the contrast, which defines how the resist is affected by the spatial distribution of the exposure energy [1]. The resist thickness can be controlled in the spin coating process and it will depend on the viscosity of the polymer and the rotation speed of the coater. The

resist thickness should always be thicker than the metal that is going to be deposited, for the positive resist case, or thick enough to endure the etching process for the negative resist case.

Another very important issue, specially when the material that is going to be deposited afterwards is a metal, is defining an appropriate strategy to avoid metal deposition on the sidewalls of the resist. This is usually done by using a double resist layer, where the bottom resist is more sensitive to e-beam exposure, resulting in an overexposed area and thus producing an undercut profile (See Fig. 3.2).

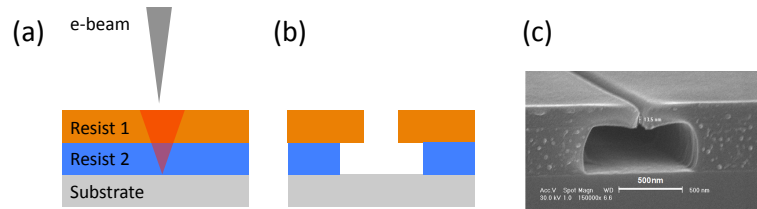


Figure 3.2: Schematic representation of the double layer strategy. (a) E-beam exposure of the double layer resist. Resist 2 has a lower molecular weight than resist 1. (b) Resist profile after the developing. (c) Scanning electron microscopy image of a real undercut. Figure adapted from Ref. [2].

Table 3.1 shows a list of common positive and negative resists used in this thesis and the purpose for their selection.

Table 3.1: Resists used in this thesis and the reason for being selected.

Resist	Purpose
495 PMMA A4	Used as a bottom layer for the undercut profile due to its low molecular weight.
950 PMMA A2	Used as the upper layer for the undercut profile for deposition of metals < 40 nm thick.
950 PMMA A4	Used as the upper layer for the undercut profile for deposition of metals > 40 nm thick.
ZEP 520A	High aspect ratio. Compared to PMMA, it can define more clearly the structures.
ma N-2403	Common negative resist, which can also be used as a photoresist.

Exposure

During the e-beam exposure, the pattern, a GDSII file previously designed using a CAD software, is transferred to the resist using an eBL equipment. The eBL system consists of two main parts: a scanning electron microscope (SEM) column and a sample holder stage. The SEM column is the responsible for generating the electron beam (either with thermionic or field emission electron source), focusing it and deflecting it in order to write the desired pattern. The beam is focused using some magnetic lenses and it has

to be centered in the middle of the column. Once this is fixed, the beam is deflected by means of some deflection plates and coils (Fig. 3.3(a)). This deflection enables to write the selected area (known as write field) while the stage is fixed. The other important part in an eBL system is the stage. In order to obtain a high resolution it is equipped with a laser interferometer that allows a precise control of the stage. This precision in the positioning enables stitching of write fields for large designs and making overlay exposures for multi-step lithography processes. The eBL system (beam control and writing process) is controlled by an external software.

Two eBL equipments were used in this work: *Raith 150-TWO* and *Raith e-line plus* (Fig. 3.3(b)). The main parameters that can be chosen in these eBL systems are the following:

- Acceleration voltage: it controls the energy of the electrons when reaching the stage. It can go from 100 V up to 30 kV, in 10 V steps.
- Aperture: it can take the following values: 7.5 μm , 10 μm , 20 μm , 30 μm , 60 μm and 120 μm . This parameter, together with the acceleration voltage, controls the current of the e-beam, which varies between 5 pA and 20 nA.
- Write field: it is the area in which the beam is deflected to write while the stage is fixed. This parameter has to be chosen carefully and a good write field alignment is necessary to avoid patterning mistakes in the limits of the different write fields. A smaller write field will give higher resolution for smaller patterns. But choosing a small write field for a big design can lead to stitching problems.
- Working distance: it is the distance between the column and the stage.
- Dose: the amount of charge per unit area that the resist receives. Typically it is given in $\mu C/cm^2$ and will be chosen depending on the type of resist that has to be exposed.

After the exposure, the samples are immersed into a solvent, called developer, which will dissolve the exposed part when using a positive resist, or the non-exposed part when using a negative resist. This is known as the developing process (Fig. 3.1 (b,f)).

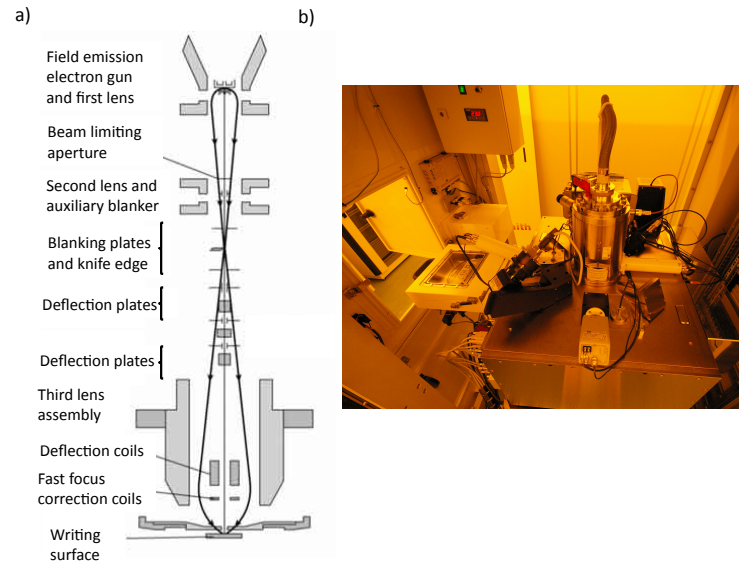


Figure 3.3: (a) Schematic representation of the SEM column in the eBL. (b) *Raith 150-TWO* equipment used in this work.

Material deposition/ etching

Once the pattern is transferred into the resist, we can have two different processes depending on the resist that we have used: an additive or a subtractive process.

The additive process takes place when the design is patterned into a positive resist (Fig. 3.1 (c)). In this case, a metal is deposited on top of the substrate and the resist. This can be done either by sputtering or by evaporation of the metal.

- Magnetron sputtering

Magnetron sputtering is a physical vapor deposition (PVD) technique. In this kind of deposition, a target made of the same material to be deposited is bombarded by energetic ions generated by a plasma situated in front of the target. The type of plasma that is selected for each deposition depends on the target, so that both (plasma and target) should have a similar atomic weight. The bombardment causes the removal of the target atoms, which expand over the whole chamber resulting in a non-directional deposition. They are deposited on the substrate forming a thin film. As a result of the ion bombardment, secondary electrons are emitted from the target surface but their motion is constrained by some magnetrons that create a magnetic field parallel to the target [3]. This can

be seen schematically in Figure 3.4 (a).

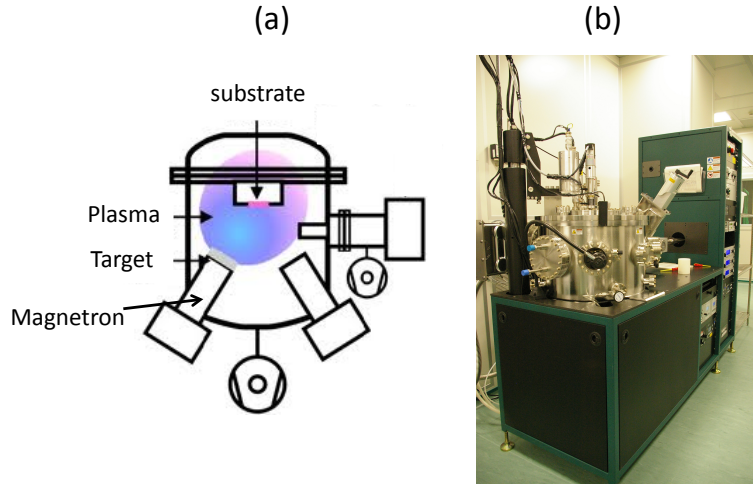


Figure 3.4: (a) Schematic representation of the magnetron sputtering process. (b) UHV 7-gun sputtering system by *AJA* used in this work.

The properties of the material that we grow on top of the substrate depend on the sputtering parameters. Therefore, controlling these parameters gives a large degree of possibilities to tune the microstructure of the deposited films.

In this work we have used a ultra high vacuum (UHV) 7-gun sputtering system by *AJA* consisting of a main chamber and a load lock that allows to load the sample without breaking the vacuum in the main chamber (see Figure 3.4 (b)). With this system, base pressures of the order of 10^{-8} Torr are reached.

- Evaporation

The evaporation process is a PVD technique that consists on heating the material to be deposited to the point where it melts and evaporates. This process takes place in a vacuum chamber where a substrate is located in the path of the evaporated atoms. Therefore, this technique is more directional than the magnetron sputtering.

One of the approaches to melt the metal to be deposited is by heating it with an electron beam. The electron beam is generated by a tungsten filament which emits electrons that are accelerated with a high voltage (of the order of kV). This electron beam is then focused and deflected with magnetic fields to the material we want to heat. When the electron beam hits the material it transfers energy, heating it above its melting point and evaporating it. This process can be seen

schematically in Figure 3.5 (a).

Another approach to melt the metal is by thermal evaporation. This can be done using effusion cells, where the material is inside a crucible, which is Joule heated (Figure 3.5 (b)).

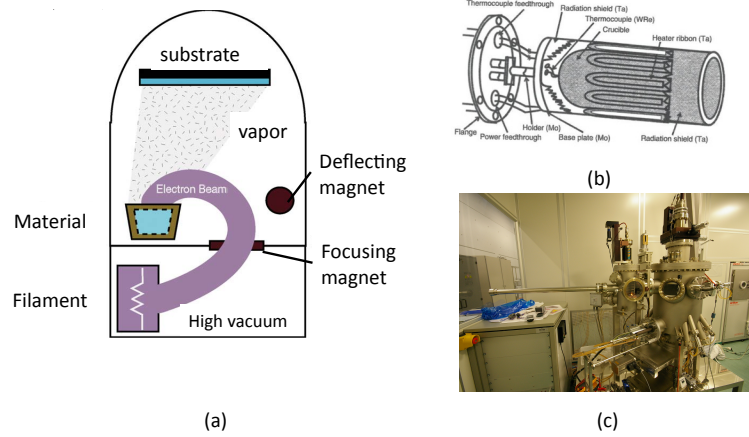


Figure 3.5: (a) Schematic representation of an e-beam evaporation process. (b) Schematic representation of an effusion cell. (c) UHV evaporator by *Createc* used in this work.

The evaporation system used in this work is a ultra high vacuum evaporator by *Createc* in which a load lock system maintains the main chamber at around 10^{-9} Torr base pressure (Figure 3.5 (c)). It contains an e-gun for e-beam evaporation and effusion cells for thermal evaporation.

In a subtractive process, the substrate is etched either by a physical etching, such as Argon-ion milling or by a chemical etching, so that everything which is not protected by the resist is etched away (Fig. 3.1 (g)).

- Ar-ion milling

An Ar-ion milling system can be used to etch a material by accelerating highly energetic Ar ions into it. Therefore, it is a purely physical process, *i.e.*, chemical reactions are not involved during the etching. This technique is highly anisotropic and there is no selectivity when etching different materials over the same substrate. An Ar-ion source is used in this technique which emits free electrons against Ar gas, creating Ar ions from the collision. Some of the ionized Ar atoms collide with

discharged chamber surfaces, where they recombine with electrons. Other ions that reach the ion optics are extracted through the apertures in the screen grid by the negative accelerator grid. Since the apertures in both grids are aligned, the extracted ions do not strike the accelerator grid, but continue on to form the ion beam. A neutralizer adds electrons to the ion beam to neutralize the positive charge of the ions. All the described elements can be seen in Figure 3.6 (a).

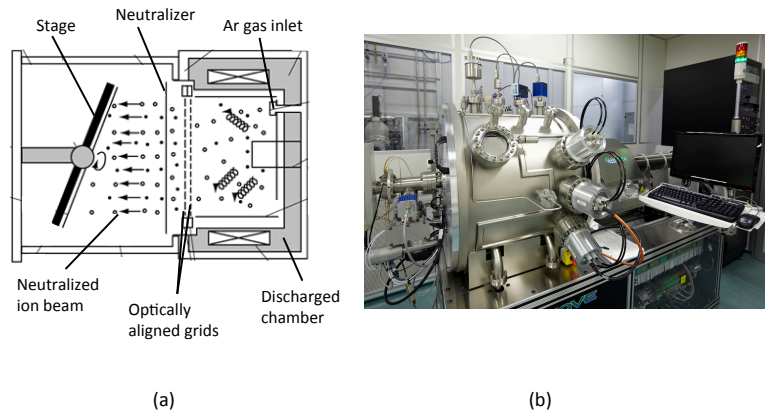


Figure 3.6: (a) Schematic representation of an Ar-ion milling process. (b) Ar-ion miller equipment by 4-WAVE used in this work.

The Ar-ion miller equipment by 4 WAVE used in this work has an inductive RF ion source to emit free electrons against the Ar gas (see Figure 3.6 (b)). Apart from the parameters that control the Ar-ion beam, there are some others to control the stage, such as the spinning and the tilting.

Lift-off

In this last step, the sample is immersed in a solvent, so that all the resist is dissolved. For the additive process, the metal in contact with the substrate will remain attached to it, whereas the metal on top of the resist will be removed, together with the resist (Fig. 3.1 (d)). For the subtractive process, the resist part that was protecting the structure from the etching process will be dissolved (Fig. 3.1 (h)).

3.1.2 Our devices

Before carrying out any fabrication step, we have to define the design that we want to pattern. There are several considerations that should be taken into account in order to design our devices:

1. Non-local devices

- The FM electrodes used in all the devices should have a well defined easy axis and a single domain, at least at the contact with the NM metal, to ensure an efficient injection. Therefore, FM electrodes with high aspect ratio (length/width ~ 5) will be fabricated.
- For LSVs and SA experiments, the FM electrodes should have different coercive fields to detect the parallel and antiparallel magnetization configurations by sweeping an external magnetic field. In this thesis, we have chosen to have electrodes with different widths for this purpose.
- For the particular case of LSVs, the separation between FM electrodes should be variable, so that we can detect the spin signal at different distances.
- For the particular case of SA technique, the separation between the FM electrodes in the LSV with the middle wire should be the same as the separation without the middle wire.

2. NM/FMI bilayers

- These devices are generally used to measure transverse resistance when a current is flowing through a Hall bar design. Therefore, it is necessary that the voltage probes are as narrow as possible compared to the current channel, so that the detected voltage is not affected by the flowing current.

Once the device is defined, we can proceed with the fabrication process. The different steps explained at the beginning of this section (Section 3.1) are repeated as many times as different metals are required for each device. For example, for hybrid NM/FM bilayers a single process is required, as only the patterning and deposition of the NM metal is needed. However, for the LSVs, the process will have to be performed twice, one for the patterning and deposition of the NM channel and the other for the FM electrodes. Last, for the case of SA devices, up to three processes are going to be

performed, as three different metals, the NM channel, the FM electrodes and the metal to study (MS), are going to be deposited.

When more than one metal is involved in the fabrication process, an additional step is introduced to ensure that the interface between the metals is transparent. This additional step consists of a gentle argon-ion milling which is performed before depositing the last metal. This cleans the interface from possible resist left-overs or oxide formation [4].

Moreover, to pattern the paths that contact the nanoscale device to the macro world, we have used photolithography. The steps are essentially the same as those described previously for the eBL patterning, with two slight differences. In this case, a photo sensitive resist is used and a optical mask (instead of a GDSII file) is necessary to pattern the design. This technique was chosen because it is less time consuming than eBL for patterning micrometer and millimeter size structures.

3.2 Characterization techniques

In the following sections we describe the methods and instruments used to electrically and morphologically characterize our devices.

3.2.1 Electrical characterization of devices

All the electrical measurements have been performed in a Physical Property Measurement System (PPMS) by *Quantum Design*, a liquid helium cryostat that allows achieving temperatures down to 1.8 K. Moreover, it is equipped with a superconducting magnet which can apply magnetic fields of ± 9 T (Figure 3.7 (a)).

Once the device is prepared, it is glued on a puck with eight different contacts where the electrical connections are done using copper wires that link the puck to the macroscopic pads of the device (manually bonded by cold indium pressing) (Fig. 3.7 (b)). The puck is pinned into a special sample rotator that is introduced into the cryostat, so that although the magnetic field is fixed in a given direction, the relative position between the magnetic field and the sample can vary (Figure 3.7 (c)).

The puck is connected to an automatic or manual switchboard, that enables to change the configuration of the voltage and current probes without taking the samples

out of the PPMS cryostat. The switchboard is connected to a nanovoltmeter (model 2182 by *Keithley*) and to a DC/AC current source (model 6221 by *Keithley*). Both measurement systems and the configuration of the cables in the automatic switchboard, as well as the temperature, magnetic field and sample position inside the PPMS, are controlled by a PC with LabVIEW software.

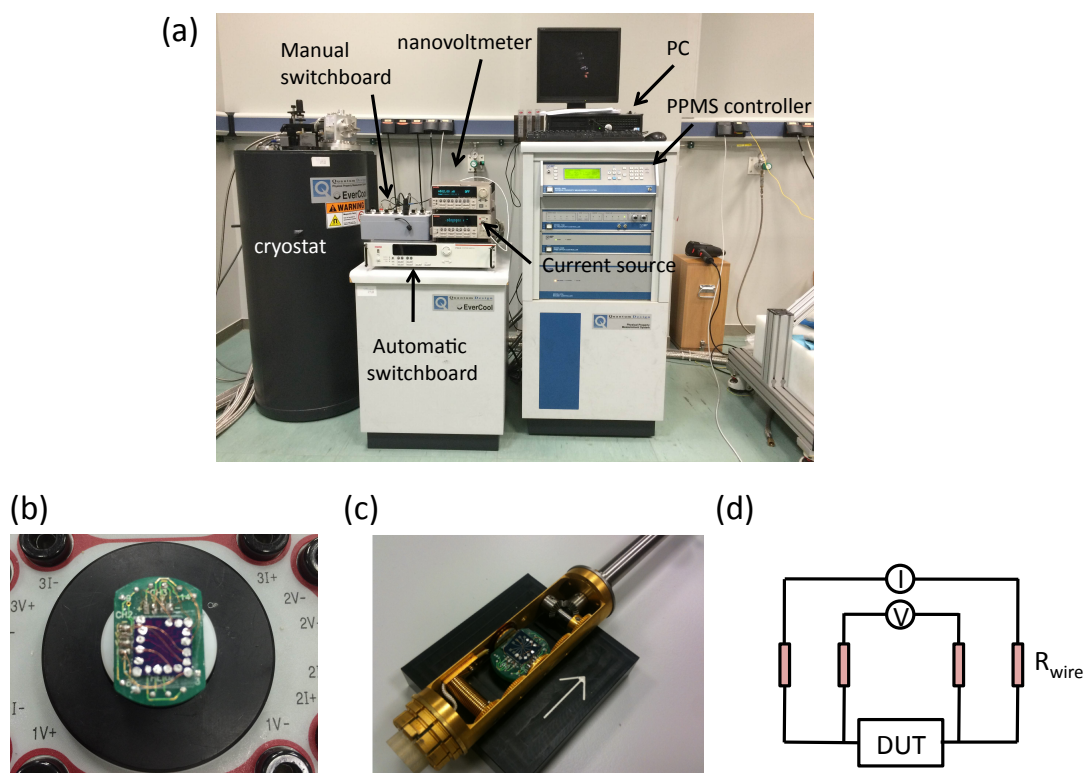


Figure 3.7: (a) PPMS equipment by *Quantum Design* and the measurement instruments (automatic and manual switchboards, nanovoltmeter and current source) used in this thesis. (b) A device glued in a puck and contacted to it by copper wires and indium. (c) Sample rotator with a device ready to be introduced into the cryostat. (d) Four-point measurement configuration.

Electrical transport measurements are performed by applying an electrical current and measuring the voltage drop. When measuring the resistance of a device under test (DUT), we can choose between a two-point or a four-point configuration. If a two-point configuration is chosen, as the voltmeter is integrated in the current source, there will be a significant error in the measured voltage due to the voltage drop coming from the wires and contacts of the current source circuit. If the resistance that we expect to measure from the DUT is of the order of $m\Omega$, as is the case of our devices, the two-point configuration measurements will largely distort our results. This problem is avoided if a four-point configuration is used instead, by connecting the voltmeter in parallel to the

current source and to the DUT (Figure 3.7 (d)). As the voltmeter resistance is typically above $1\text{ G}\Omega$, assuming that the measured resistance is the one of the sample is a good approximation:

$$\frac{1}{R_{Measured}} = \frac{1}{R_{Voltmeter}} + \frac{1}{R_{DUT}} \approx \frac{1}{R_{DUT}} \quad (3.1)$$

Apart from the parasitic noise coming from the resistance of the wires and contacts, there is another important contribution coming from the thermal noise. There are two approaches to suppress it: by using a DC reversal method or using a lock-in method (*i.e.*, using AC signals and filtering out all the frequencies except the one from the signal). In this work, the DC reversal method has been chosen because compared to lock-in techniques it has numerous benefits for the type of measurements we perform. First of all, DC techniques allow to execute a measurement with a given current polarity, which is not possible when we use AC signals. Furthermore, DC reversal method reduces the impact of error sources compared to lock-in techniques, as well as the time needed to achieve a low-noise measurement [5].

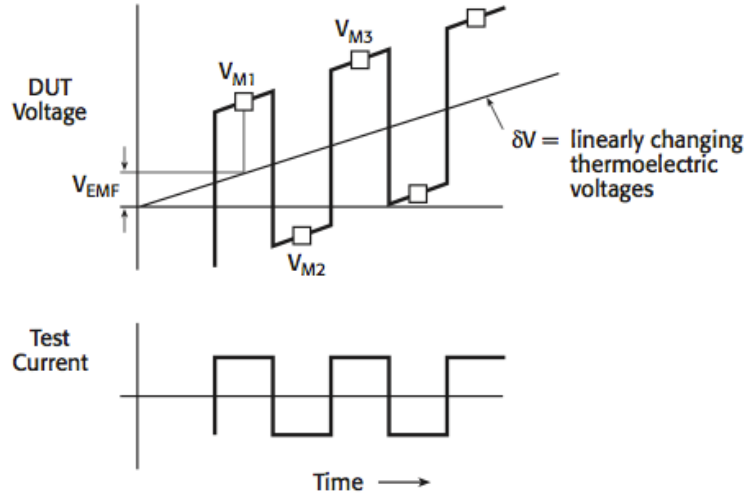


Figure 3.8: Schematic representation of the DC reversal technique. Figure taken from Ref. [5].

The DC reversal method works on the following way. It assumes that the thermoelectric voltage has two major contributions: a constant offset, V_{EMF} , and a linear contribution over time, δV . Therefore, if a DC current is applied, alternating the polarity, and three different voltage measurements are performed over a period of time, one can get:

$$V_{M1} = V_{DUT} + V_{EMF} \quad (3.2)$$

$$V_{M2} = -V_{DUT} + V_{EMF} + \delta V \quad (3.3)$$

$$V_{M3} = V_{DUT} + V_{EMF} + 2\delta V \quad (3.4)$$

where V_{EMF} and δV can be cancelled out in the following way:

$$V_A = (V_{M1} - V_{M2})/2 = V_{DUT} - \delta V/2 \quad (3.5)$$

$$V_B = (V_{M3} - V_{M2})/2 = V_{DUT} + \delta V/2 \quad (3.6)$$

If we now average between the two values, V_A and V_B , we will finally decouple the voltage drop over the device from the thermal noise:

$$V_{final} = (V_A + V_B)/2 = V_{DUT} \quad (3.7)$$

We generally measure the resistance as a function of the temperature, $R(T)$, the magnetic field, $R(H)$, and the rotation angle of the sample with respect to the magnetic field $R(\alpha)$.

3.2.2 X-ray diffraction

X-ray diffraction is a non-destructive technique for the investigation of the fine structure of matter. Although this technique was originally used to determine the crystal structure, the method is applied today for chemical analysis, stress measurements, study of particle size, determination of the orientation of a crystal, the film thickness, etc. [6]. In this work, we have used X-ray diffraction measurements to study the crystallographic quality of the epitaxially grown layers and reflectivity measurements to determine their thickness.

An X-ray equipment system *X' Pert PRO* by *PANalytical* has been used in this work. This diffractometer is equipped with a high stability X-ray generator tube, a very precise and reproducible goniometer (with an angular precision of 0.00001°) and a

detector which uses pixel detector technology. As the measurements are done with K_α radiation from copper, the K_β radiation is removed by means of filters. Figure 3.9 (a) shows the main parts of our X-ray equipment.

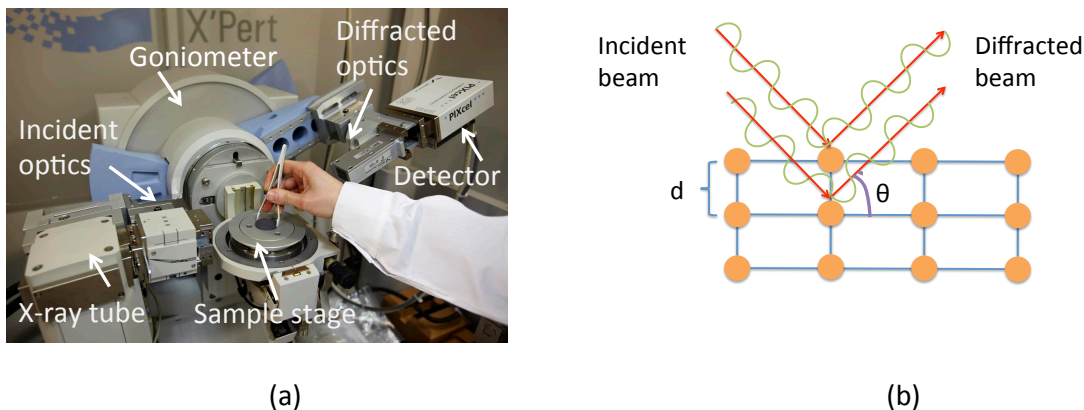


Figure 3.9: (a) The X-ray diffractometer used in this work with the different parts labeled. (b) Schematic representation of how X-rays scatter with a crystalline structure.

When X-rays strike a crystalline structure, the scattered X-rays will interfere constructively and destructively, producing a diffraction pattern which is characteristic for the specific crystalline structure of the material. According to Bragg's law, a constructive interference will occur only for a certain incident and observation angle θ if

$$n\lambda = 2d \sin \theta \quad (3.8)$$

where n is an integer, λ is the wavelength of the incident wave, d is the distance between the atomic planes and θ is the angle between the incident wave and the scattering planes. Figure 3.9 (b) shows a schematic representation where d and θ values can be visualized.

By scanning the incident and diffracted beam in different θ - 2θ angles, one will obtain a diffraction spectra as seen in Figure 3.10 (a). If the materials are polycrystalline, we will obtain a spectra with many peaks, being this spectra a fingerprint for each material. If the material is a single crystal, a unique peak will be observed, corresponding to the crystallographic plane of the single crystal.

However, $\theta - 2\theta$ scans are not enough to fully characterize the crystallographic structure of a sample, as these measurements do not take into account possible azimuthal orientation misalignment. In order to characterize this, one can perform ϕ

scans, being ϕ the rotation angle with respect to the axis normal to the surface plane. This measurement consists of scanning the sample fixing the incident and the diffracted beam and rotating the sample along ϕ .

Reflectivity measurements are performed at low θ angles. In this case, we will obtain the so-called Kiessig fringes (Figure 3.10 (b)). The separation between these fringes is determined by the thickness of the sample, while the slope that all these fringes define gives an estimation of the roughness.

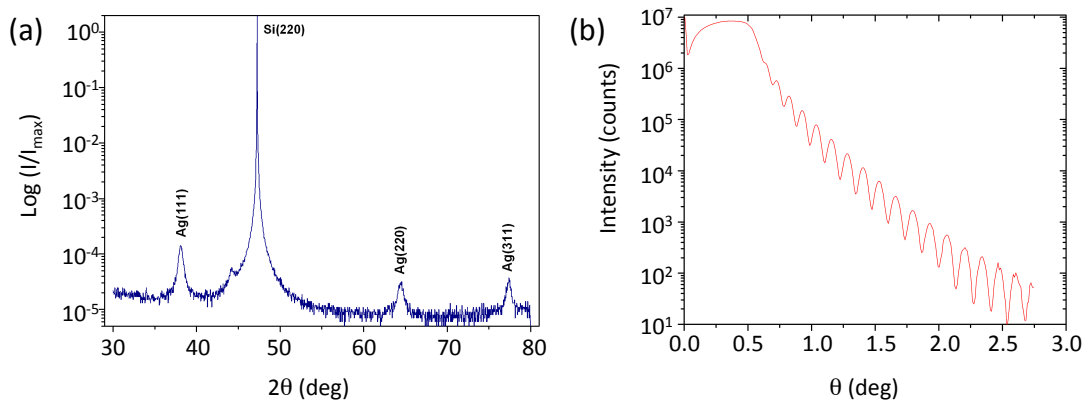


Figure 3.10: (a) X-ray diffraction measurement of a 40-nm-thick polycrystalline Ag thin film on top of a $\langle 110 \rangle$ Si substrate. (b) Intensity profile for the reflectivity measurement of a 30-nm-thick Au thin film.

3.2.3 Scanning electron microscopy

Scanning electron microscopy (SEM) has been used to measure the dimensions (length and width) of the fabricated nanodevices with nanometric resolution. SEM is a technique that creates images by focusing a high energy electron beam onto the surface of a sample and detecting the signals that are coming from the interaction of the incident electrons with the sample surface. The sample is scanned point by point and superposing the information obtained from each individual point the whole image is formed. Environmental *SEM Quanta FEG 250* has been used in this work.

References

- [1] H. J. Levinson, *Principles of lithography*, Second Edition (SPIE Press, 2005).
- [2] C. S. Wu, Y. Makiuchi, and C. Chen, in *Lithography*, edited by M. Wang (2010).
- [3] P. J. Kelly and R. D. Arnell, *Vacuum* **56**, 159, (2000).
- [4] E. Villamor, M. Isasa, L. E. Hueso, and F. Casanova, *Phys. Rev. B* **87**, 094417 (2013).
- [5] A. Daire, W. Goeke, and M. A. Tupta, "White Paper: New instruments can lock out lock-ins." *Keithley Instruments, Inc* (2005).
- [6] B. D. Cullity, *Elements of X-ray diffraction* **56**, Addison-Wesley Publishing Company, Inc. London, Second edition (1959).

Chapter 4

Spin transport in Ag

For an optimum performance of a spintronic device, it is crucial that spin information travels over long distances. This can be done by choosing materials with long spin diffusion length, λ_N , being copper (Cu) [1–11], aluminum (Al) [2, 6, 10, 12–14] or silver (Ag) [15–22] the most commonly selected metals. However, in order to further enhance λ_N we need to first understand which are the spin relaxation processes that lead to the loss of spin information. As seen in Section 2.1.1, the spin relaxation in NM metals is governed by the Elliott-Yafet (EY) mechanism [23,24], with phonons, grain boundaries, impurities or the surface being common sources for the associated spin-flip scattering [2, 4, 9–11, 18, 19]. A proper control of these contributions could thus help obtaining larger λ_N values.

In this chapter, we explore a way of diminishing the grain boundary contribution to the spin relaxation by controlling the growth conditions of Ag. For this purpose, we have fabricated $\text{Ni}_{80}\text{Fe}_{20}$ (permalloy, Py)/Ag LSVs (see Fig. 4.1(a)) where the Ag channel is grown in two different ways: epitaxially and polycrystalline. The epitaxial growth reduces the Ag grain misalignment as compared to the polycrystalline growth, enhancing transport phenomena. From non-local measurements we determine the spin transport properties of epitaxial Ag channel, which are superior to those from polycrystalline Ag.

4.1 Thin film growth and characterization

Thin films with 40 nm of epitaxial Ag were grown at room temperature by sputtering on a (110) Si substrate, after first removing the native Si-oxide by etching the Si-substrate with hydrofluoric (HF) acid [25, 26]. For comparison, a control sample was fabricated following the same process, except that Ag was deposited without pretreating the Si substrate with HF acid, thus leaving the native oxide and leading to a polycrystalline Ag channel structure [27]. The structural analysis of the Ag films was performed via X-ray diffraction (XRD) measurements (see Section 3.2.2). The crystal structure was checked by coplanar θ - 2θ XRD measurements and ϕ scans (Fig. 4.1(b) and (c)). For the case of epitaxial Ag, from the θ - 2θ scans only one diffraction peak at $2\theta \simeq 64.45^\circ$, corresponding to the Ag (220) atomic planes, was observed together with the (220) Si substrate diffraction (Fig. 4.1(b), red line). On the contrary, for the polycrystalline Ag case (Fig. 4.1(b), blue line), three different diffractions peaks were measured, being $2\theta \simeq 38.10^\circ$, which corresponds to Ag (111) atomic planes, the most pronounced peak. The in-plane orientation relationship between Si substrates and Ag thin films were investigated by means of XRD ϕ -scans at the $\{400\}$ poles for Si and at the $\{200\}$ for Ag. These ϕ scans clearly confirmed the epitaxial growth of Ag onto HF-etched Si. As clearly seen in Fig. 4.1(c), both the Ag (red solid line, bottom panel) and the Si substrate (black line, top panel) show two diffraction peaks, corresponding to the two $\{100\}$ poles, which are 180° apart and appear at the same absolute ϕ positions [24]. Regarding the ϕ scans for the polycrystalline Ag (Fig. 4.1(c), blue dashed line, bottom panel) only a more or less uniform background signal can be measured, as expected from a non-epitaxial structure. Furthermore, the average grain size for each sample can be extracted from the diffraction peaks by applying the Scherrer equation. From the (220) diffraction peak of the epitaxial Ag (Fig. 4.1(b)), a grain size of 41 ± 4 nm is obtained. On the other hand, using the same equation for the diffraction peaks of polycrystalline Ag, grain sizes of 15 ± 1 nm, 16 ± 2 nm and 26 ± 3 nm are obtained from the (111), (200) and (220) peaks, respectively, yielding an average value of 19 ± 6 nm.

4.2 Device fabrication

After the structural characterization, the Ag films were coated with negative resist and in an initial eBL step (see Section 3.1.1 for a description of the technique), a ~ 200 -

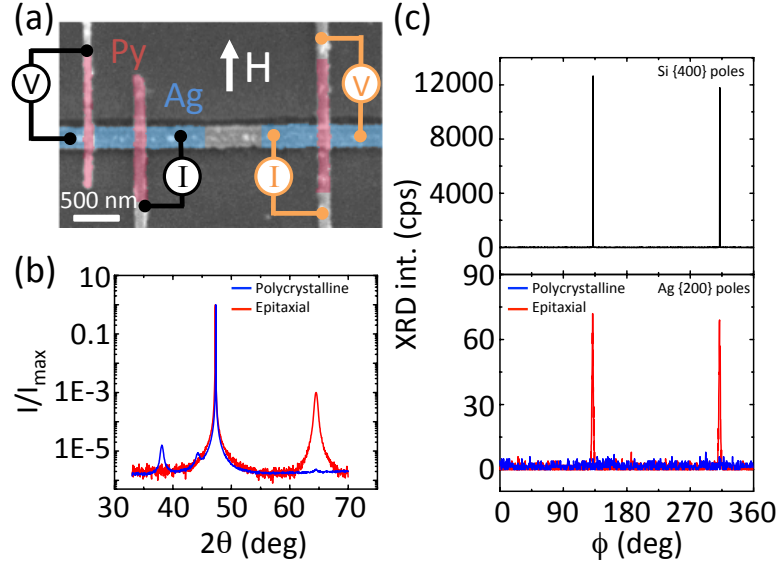


Figure 4.1: (a) SEM image of a Py/Ag LSV (left side) and a vertical Py bar on top of the Ag channel (right side), which was used to measure the interface resistance of Py/Ag. The FM and NM materials, the direction of the applied magnetic field and the non-local (black, left side) and interface resistance (orange, right side) measurement configuration are schematically depicted. (b) XRD θ - 2θ scan for the epitaxial Ag (red solid line) and polycrystalline Ag (blue dashed line). In the epitaxial case, the characteristic peak of Si (220) appears at $2\theta \simeq 47.30^\circ$ and the peak of epitaxial Ag (220) appears at $2\theta \simeq 64.45^\circ$. In the polycrystalline case, the characteristic peak of Si (220) appears at $2\theta \simeq 47.30^\circ$ and the peaks of Ag (111), Ag (200) and Ag (220) appear at $2\theta \simeq 38.1^\circ$, $2\theta \simeq 44.2^\circ$ and $2\theta \simeq 64.45^\circ$, respectively. Note that the Ag (220) peak in the polycrystalline case is not as pronounced as in the epitaxial case. (c) XRD ϕ -scans at the 2θ poles of the (100) planes of the Si substrate (top panel) and Ag thin films (bottom panel) for the epitaxial (red solid line) and polycrystalline (blue dashed line) cases.

nm-wide channel was patterned. Ag was removed with two consecutive Ar-ion etchings (Fig. 4.2(a)). In the first etching, Ar ions were accelerated almost perpendicularly (80° from in-plane orientation) to the Ag surface in order to remove the Ag that was not protected by the negative resist. In this first step, some etched Ag was redeposited at the edges of the channel, forming vertical walls of Ag that needed to be removed. Therefore, a second etching was performed without breaking the vacuum by accelerating Ar ions almost perpendicular to these Ag walls (10° from in-plane orientation). The suppression of the redeposited metal was confirmed by observing cross-sectional cuts, produced by means of focused ion beam (FIB) irradiation after the first (Fig. 4.2(b)) and the second etching (Fig. 4.2(c)). After these etching processes, the samples were immersed in acetone, so that all the resist was removed. In a second eBL step, the FM electrodes were patterned using a double layer of positive resist in this case. 45-nm-thick Py was e-beam evaporated at a pressure of $\leq 1 \times 10^{-8}$ mbar and the samples

were immersed in acetone for lift-off. Different Py electrode widths, ~ 110 nm and ~ 150 nm, were chosen in order to obtain different magnetic switching fields. Each sample contains several LSVs where the edge-to-edge distance L between the Py electrodes varied between 150 and 5500 nm.

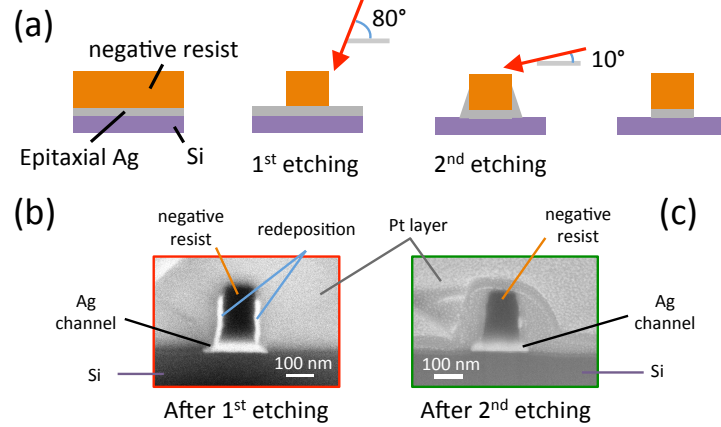


Figure 4.2: (a) Schematic representation of the two-step Ag milling. (b) Cross-sectional SEM image of the Ag channel just after the first etching. The vertical walls are redeposited Ag. (c) Cross-sectional SEM image of the Ag channel after the second milling. Vertical walls have been milled and the Ag channel has acquired the desired shape. Before cutting the cross sections by FIB, an initial e-beam induced deposition of Pt followed by ion-beam induced deposition of Pt was placed on top of Ag to protect the nanostructure, this is evident in the SEM images.

In Appendix A a more detailed description of the fabrication parameters used in each step are compiled.

4.3 Results

As shown in Section 2.1.1, by performing non-local measurements in a LSV (Fig 4.1(a)) one can evaluate the spin signal, ΔR_{NL} , for a given distance. Since ΔR_{NL} is proportional to the spin accumulation at the FM detector, it will decay upon increasing the distance L between the FM electrodes (Fig 4.3(b)). Therefore, by fitting ΔR_{NL} as a function of L to Eq. 2.14 λ_{Ag} and P_I can be obtained.

All the geometrical parameters on Eq. 2.14, such as the width or length of the devices, are determined by using a SEM and the thickness of the metals is controlled by the quartz monitor of the evaporation system and further confirmed by X-ray reflectivity on a thin film deposited together with each sample.

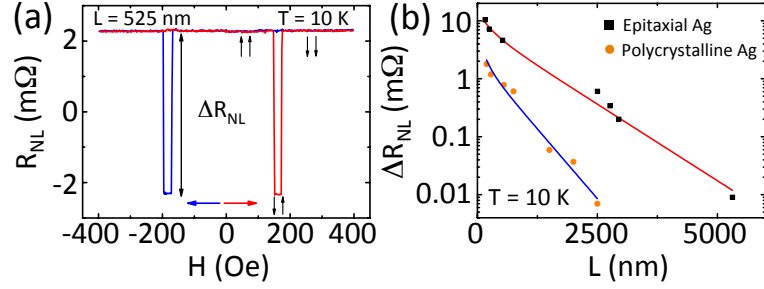


Figure 4.3: (a) Non-local resistance as a function of the applied magnetic field at 10 K for a Py/Ag LSV with epitaxial Ag where $L=525$ nm. The spin signal is tagged as ΔR_{NL} . (b) Spin signal as a function of the distance L between the electrodes at 10 K in Py/Ag LSVs. The solid black (orange) squares (circles) are the experimental data for the epitaxial (polycrystalline) Ag and the red (blue) line is the fit to Eq. 2.14 .

The resistance of the interface, R_I , is measured in the same device, in which the spin signal is obtained by using a cross-configuration that suppresses the contribution of the contacts, as shown Fig. 4.1(a) (orange line). The measured value, $R_I=60$ mΩ, is in agreement with a non-transparent interface present in Py/Ag as previously observed [16,20,22] and the approximation of Eq. 2.15 cannot be used. However, R_I is not large enough to use the approximation of Eq. 2.16, either. The resistivity of Ag is measured using a 4-point configuration, in which a current is sent through the Ag channel and a voltage is measured using the Py electrodes. Varying the distance L in between the electrodes, the resistance of Ag for every L is measured and performing a linear regression, ρ_{Ag} ($= 1.06 \mu\Omega cm$) is obtained. The resistivity of Py, ρ_{Py} ($= 22.4 \mu\Omega cm$), is measured separately in a device for which Py was grown under the same evaporation conditions. By setting $\lambda_{Py} = 5$ nm [28] and $\alpha_{Py} = 0.33$ [3,4,6] we fit our experimental data to Eq. 2.14 and we obtain the fitting parameters $P_I=0.47\pm 0.04$ and $\lambda_{Ag}=823\pm 59$ nm at 10 K for epitaxially grown Ag.

For comparison, the control sample with polycrystalline growth is electrically characterized in the same way. It yields a higher Ag resistivity, $\rho_{Ag} = 2.22 \mu\Omega cm$, a lower spin diffusion length, $\lambda_{Ag}=449\pm 30$ nm and a lower interface spin polarization $P_I=0.25\pm 0.03$ at 10 K which are comparable to other polycrystalline Ag samples reported in literature [17,18,21].

This substantial improvement in the spin diffusion length, by a factor of two, can be related to the decrease of the spin relaxation via grain boundary scattering [4,15]. As has been previously observed, the polycrystalline sample shows a considerably smaller

grain size in comparison to the epitaxial Ag. The smaller grain size implies having more grain boundaries, and consequently a higher resistivity and a shorter λ_{Ag} . Moreover, grains do not have a preferred crystallographic orientation for the polycrystalline Ag case, so that the existing grain boundaries are high angle grain boundaries, which also contributes to a higher resistivity. In contrast, the epitaxial growth of Ag strongly reduces the grain boundaries in the channel, which lowers the resistivity to $\rho_{Ag} \sim 1.07 \mu\Omega cm$ and increases λ_{Ag} . This dependence is in good agreement with the EY mechanism, which predicts $\lambda_{Ag} \propto 1/\rho_{Ag}$ as seen in Section 2.1.1. This mechanism is probably similar to what a thermal annealing might do to polycrystalline Ag. For LSVs where Ag has not been treated, $\lambda_{Ag} \simeq 550$ nm [17,18] is obtained, whereas values of $\lambda_{Ag} \simeq 1000$ nm have been reported after thermally treating the devices [15,21]. However, the advantage of controlling the Ag growth by means of epitaxy is that there is no need for additional thermal treatment, and given that the growth is done at room temperature, possible thermal diffusion between metals is avoided.

4.4 Conclusions

In conclusion, we have shown that the spin diffusion length in Ag can be substantially increased by controlling the growth process. When epitaxial Ag is grown, the grain boundary scattering is largely suppressed leading to lower resistivity values and higher spin diffusion lengths. The main advantage that this approach offers compared to an annealing treatment is that the growth process is done at room temperature. This avoids a possible diffusion of metals when the device is being heated. Proper engineering of the material used as a spin channel can thus improve the spin transport properties, and hereby help towards the development of devices based on pure spin currents.

References

- [1] F. J. Jedema, A. T. Filip and B. J. van Wees, *Nature* **410**, 345 (2001).
- [2] F. J. Jedema, M.S Nijboer, A. T. Filip and B. J. van Wees, *Phys. Rev. B* **67**, 085319 (2003).
- [3] E. Villamor, M. Isasa, L. E. Hueso and F. Casanova, *Phys. Rev. B* **88**, 184411 (2013).
- [4] E. Villamor, M. Isasa, L. E. Hueso and F. Casanova, *Phys. Rev. B* **87**, 094417 (2013).
- [5] Y. Ji, A. Hoffmann, J. E. Pearson and S. D. Bader, *Appl. Phys. Lett.* **88**, 052509 (2006).
- [6] F. Casanova, A. Sharoni, M. Erekhinsky and I. K. Schuller, *Phys. Rev. B* **79**, 184415 (2009).
- [7] T. Kimura, Y. Otani and J. Harmle, *Phys. Rev. B* **73**, 132405 (2006).
- [8] X. J. Wang, H. Zou, L. E. Ocola, R. Dican and Y. Ji, *Appl. Phys.* **105**, 093907 (2009)
- [9] M. Erekhinsky, A. Sharoni, F. Casanova and I. K. Schuller, *Appl. Phys. Lett.* **96**, 022513 (2010).
- [10] L. O'Brien, M. J. Erickson, D. Spivak, H. Ambaye, R. J. Goyette, V. Lauter, P. A. Crowell, and C. Leighton, *Nature comm.* **5**, 3927 (2014).
- [11] T. Kimura, and Y. Otani, *Phys. Rev. Lett.* **100**, 066602 (2008).
- [12] S. O. Valenzuela and M. Tinkham, *Appl. Phys. Lett.* **85**, 5914 (2004).
- [13] M. Johnson and R. H. Silsbee, *Phys. Rev. Lett.* **55**, 1790 (1985).

- [14] J. C. Rojas-Sanchez, *et al.*, *Appl. Phys. Lett.* **102**, 132408 (2013).
- [15] L. Wang, Y. Fukuma, H. Idzuchi, G. Yu, Y. Jiang and Y. Otani, *Appl. Phys. Express* **4**, 093004 (2011).
- [16] T. Kimura and Y. Otani, *Phys. Rev. Lett.* **99**, 196604 (2007).
- [17] Y. Fukuma, L. Wang, H. Idzuchi and Y. Otani, *Appl. Phys. Lett.* **97**, 012507 (2010).
- [18] G. Mihajlovic, J. E. Pearson, S. D: Bader, and A. Hoffmann, *Phys. Rev. Lett.* **104**, 237202 (2010).
- [19] H. Idzuchi , Y. Fukuma, L. Wang and Y. Otani, *Appl. Phys. Lett.* **101**, 022415 (2012).
- [20] G. Mihajlovic, D. K. Schreiber, Y. Liu, J. E. Pearson, S. D: Bader, A. K. Petford-Long and A. Hoffmann, *Appl. Phys. Lett.* **97**, 112502 (2010).
- [21] Y. Fukuma, L. Wang, H. Idzuchi, S. Takahashi, S. Maekawa and Y. Otani, *Nat. Mater.* **10**, 527 (2011).
- [22] R. Godfrey and M. Johnson, *Phys. Rev. Lett.* **96**, 136601 (2006).
- [23] R. J. Elliott, *Phys. Rev.* **96**, 266 (1954).
- [24] Y. Yafet, *Solid State Physics* edited by F. Seitz and D. Turnbull (New York: Academic, 1963)
- [25] W. Yang, D. Lambeth and D. E. Laughlin, *J. Appl. Phys.* **85**, 4723 (1999).
- [26] O. Idigoras, A. K. Suszka, P. Vavassori, P. Landeros, J. M. Porro and A. Berger, *Phys. Rev. B* **84**, 132403 (2011).
- [27] O. Idigoras, A. K. Suszka, P. Vavassori, B. Obry, B. Hillebrands, P. Landeros and A. Berger, *J. Appl. Phys.* **115**, 083912 (2014).
- [28] S. Dubois, L. Piraux, J. M. George, K. Ounadjela, J. L. Duvail and A. Fert, *Phys. Rev. B* **60**, 477 (1999).

Chapter 5

Spin transport and spin Hall effect in Au and Pt

As important as transporting pure spin currents over long distances, is the creation of such spin current without using ferromagnetic elements. This can be done by exploiting the spin Hall effect. As explained in Section 1.2.1, the SHE is present in metals with strong spin-orbit coupling (SOC), that is, with large atomic number, Z . However, as strong SOC values diminish the spin diffusion length (λ), the most appropriate materials would have a short λ . Therefore, instead of using Ag, which was characterized in the previous chapter, we will select two heavier elements. One is platinum (Pt); even though it is one of the prototype metals to exploit the SHE [1–4], there is still a big controversy regarding the magnitude of the spin Hall angle [5]. The other is gold (Au), which is interesting because very contradicting spin Hall angle values have also been reported [6–10]. In addition, Au shows a relatively large spin diffusion length in spite of a strong SOC [8, 11–13].

In this chapter, we will first focus on the spin transport properties of Pt and Au, using a different approach to the one seen in the previous chapter: the spin absorption (SA) technique. After determining the spin transport properties, we will use the same devices to measure the spin Hall effect. Finally, we will measure and analyze the temperature dependence of the spin Hall resistivity in order to separate the different contributions to the spin Hall effect for both metals.

5.1 Fabrication

The SA devices are structures based on a lateral spin valve (LSV) geometry. However, unlike lateral spin valves LSVs described in the previous chapter, they require three fabrication steps: the first step for the FM electrodes, the second for the middle wire (the metal to study, MS) and the third for the NM channel. In our case, we have fabricated our devices by multiple step eBL on top of a SiO₂ (150 nm)/Si substrate, followed by metal deposition and lift-off.

These devices consist of two Cu/permalloy (Py) LSVs, each one with the same separation in between the Py electrodes ($L \sim 630$ nm), one of them having a middle wire with the MS in between the ferromagnets (see Fig. 5.1(a)). In the first lithography step, the two pairs of FM electrodes are patterned with different widths, ~ 110 nm and ~ 160 nm, in order to obtain different switching magnetic fields and 35 nm of Py are e-beam evaporated. In the second lithography step, the MS wire in between the FM electrodes is patterned and Pt or Au are deposited. The 15-nm-thick and ~ 150 -nm-wide Pt wire is deposited by magnetron sputtering, whereas the 80-nm-thick and ~ 140 -nm-wide Au wire is grown by e-beam evaporation at a pressure of $\leq 1 \times 10^{-8}$ mbar. In this case, a 1.5-nm-thick Ti layer is deposited before Au in order to avoid adhesion problems. In the third lithography step, a ~ 150 -nm-wide NM channel is patterned and Cu is thermally evaporated at a pressure of $\leq 1 \times 10^{-8}$ mbar. Different Cu thicknesses of 60, 100 and 145 nm are used in the devices. Before the Cu deposition, the Py and MS wire surfaces are cleaned by Ar-ion milling to ensure transparent contacts.

All the fabrication parameters are described in detail in Appendix B.

5.2 Spin transport properties

As seen in Section 2.1.2, the spin diffusion length can also be extracted by comparing the spin signal measured in a conventional LSV, ΔR_{NL}^{ref} , to the spin signal measured in a LSV with the MS in between the FM electrodes, ΔR_{NL}^{abs} (see Fig. 5.1(b)). Since λ_{Cu} , λ_{Py} , ρ_{Cu} , ρ_{Py} and α_{Py} values for Cu and Py are well known from our previous work [14, 15], λ_M can be obtained from Eq. 2.18.

For MS=Pt, we measured $\rho_{Pt} = 25.0 \mu\Omega \text{ cm}$ ($39.7 \mu\Omega \text{ cm}$) at 10 K (300 K), which gives $\lambda_{Pt} = 3.4 \pm 0.3$ nm (2.0 ± 2.2 nm) (see Fig. 5.2(a) and inset). If we compare the

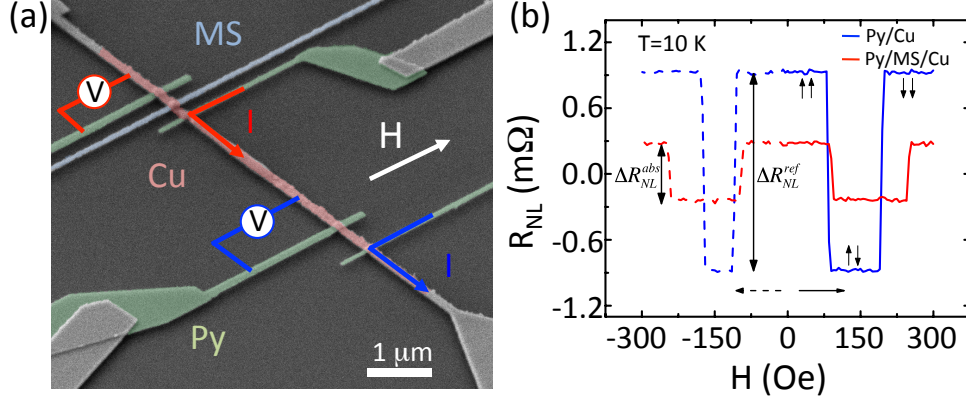


Figure 5.1: (a) Colored SEM image of two Py/Cu LSVs, one of them with a MS wire in between the Py electrodes. The measurement configuration, the direction of the applied magnetic field (H) and the different materials (Py, MS and Cu) are shown. (b) Non-local resistance as a function of H at 10 K for a Py/Cu LSV without (blue line) and with (red line) the MS wire in between the electrodes. The solid (dashed) line represents the increasing (decreasing) sweep of H .

λ_{Pt} value at low temperatures to the value measured by Morota *et al.* [4] with the same SA technique, we obtain a shorter value, most likely due to the fact that we have a 2.5 times more resistive Pt. The λ_{Pt} value at 300 K is comparable to values reported in literature using a different technique, spin pumping (SP) (1.2 - 3.7 nm, see Table 5.1).

For MS=Au, we measured $\rho_{Au} = 3.62 \mu\Omega \text{ cm}$ ($8.07 \mu\Omega \text{ cm}$) at 10 K (300 K), plotted in the inset of Fig. 5.2(b). We obtain $\lambda_{Au} = 21 \pm 1 \text{ nm}$ ($11 \pm 2 \text{ nm}$) at 10 K (300 K) being much smaller than the values reported in literature (see Table 5.1). This could be related to the used approximations in the spin resistance for Au. For R_M described in Eq. 2.18, we are assuming $w_{Cu} \gg \lambda_M$ [4]. However, this is not the case for Au, where $w_{Cu} \sim \lambda_{Au}$. Therefore, we need to determine the spin resistance for this particular case. From the general definition of the spin resistance seen in Section 2.1.1 ($R_s = \frac{\rho\lambda^2}{V}$), we can derive $R_{Au} = \frac{\rho_{Au}\lambda_{Au}^2}{w_{Au}t_{Au}(w_{Cu} + 2\lambda_{Au})}$, where we approximate the spin diffusion volume in the Au wire by $V = w_{Au}t_{Au}(w_{Cu} + 2\lambda_{Au})$. Using this intermediate expression for R_M in Eq. 2.18, we obtain $\lambda_{Au} = 53 \pm 2 \text{ nm}$ ($32 \pm 5 \text{ nm}$) at 10 K (300 K). These values are in better agreement with those reported in literature (see Table 5.1).

Obtaining an accurate value of λ_M is a matter of utmost importance to determine the correct magnitude of the SHE, as will be evidenced in the follow section.

Table 5.1: Spin diffusion length and spin Hall angle for Pt and Au extracted from the literature and this work using different methods (lateral spin valves=LSV, spin pumping=SP, spin-torque ferromagnetic resonance=ST-FMR, Hall Cross=HC and spin absorption=SA). Temperatures and resistivities are included.

Material	T(K)	$\rho(\mu\Omega \text{ cm})$	λ (nm)	$\theta_{SH}(\%)$	Method	Ref.
Pt	300	39.7	2.0 ± 2.2	1.5 ± 2.9	SA	This thesis
	300	-	1.4	9 ± 2	SP	[9]
	300	25	1.2	8.6 ± 0.5	SP	[16]
	300	20	1.4 ± 0.3	>5	ST-FMR	[5]
	300	41.3	3.7 ± 0.2	4^a	SP	[17]
	300	17.3 ± 0.6	3.4 ± 0.4	5.6 ± 1.0	SP	[18]
	10	25.0	3.4 ± 0.3	1.5 ± 0.3	SA	This thesis
	10	10	10 ± 2	2.4 ± 0.6	SA	[4]
	8	-	1.6	-	SP	[16]
Au	300	8.07	32 ± 5	<0.05	SA	This thesis
	300	5	35	0.25 ± 0.1	SP	[7]
	300	-	35	0.8 ± 0.1	SP	[9]
	295	3.89	36	<0.27	HC	[6]
	77	3.5	98	-	LSV	[13]
	15	4	85	-	LSV	[12]
	10	3.62	53 ± 2	0.22 ± 0.07	SA	This thesis
	10	-	63 ± 15	-	LSV	[11]
	10	4.0	33 ± 9	1.0 ± 0.2	SA	[8]
	4.5	2.07	65	<0.23	HC	[6]

^aThe value reported in the original paper is twice this value due to a factor of 2 difference in the θ_{SH} definition.

5.3 Spin Hall effect

Once we have settled the spin transport properties of Pt and Au, we will measure the ISHE using the same SA devices, but changing the measurement configuration as indicated in Fig. 5.3(a).

Figure 5.3(b) shows the non-local resistance, R_{ISHE} , measured in the MS wire as a results of the ISHE. As explained in Section 2.1.3, this non-local resistance should linearly increase with increasing the magnetic field and saturate above the saturation field of the FM injector, thus it should follow the magnetization of the injector (see Fig. 5.3(c)). The change in resistance between the two saturated regions is shown as ΔR_{SCC} in Fig. 5.3(b) and it is a fingerprint of ISHE in SA devices. We observe that ΔR_{SCC} is much larger for Pt than for Au, although the sign is the same for

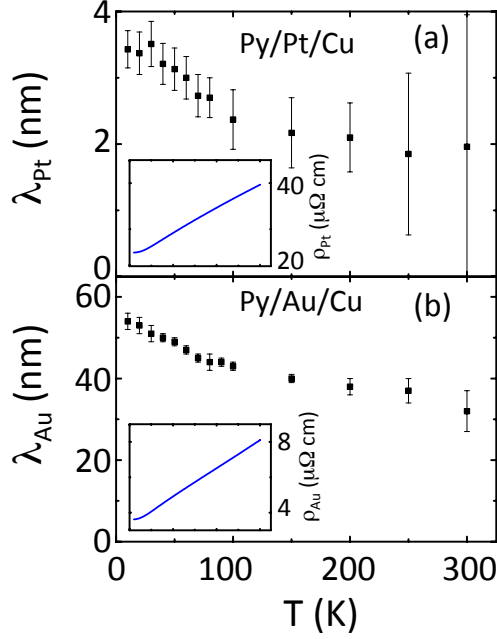


Figure 5.2: Spin diffusion length of (a) Pt and (b) Au as a function of temperature obtained from spin absorption experiments. Insets: (a) Pt and (b) Au resistivity as a function of temperature. Note that the temperature scale in the inset is the same as the one in the main figure.

both. As explained in Section 2.1.3, ΔR_{SCC} can be easily related to the spin Hall conductivity, σ_{SH} , by Eq. 2.19, or to the spin Hall resistivity, ρ_{SH} , using the definition in Eq. 1.4, $\rho_{SH} \approx -\sigma_{SH}/\sigma_M^2$. Therefore, we will be able to write the spin Hall angle in terms of either σ_{SH} or ρ_{SH} : $\theta_{SH} = \frac{\sigma_{SH}}{\sigma_M} = -\frac{\rho_{SH}}{\rho_M}$ (Eq. 1.12). These three related parameters, ρ_{SH} , σ_{SH} and θ_{SH} , give us complementary information of the effect. Indeed, θ_{SH} will give us its efficiency, whereas ρ_{SH} and σ_{SH} will be helpful to study the different mechanisms that contribute to the effect.

For the case of $MS = Pt$, two different SA devices have been measured, one with $t_{Cu} = 60$ nm and $d = 280$ nm and the other with $t_{Cu} = 100$ nm and $d = 310$ nm, where d is the distance between the Py injector and the Pt wire. As shown in Figs. 5.4(a) and 5.4(b), the geometrical parameters do not affect the obtained σ_{SH} and θ_{SH} values, demonstrating the consistency of the results using different devices. From the measurements at 10 K, we obtain $\theta_{SH} \approx 1.5 \pm 0.3\%$ in reasonable agreement with values reported using the same technique [4]. When increasing the temperature, σ_{SH} is constant, whereas θ_{SH} increases monotonically up to $\theta_{SH} \sim 1.5 \pm 2.9\%$ at 300 K. At this temperature, only θ_{SH} values determined by other techniques have been reported,

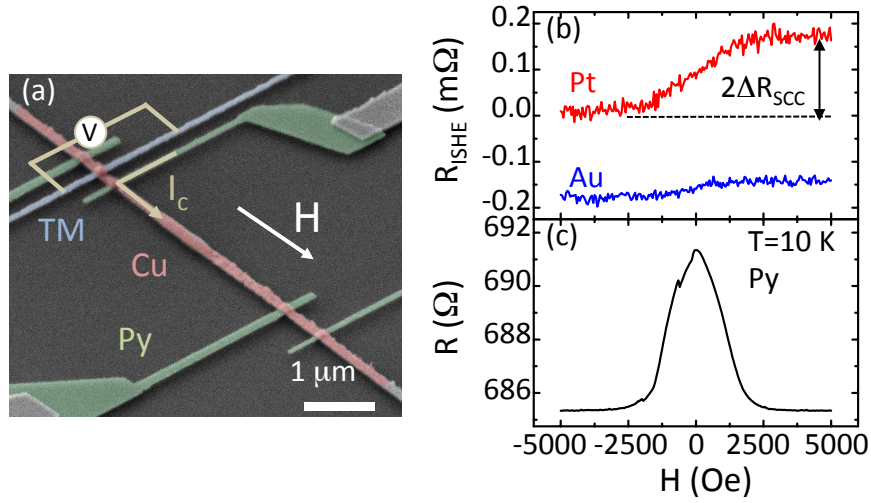


Figure 5.3: (a) Colored SEM image of the same device shown in Fig. 5.1 used now to measure the ISHE. The measurement configuration, direction of H and the different materials (Py, MS and Cu) are shown. (b) Non-local resistance for Pt (red) and Au (blue) as a function of H measured at 10 K in the ISHE configuration shown in (a). Note that the curves are shifted from 0 for the sake of clarity. (c) Resistance as a function of H , applied as shown in (a), for the Py electrode used for spin injection, measured at 10 K.

which are substantially larger (between 4% and 9%; see Table 5.1). This discrepancy between different techniques estimating the spin Hall angle is a long standing discussion [5]. However, recently, the spin memory loss (SML) has been suggested as a possible explanation [18] to reconcile the large dispersion in the published θ_{SH} values in Pt (Table 5.1). See Section 5.3.1 for a detailed discussion of SML.

For the case of MS = Au, we choose a 145-nm-thick Cu channel and two different distances ($d = 180$ nm and $d = 260$ nm) between the Py electrode and Au wire. As plotted in Figs. 5.4(c) and 5.4(d), reproducible σ_{SH} and θ_{SH} values as a function of temperature are obtained when varying d , showing consistent results with different devices. From measurements at 10 K, we obtain $\theta_{SH} \approx 0.21 \pm 0.07\%$. When increasing the temperature, both σ_{SH} and θ_{SH} decrease strongly and go below the measurable threshold for $T > 200$ K. This temperature dependence is similar to what is reported in Ref. [8], but with slightly lower values in our case. We thus expect $\theta_{SH} < 0.04\%$ at 300 K. Again, this value clearly differs from results obtained with the spin pumping technique, in which values between 0.25% and 0.8% at room temperature are reported (see Table 5.1). The possible role of SML is also discussed in Section 5.3.1.

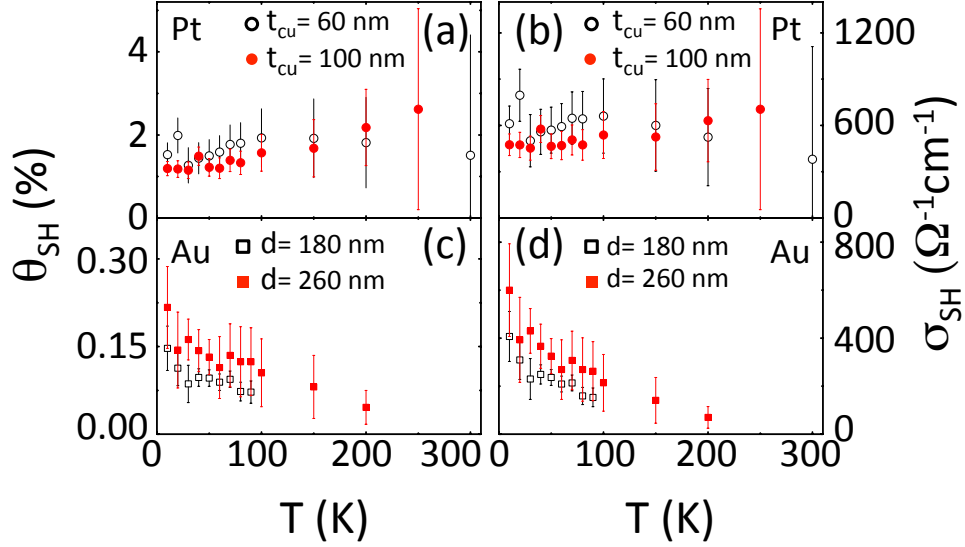


Figure 5.4: Spin Hall angle (a) and spin Hall conductivity (b) of Pt as a function of temperature obtained from two devices with $t_{Pt} = 15$ nm and different t_{Cu} (see legend). Spin Hall angle (c) and spin Hall conductivity (d) of Au as a function of temperature obtained from two devices with $t_{Au} = 80$ nm and different d (see legend).

5.3.1 Possible role of spin memory loss

The SML is a phenomenon occurring in disordered interfaces, where the spin current gets partially depolarized and, consequently, it is dissipated at the interface. This means that if we have systems with SML, which are usually those formed by $3d/5d$ interfaces (Cu/Pt and Cu/Au among them), both λ_M and θ_{SH} will be affected. First, if we have SML, the spin diffusion length that we obtain from SA experiments would be underestimated, as part of the spin current is partially depolarized at the interface. To take this depolarization into account, we should analyze the $3d/5d$ interfaces as if they were trilayers formed by the $3d$ metal, the interface and the $5d$ metal (Cu|interface|MS, see Fig. 5.5).

When the spin current diffusing along the Cu is absorbed into the MS wire, the spin current will go through the interface first. Therefore, when defining the spin resistance, we will have to take into account the series resistance (R_{series}) of the interface (R_I) and the MS layer (R_M). The spin resistance in a series connection is given by [18, 19]:

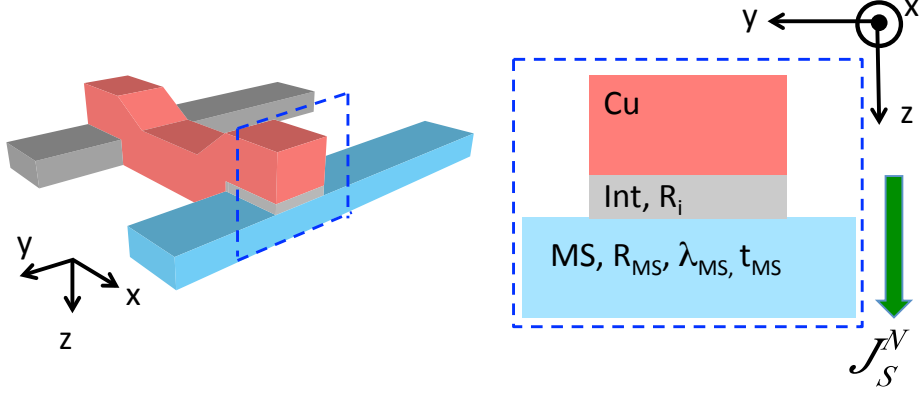


Figure 5.5: Schematic representation of a device and its transverse cut where the Cu channel, an interfacial layer and the MS wire are presented. The interfacial layer is inserted to take into account the spin memory loss.

$$R_{series} = \frac{R_I R_M \cosh[\delta] + \frac{R_I}{\delta} \sinh[\delta]}{\delta R_M \sinh[\delta] + \frac{R_I}{\delta} \cosh[\delta]}, \quad (5.1)$$

where, assuming the SML hypothesis, the R_{series} is the measured spin resistance in the spin absorption experiment and R_M should be the spin resistance of the MS, considering the real λ_M instead of the underestimated one. δ in Eq. 5.1 is the spin-flip parameter, a phenomenological value which governs the SML and R_I is the interface resistance. Assuming that δ and R_I are known and that R_{series} is directly measured in the SA experiment, one can obtain the real λ_M .

The other parameter that gets underestimated due to SML is the spin Hall angle. If we define the SML parameter, r_{SML} , which is the ratio between the spin current injected from the 3d metal (j_s^{NM}) and the current that reaches the 5d metal (j_s^{MS}) after being depolarized at the interface, we will be able to estimate the real θ_{SH} . r_{SML} is defined as:

$$r_{SML} = \frac{j_s^M}{j_s^N} = \frac{\frac{R_I}{\delta}}{R_M \sinh(\delta) + \frac{R_I}{\delta} \cosh(\delta)}. \quad (5.2)$$

The SML ratio should thus be inserted into Eq. 2.24 in the following way:

$$\theta_{SH} = \frac{1}{r_{SML\rho M}} \frac{w_M}{x_M} \left(\frac{I_c}{\bar{I}_s} \right) \Delta R_{SCC}. \quad (5.3)$$

Lets see what happens when we apply Eq. 5.1 and Eq. 5.3 to calculate the real λ_M and θ_{SH} , respectively. For the case of MS = Pt, the R_I that we measure in our devices is negative, meaning that R_I is of the order or lower than the resistance of the metals forming the interface [20, 21], $R_I A < 3 f\Omega m^2$ in our case, where A is the area of the interface. Therefore, it can be considered as a transparent interface and consequently SML could be neglected. If we anyway take $R_I A = 1.5 f\Omega m^2$ and $\delta = 0.9$ values from literature [22], we see that there is no possible solution for λ_{Pt} to fulfill Eq. 5.1. This means that the interface parameters that we have taken from literature (R_I and δ) are not characteristic of our Pt/Cu interface. Therefore, we cannot safely ascribe a value to θ_{SH} by correcting the SML contribution.

For MS = Au, as in the case of Pt, we also measure a negative interface resistance for Cu|Au, meaning that $R_I A < 6 f\Omega m^2$ in this case. If we anyway consider SML taking $R_I A = 0.3 f\Omega m^2$ and $\delta = 0.13$ values from literature [22], there is not a possible solution to satisfy Eq. 5.1. However, as stated for Pt/Cu, the reported values for Au/Cu might not be representative of our particular interface, and thus we cannot obtain a proper θ_{SH} value derived from SML.

We should emphasize that these δ and R_I literature values for the interfacial properties are obtained from thin film multilayers, whose interface might be very different to the interface formed between nanowires, as in our case. Therefore, even if SML might be a reason for the underestimation of λ_M and θ_{SH} , we believe its quantification is not trivial.

5.3.2 Mechanisms contributing to the SHE

In order to gain a deeper understanding of the mechanisms behind the SHE, we look into its temperature dependence. Whereas the intrinsic mechanism is related to the band structure of the metal, extrinsic mechanisms could include skew scattering and side jump [23]. Up to now, the intrinsic mechanism has been reported to dominate over extrinsic mechanisms in 4d and 5d transition metals, such as Nb, Ta, Mo, Pd, and Pt [4, 24]. In our metallic systems, with low impurity concentrations, the skew scattering

mechanism dominates over side jump [25, 26]. Therefore, only skew scattering will be taken into account as extrinsic contribution. In analogy to the AHE, the total spin Hall conductivity is calculated by considering the intrinsic and extrinsic contribution as parallel channels ($\sigma_{SH} = \sigma_{SH}^{int} + \sigma_{SH}^{ext}$) and the various extrinsic scattering mechanisms, impurities and phonons, as independent scattering sources forming a serial resistor circuit ($\rho_{SH}^{ext} = \rho_{SH}^{imp} + \rho_{SH}^{phon}$) [27, 28]. This leads us to

$$\sigma_{SH} = \sigma_{SH}^{int} + \sigma_{SH}^{ext} = \sigma_{SH}^{int} - \frac{\rho_{SH}^{imp} + \rho_{SH}^{phon}}{(\rho_M^{imp} + \rho_M^{phon})^2 + (\rho_{SH}^{imp} + \rho_{SH}^{phon})^2} \quad (5.4)$$

where ρ_M^{imp} and ρ_M^{phon} are the impurity and phonon contributions to the total resistivity, respectively ($\rho_M = \rho_M^{phon} + \rho_M^{imp}$). Taking into account that $\rho_{SH} \ll \rho_M$, we can rewrite Eq. 5.4 as

$$\sigma_{SH} = \sigma_{SH}^{int} - \frac{\rho_{SH}^{imp} + \rho_{SH}^{phon}}{\rho_M^2} \quad (5.5)$$

In the case that the intrinsic term dominates ($\sigma_{SH}^{int} \gg \frac{\rho_{SH}^{ext}}{\rho_M^2}$), σ_{SH} is independent from the mean free path for scattering and θ_{SH} depends on ρ_M in the form of $\theta_{SH} \propto \rho_M$. Therefore, σ_{SH} is temperature independent and θ_{SH} will increase linearly with T . This is the behavior that we observe for Pt (Figs. 5.4(a) and 5.4(b)) confirming that the intrinsic contribution is dominant. However, the decrease of σ_{SH} and θ_{SH} that we observe with T for the case of Au (Figs. 5.4(c) and 5.4(d)) cannot be explained by a dominating intrinsic contribution. Similar experimental results with a strong temperature dependence of θ_{SH} in Au have been recently reported by Niimi *et al.* [8], although the effect is attributed to an intrinsic mechanism.

Realistically, we have to take into account both intrinsic and extrinsic contributions, which we will quantify for Pt and Au. In order to extract the individual contributions, we rewrite Eq. 5.5 in terms of ρ_{SH} assuming, in a first approximation, that phonon skew scattering, ρ_{SH}^{phon} , is negligible for the spin Hall resistivity [29]:

$$-\rho_{SH} = \sigma_{SH}^{int} \rho_M^2 - \rho_{SH}^{imp} \quad (5.6)$$

This equation is analogous to the one derived for the AHE (Eq. 1.7). However, instead of using the skew-scattering constant, a_{ss} , we have written it in terms of ρ_{SH}^{imp} ,

being $a_{ss} = \rho_{SH}^{imp} / \rho_M^{imp} \approx -\sigma_{SH}^{imp} / \rho_M^{imp}$.

If we plot $-\rho_{SH}$ against ρ_M^2 , we can directly fit a linear function in which the slope gives the magnitude of the intrinsic contribution and the onset the extrinsic one (Figs. 5.6(a) and 5.6(b)). The values that we extract from this fitting are summarized in Table 5.2, where the relation $\sigma_{SH}^{imp} \approx -\rho_{SH}^{imp} / (\rho_M^{imp})^2$ has been used.

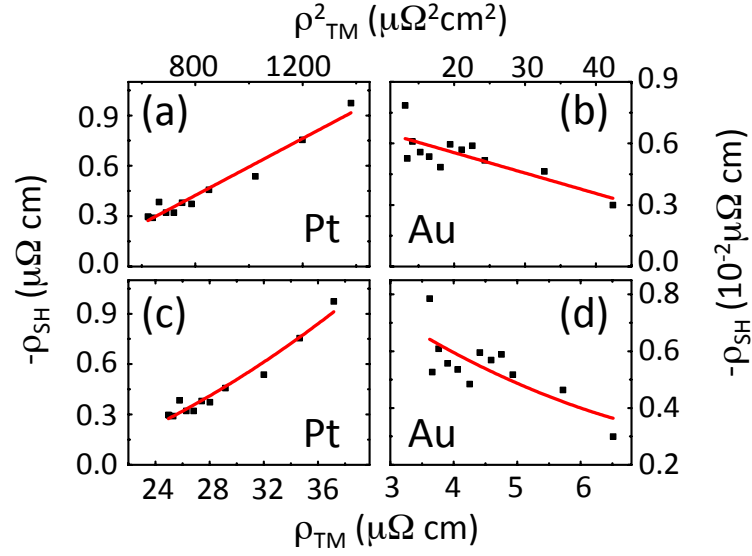


Figure 5.6: (a) Spin Hall resistivity as a function of the square of the total resistivity (a) for Pt and (b) for Au (black dots). The red solid line is a fit of the data to Eq.5.6, where the phonon skew scattering contribution is neglected. Spin Hall resistivity as a function of the total resistivity for (c) Pt and (d) Au (black dots). The red solid line is a fit of the data to Eq. 5.8, taking into account phonon skew scattering contribution.

As can be seen from Table 5.2, the intrinsic contribution of σ_{SH} in Pt dominates over the extrinsic one, as expected both from theoretical [24,30] and other experimental work [4], with a magnitude in close agreement with tight-binding calculations ($830 \mu\Omega^{-1} \text{ cm}^{-1}$) from Ref. [24]. On the other hand, the extrinsic contribution of σ_{SH} in Au dominates over the intrinsic one, which is consistent with previous theoretical work [31]. However, we obtain the opposite sign of σ_{SH}^{int} for the case of Au compared to Pt, in disagreement with first-principles calculations [30,32,33]. Furthermore, both transition metals have more than half-filled d bands, pointing to a positive intrinsic spin Hall conductivity as discussed previously [34] (see also Fig. 1.4). The origin of this unexpected sign is that the temperature dependence that enters in Eq. 5.5 through ρ_M is thus not enough to account for the strong temperature decay in σ_{SH} for Au (Fig. 5.4(d)). A possible explanation could be that neglecting the phonon contribution to

skew scattering is not a valid simplification. We can thus reintroduce this term, so that Eq. 5.6 is now:

$$-\rho_{SH} = \sigma_{SH}^{int} \rho_M^2 - \rho_{SH}^{phon} - \rho_{SH}^{imp}. \quad (5.7)$$

Assuming that skew scattering at phonons ($\rho_{SH}^{phon} \propto \rho_M^{phon}$) has the same scaling as the skew scattering at impurities ($\rho_{SH}^{imp} \propto \rho_M^{imp}$), we can rewrite Eq. 5.7 as:

$$-\rho_{SH} = \sigma_{SH}^{int} \rho_M^2 + \theta_{SH}^{phon} (\rho_M - \rho_M^{imp}) + \sigma_{SH}^{imp} (\rho_M^{imp})^2, \quad (5.8)$$

where θ_{SH}^{phon} is the phonon contribution to the spin Hall angle, which is temperature independent. By fitting our experimental data to Eq. 5.8 and fixing the intrinsic spin Hall conductivities from values obtained by tight-binding calculations [24], see Figs. 5.6(c) and 5.6(d), we obtain the values reported in Table 5.2. For Au we find a nonzero θ_{SH}^{phon} value, suggesting that phonon skew scattering might be an important contribution that has to be taken into account. However, a phonon contribution has not been identified up to now, either by studying the SHE in Pt [4], or in analyzing the AHE in Fe [29]. Indeed, the θ_{SH}^{phon} obtained for Pt is compatible with the value obtained for Au, although its contribution is irrelevant and hardly changes the weight of the other contributions (see Table 5.2). This observation evidences that the phonon term is not detectable experimentally in Pt. However, for the case of Au, it is clear that adding the phonon contribution involves a substantial change in the rest of the parameters (see Table 5.2). One reason to observe it so unambiguously in Au is the low resistivity of this metal. From Eq. 5.8, it can be clearly seen that the different contributions scale differently with the resistivity. The intrinsic term scales with $\propto \rho_M^2$, so that, in metals with large resistivity, this term will dominate over the rest. The phonon contribution term scales with $\propto (\rho_M - \rho_M^{imp})$, which means that, for small residual resistivities ρ_{TM}^{imp} like in the case of Au, this second term is comparable or higher than the intrinsic term and, therefore, it cannot be disregarded. Finally, the impurity contribution scales with $\propto (\rho_M^{imp})^2$, dominating over the phonon term in metals with higher residual resistivity.

Table 5.2: Summary of the fitting parameters obtained from data plotted in Fig 5.6.

		$\sigma_{SH}^{int} (\Omega^{-1} \text{ cm}^{-1})$	$\sigma_{SH}^{imp} (\Omega^{-1} \text{ cm}^{-1})$	$\theta_{SH}^{phon} (\%)$
Without phonon	Pt	847 ± 53	-406 ± 73	-
	Au	-100 ± 26	575 ± 45	-
With phonon	Pt	830	-388 ± 27	-0.06 ± 0.33
	Au	106	384 ± 25	-0.20 ± 0.03

5.4 Conclusions

We have shown that, by using SA device,s we are able to determine the particularly short spin diffusion length of metals with strong SOC, impossible to extract using conventional LSVs. We have also found that a proper definition of the spin resistance in Au is crucial to obtain an accurate spin diffusion length value. Additionally, using the same device, we have obtained the spin Hall angle for Au and Pt. We find systematically smaller spin Hall angles in comparison to those estimated by the spin pumping and spin-torque ferromagnetic resonance techniques. Although this underestimation might be corrected taking into account SML, we believe that its quantification is not trivial for our interfaces.

Moreover, we measured the temperature dependence of the SHE in Pt and Au to study the different contributing mechanisms. Whereas the intrinsic mechanism is the dominant contribution in Pt, for the case of Au extrinsic mechanisms play an important role. In particular, we have reported experimental evidence of a strong decay in the spin Hall angle for Au, which cannot be explained unambiguously by the intrinsic and impurity contributions. Therefore, we show that the phonon skew scattering contribution has to be taken into account as a source for the SHE, especially in materials, such as Au, where the residual resistivity is low. Additional work would be needed to better quantify the phonon-induced skew scattering in Au by systematically varying the residual resistivity.

References

- [1] E. Saitoh, M. Ueda, H. Mikajima, and G. Tatara, *Appl. Phys. Lett.* **88**, 182509 (2006).
- [2] T. Kimura, Y. Otani, T. Sato, S. Takahashi, and S. Maekawa, *Phys. Rev. Lett.* **98**, 156601 (2007).
- [3] L. Vila, T. Kimura, and Y. Otani, *Phys. Rev. Lett.* **99**, 226604 (2007).
- [4] M. Morota, Y. Niimi, K. Ohnishi, D. H. Wei, T. Tanaka, H. Kontani, T. Kimura, and Y. Otani, *Phys. Rev. B* **83**, 174405 (2011).
- [5] L. Liu, R. A. Buhrman, and D. C. Ralph, *arXiv:1111.3702*.
- [6] G. Mihajlovic, J. E. Pearson, M. A. Garcia, S. D. Bader, and A. Hoffmann, *Phys. Rev. Lett.* **103**, 166601 (2009).
- [7] V. Vlaminck, J. E. Pearson, S. D. Bader, and A. Hoffmann, *Phys. Rev. B* **88**, 064414 (2013).
- [8] Y. Niimi, H. Suzuki, Y. Kawanishi, Y. Omori, T. Valet, A. Fert, and Y. Otani, *Phys. Rev. B* **89**, 054401 (2014).
- [9] M. Obstbaum, M. Härtinger, H. G. Bauer, T. Meier, F. Swientek, C. H. Back, and G. Woltersdorf, *Phys. Rev. B* **89**, 060407(R) (2014).
- [10] T. Seki, Y. Hasegawa, S. Mitani, S. Takahashi, H. Imamura, S. Maekawa, J. Nitta, and K. Takanashi, *Nature Mater.* **7**, 125 (2008).
- [11] Y. Ji, A. Hoffmann, J. S. Jiang, and S. D. Bader, *Appl. Phys. Lett.* **85**, 6218 (2004).
- [12] J. Ku, J. Chang, S. Han, J. Ha, and J. Eom, *J. Appl. Phys.* **99**, 08H705 (2006).

- [13] P. Laczkowski, L. Vila, V.-D. Nguyen, A. Marty, J.-P. Attané, H. Jaffrès, J.-M. George, and A. Fert, *Phys. Rev. B* **85**, 220404(R) (2012).
- [14] E. Villamor, M. Isasa, L. E. Hueso, and F. Casanova, *Phys. Rev. B* **87**, 094417 (2013).
- [15] E. Villamor, M. Isasa, L. E. Hueso, and F. Casanova, *Phys. Rev. B* **88**, 184411 (2013).
- [16] W. Zhang, V. Vlaminck, J. E. Pearson, R. Divan, S. D. Bader, and A. Hoffmann, *Appl. Phys. Lett.* **103**, 242414 (2013).
- [17] A. Azevedo, L. H. Vilela-Leao, R. L. Rodríguez-Suárez, A. F. Lacerda Santos, and S. M. Rezende, *Phys. Rev. B* **83**, 144402 (2011).
- [18] J.-C. Rojas-Sánchez, N. Reyren, P. Laczkowski, W. Savero, J.-P. Attané, C. Deranlot, M. Jamet, J.-M. George, L. Vila, and H. Jaffrès, *Phys. Rev. Lett.* **112**, 106602 (2014).
- [19] T. Kimura, J. Hamrle and Y. Otani, *Phys. Rev. B* **72**, 014461 (2005).
- [20] R. J. Pedersen and F. L. Vernon, *Appl. Phys. Lett.* **10**, 29 (1976).
- [21] J. M. Pomeroy and H. Grube, *J. Appl. Phys.* **105**, 094503 (2009).
- [22] J. Bass and W. P. Pratt, *J. Phys.: Condens. Matter* **19**, 183201 (2007).
- [23] A. Hoffmann, *IEEE Trans. Magn.* **49**, 5172 (2013).
- [24] T. Tanaka, H. Kontani, M. Naito, D. S. Hirashima, K. Yamada, and J. Inoue, *Phys. Rev. B* **77**, 165117 (2008).
- [25] A. Fert and P. M. Levy, *Phys. Rev. Lett.* **106**, 157208 (2011).
- [26] S. Lowitzer, M. Gradhand, D. Kodderitzsch, D. Fedorov, I. Mertig, and F. Ebert, *Phys. Rev. Lett.* **106**, 056601 (2011).
- [27] S. Onoda, N. Sugimoto, and N. Nagaosa, *Phys. Rev. Lett.* **97**, 126602 (2006).
- [28] N. A. Sinitsyn, *J. Phys.: Condens. Matter* **20**, 023201 (2008).
- [29] Y. Tian, L. Ye, and X. Jin, *Phys. Rev. Lett.* **103**, 087206 (2009).
- [30] G. Y. Guo, *J. Appl. Phys.* **105**, 07C701 (2009).

- [31] M. Gradhand, D. V. Fedorov, P. Zahn, I. Mertig, Y. Niimi, Y. Otani, L. Vila, and A. Fert, *Spin* **2**, 1250010 (2012).
- [32] M. Gradhand, D. V. Fedorov, F. Pientka, P. Zahn, I. Mertig, and B. L. Györfy, *Phys. Rev. B* **84**, 075113 (2011).
- [33] G. Y. Guo, S. Murakami, T.-W. Chen, and N. Nagaosa, *Phys. Rev. Lett.* **100**, 096401 (2008).
- [34] H. Kontani, T. Tanaka, D. S. Hirashima, K. Yamada, and J. Inoue, *Phys. Rev. Lett.* **102**, 016601 (2009).

Chapter 6

Inverse Rashba-Edelstein effect in Bi

Another very promising way to convert spin current into charge current is by exploiting the inverse Rashba-Edelstein effect (IREE) as explained in Section 1.2.2. This phenomenon arises from the spin-orbit splitting in a two-dimensional electron gas (2DEG) known as the Rashba effect, leading to the conversion of a 3D spin current into a 2D charge current [1]. There are many systems where the surface state is strongly spin-orbit split, including metals (a typical example is Au(111) [2]) and semiconductors with giant spin-orbit coupling (SOC), such as BiTeI and BiTeCl [3, 4], although in these cases the bulk states usually dominate the conduction. An optimal choice seems to be a semimetallic system such as bismuth (Bi).

Bi is a group V semimetal with an anisotropic Fermi surface, where small electron and hole pockets give rise to a low carrier density, $n \sim p \sim 3 \times 10^{17} \text{ cm}^{-3}$, high resistivity ($\sim 100 \mu\Omega \text{ cm}$) and relatively large Fermi wavelength ($\sim 30 \text{ nm}$) [2]. For thin films, the energy band structure changes. When film dimensions are comparable to the Fermi wavelength, a semimetal-to-semiconductor transition is predicted [3]. At the same time, metallic surface states are found to gain relevance in transport, leading to a 2D confinement of the carriers as recently observed experimentally [2]. The strong SOC in Bi and the loss of time-reversal symmetry at the surface produces Rashba splitting on the surface states [4]. For this reason, not only the SOC on the Bi surface has attracted a great deal of attention [5], but also surface alloying of Bi with other materials has been studied. The largest spin-splitting has been found for a silver (Ag)/Bi interface [6],

however other systems such as copper (Cu)/Bi are also expected to manifest a sizeable effect [7].

In this chapter, we will use the spin absorption (SA) method (as in Chapter 5) to demonstrate first that all the spin current that reaches the Bi wire is absorbed at the surface, without diffusing into the bulk. Then, using the same devices, we will show how this 3D spin current is converted into a 2D charge current due to IREE and we quantify it with the IREE length (λ_{IREE}). This λ_{IREE} undergoes a puzzling sign change when we study it as a function of temperature. In order to understand this intriguing behavior, we provide a theoretical analysis that explains the sign change in terms of the complex spin structure and dispersion of the surface states of Bi at the Fermi level.

6.1 Fabrication

The fabrication procedure is the same as the one described in the previous chapter (Section 5.1). In the first lithography step, the FM electrodes are patterned with different widths (~ 100 nm and ~ 150 nm) and a separation between the electrodes of $L \sim 630$ nm. 35-nm-thick Py is deposited by e-beam evaporation at a pressure of $\leq 1 \times 10^{-8}$ mbar. In the second lithography step, the ~ 150 -nm-wide middle wire is patterned and 20-nm-thick Bi is deposited by e-beam evaporation at a pressure of $\sim 1 \times 10^{-7}$ mbar. Since our Bi films grow on top of SiO₂, they are predominantly textured along the (111) direction [8]. In the last step, the ~ 150 -nm-wide channel is patterned and 100-nm-thick Cu is thermally evaporated ($\leq 1 \times 10^{-8}$ mbar). Before the Cu deposition, the Py and Bi surfaces are cleaned with an Ar-ion milling to remove the possible resist left overs or oxide formation.

A more detailed description of the fabrication parameters is given in Appendix B.

6.2 Spin absorption at the interface

First, the Bi wire is electrically characterized, where the resistivity is measured using a 4-probe configuration, as shown in Fig. 6.1(a). From these measurements as a function of temperature (Fig. 6.1(b)), a resistivity of $\rho_{Bi}=988 \mu\Omega \text{ cm}$ ($\rho_{Bi}=830 \mu\Omega \text{ cm}$) is

obtained at 10 K (300 K). Afterwards, we performed non-local measurements (Fig. 6.1(c)), where, despite the high resistivity of the Bi wire, a clear spin absorption can be observed. The temperature dependence of the spin absorption ratio η is plotted in Fig. 6.1(d). At low temperature, we obtain $\eta=0.14$, which together with the measured ρ_{Bi} at 10 K, yields $\lambda_{Bi}=0.05$ nm. However, this value is far from $\lambda_{Bi}=20$ nm obtained by weak antilocalization (WAL) measurements in Bi evaporated under the same conditions [9]. The same occurs at room temperature, where from the measured values of $\eta=0.11$ and ρ_{Bi} we extract a spin diffusion length of $\lambda_{Bi}=0.11$ nm. This value is again far from room temperature λ_{Bi} values reported in literature using the spin-pumping technique, which range from 8 to 50 nm [10–12]. We must stress here that WAL and spin-pumping experiments probe the bulk λ_{Bi} value. However, both the room- and low-temperature λ_{Bi} values that we extract from SA measurements are anomalously small, as they are shorter than the interatomic distance of Bi [13], evidencing that the spin current is strongly absorbed at the metallic surface rather than in the bulk, in good agreement with the unique surface properties of Bi [2].

6.3 Inverse Rashba-Edelstein effect

6.3.1 Experimental characterization

After proving that the Bi surface acts as a strong spin absorber, we will analyze the way in which the absorbed spin current is converted into a charge current. This conversion will be given by λ_{IREE} which is defined in Eq. 2.25. Since all the transport in Bi occurs at the surface, the sheet resistance, R_{sheet} , of Eq. 2.25 can be calculated as the measured resistivity divided by the Bi thickness, $R_{sheet} = \rho_{Bi}/t_{Bi}$. Thus, for the case of Bi, λ_{IREE} is defined as:

$$\lambda_{IREE} = \frac{w_{Bi} t_{Bi}}{x_{Bi} \rho_{Bi}} \frac{I_c}{I_s(z=0)} \Delta R_{SCC} \quad (6.1)$$

where all the geometrical parameters can be measured by SEM, x_{Bi} is the shunting coefficient and ΔR_{SCC} is measured as shown in Fig. 6.2(a).

As can be seen from Eq. 6.1, the shunting coefficient is crucial for a proper evaluation of the spin-to-charge conversion. Therefore, in order to obtain an accurate

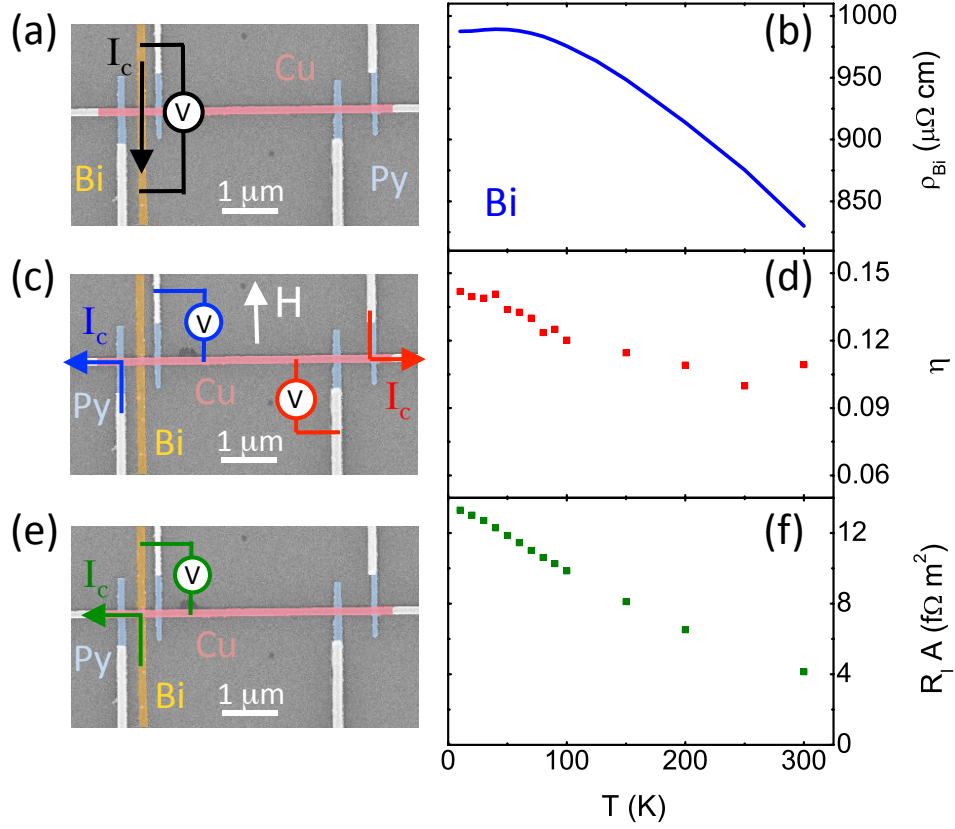


Figure 6.1: (a) Colored SEM image of two Py/Cu LSVs, the left one with a Bi wire in between the Py electrodes and the right one without. The measurement configuration to measure the Bi resistivity and the different materials (Py, Bi and Cu) are shown. (b) Resistivity of the Bi wire as a function of temperature. (c) SEM image of the device, where the non-local measurement configuration and the applied magnetic field, H , are shown. (d) Spin absorption parameter, $\eta = \frac{\Delta R_{NL}^{abs}}{\Delta R_{NL}^{ref}}$ as a function of temperature. (e) SEM image of the device where the cross configuration for measuring the Cu/Bi interface resistance is shown. (f) Measured interface resistance area product as a function of temperature.

value, we have used a software based on finite elements (SpinFlow 3D). For this purpose, we have to determine the resistivity of the metals forming the interface (ρ_{Cu} and ρ_{Bi}), its area (A) and the resistance of the interface, R_I . The Cu/Bi interface resistance was measured using a cross configuration (Figs. 6.1(e) and 6.1(f)). We obtain a shunting coefficient of $x_{Bi} = 0.1012$ (0.0856) at 10 K (300 K).

The λ_{IREE} value that we deduce from our measurements (Fig. 6.2(b)) is $\lambda_{IREE} = 0.009$ nm (-0.001 nm) at 300 K (10 K), which is smaller than $\lambda_{IREE} = 0.3$ nm reported for Ag/Bi at 300 K by spin-pumping experiments [14]. Since the injection process might be substantially less efficient for electrical spin injection than for spin-pumping experiments

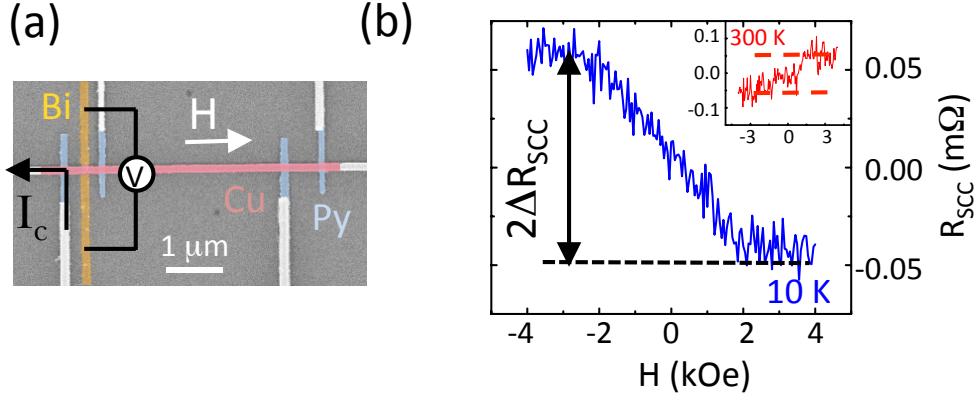


Figure 6.2: (a) Colored SEM image of a typical device to measure the spin-to-charge conversion. The materials (Py, Cu and Bi), the direction of H and the measurement configuration are shown. (b) Non-local resistance R_{SCC} for Bi detected when measuring in the spin-to-charge conversion configuration as a function of H at 10 K (blue curve). Inset: R_{SCC} as a function of H at 300 K (red curve), where the dashed lines are a guide to the eye. The spin-to-charge conversion signal is tagged as ΔR_{SCC} . A current of $I_c = 1 \text{ mA}$ is injected.

[15], our effective λ_{IREE} value is a lower limit. A theoretical estimation of λ_{IREE} from the expression $\lambda_{IREE} = \frac{\alpha_R \tau}{\hbar}$ [1, 14], where τ is the momentum relaxation time as discussed by Shen et al. [1] and α_R is the Rashba coefficient, is not trivial. On the one hand, τ should be the momentum relaxation time of the metallic surface of Bi, which is not straightforward to determine from experiments, as usually bulk τ is measured. On the other hand, for the complex non-monotonic dispersion of the Bi(111) surface states (Fig. 6.4(a)) the parameter α_R does not have an obvious physical meaning, and it is not clear which value should be ascribed to it in the present experiment.

The most puzzling point in these results is the sign cross over that we observe for λ_{IREE} at $\sim 125 \text{ K}$ (Fig. 6.3(a)). This implies that opposite charge currents are created with the same spin current direction at low and high temperatures. In the next section, we provide a theoretical analysis, based on the first principles band structure, that can account for this sign change.

6.3.2 Theoretical analysis

In order to understand this behaviour, a careful microscopic analysis of the spin-resolved surface electronic structure is needed. Let us consider the nonequilibrium distribution of carriers in Bi produced by the injection of a pure spin current. The nonequilibrium carriers are restricted to a close vicinity of the Fermi energy, and the probability of

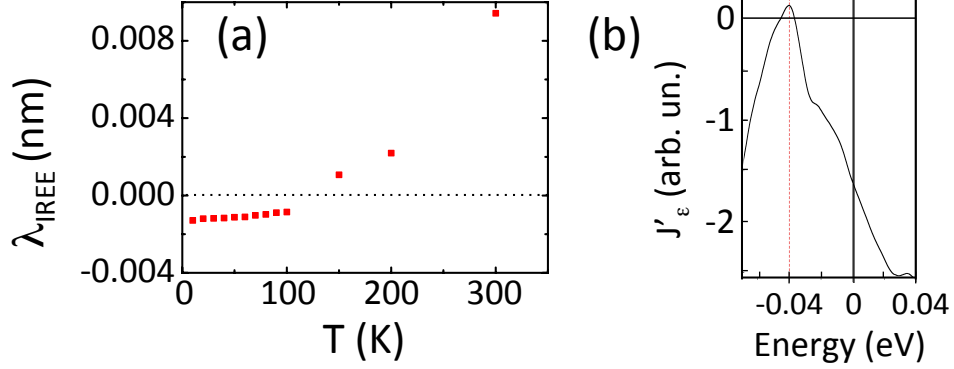


Figure 6.3: (a) Temperature evolution of the IREE length of Bi as obtained from a SA device. (b) Energy dependence of the spectral current density $j'_E(E)$ calculated by using $s_\lambda(k_\parallel)$ for $n_\lambda(k_\parallel)$.

an electron state to host the injected electron depends on its probability to have the respective spin, \uparrow or \downarrow , in the vicinity of the surface (by controlling the overlap between the wave function of the injected electron and the current carrying state).

Let the in-plane spin quantization axis be perpendicular to the induced current direction and consider the difference between the current due to spin- \uparrow and spin- \downarrow electrons. In a semi-infinite crystal the eigenstates are labeled by the Bloch vector parallel to the surface k_\parallel , the energy E , and the band number λ . In a slab calculation, the energy continuum at each k_\parallel is approximated by a discrete set of levels. Each eigenstate is ascribed a spin value $s_\lambda(k_\parallel)$, which is defined as an integral over a surface region from depth z_0 to vacuum z_V :

$$s_\lambda(k_\parallel) = \int_{z_0}^{z_V} \rho_\lambda^\uparrow(k_\parallel, z) - \rho_\lambda^\downarrow(k_\parallel, z) dz \quad (6.2)$$

The spin spectral density for k_\parallel along $\overline{\Gamma M}$ and the spin quantization axis perpendicular to k_\parallel is shown in Fig. 6.4(a) (the integration in Eq. 6.2 is over the outermost bilayer). The electric current density j is then a sum of the partial currents over all states outside the equilibrium distribution. The contribution of a narrow energy interval δE around energy E to the nonequilibrium current is $\delta j = j'_E(E)\delta E$, with the current spectral density given by the integral over a constant energy contour:

$$j'_E(E) = \sum_{\lambda} \int_{FS} d\tau \frac{n_{\lambda}(k_{\parallel}^{\lambda}) v_{\lambda}(k_{\parallel}^{\lambda})}{|\nabla_{k_{\parallel}} \epsilon_{\lambda}(k_{\parallel}^{\lambda})|} \quad (6.3)$$

where $v_{\lambda}(k_{\parallel})$ is the group velocity, and $n_{\lambda}(k_{\parallel})$ is the deviation of the occupation number from its equilibrium value. At elevated temperatures the Fermi distribution smears out, and the states below E_F become available to the injected electrons, which changes the balance of different contributions to the integral, and, thus, may change the sign of the effect [Fig. 6.3(b)].

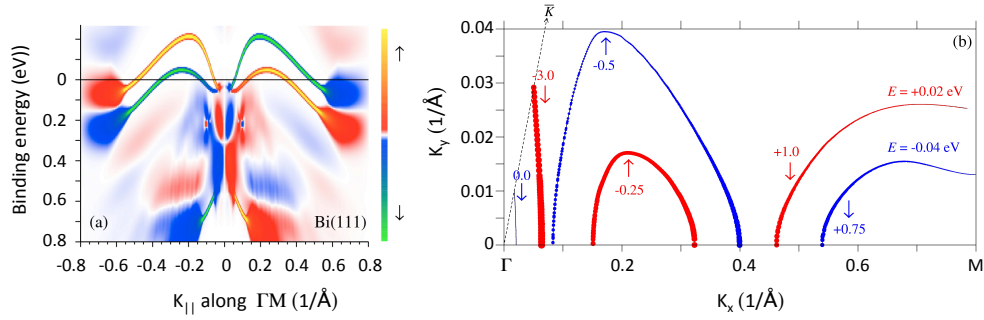


Figure 6.4: (a) k_{\parallel} projected spin spectral density for k_{\parallel} along ΓM . The calculation is performed for a slab of 16 Bi bilayers with the full-potential linear augmented plane wave method [16]. Surface states are shown by distinct thick lines, and the bulk states are presented by smearing the slab levels with a Gaussian of 0.15 eV FWHM. (b) Constant energy contours in the 30° sector of the 2D Brillouin zone for $E = 0.02$ eV (green lines) and $E = 0.04$ eV (black lines) relative to the Fermi energy. The sign of the spin projection $s_{\lambda}(k_{\parallel})$ of the contour is indicated by \uparrow or \downarrow , and the line thickness is proportional to the absolute value of the spin projection. The value at the \uparrow or \downarrow symbol (in arbitrary units) indicates the contribution of that branch of the contour to j'_E .

Let us consider current along the Bi(111) surface in the $\overline{\Gamma M}$ direction. Because the coefficients $n_{\lambda}(k_{\parallel})$ are not known (they depend on specific features of the injection process), for a qualitative discussion let us assume $n_{\lambda}(k_{\parallel})$ to be proportional to the spin at the surface $s_{\lambda}(k_{\parallel})$, see Eq. 6.2. Two constant energy contours for two energies close to E_F are shown in Fig. 6.4(b). Although the bulk states at the Fermi level are spin polarized at the surface, see Fig. 6.4(a), the main contribution to the inverse Rashba-Edelstein effect turns out to come from the surface states. Within the same surface state band the net spin projection does not change sign, but the direction of the group velocity changes. As a result, the contributions from different k_{\parallel} regions have different sign, and their relative weights vary with energy. The function $j'_E(E)$ calculated for a 16-bilayer Bi(111) slab is shown in Fig. 6.3(b). The $j'_E(E)$ curve turns out to be

non-monotonic, and it changes sign at 0.04 eV below the Fermi energy.

This offers the following hypothetical scenario of the sign change in the IREE effect with increasing the temperature: suppose that in the actual case the current spectral density changes sign just below the Fermi level. As the equilibrium occupation of the states below E_F decreases, they become selectively (depending on the spin) occupied by the injected electrons and may produce a current in the opposite direction. This may not happen for surface states of the Rashba model because of their monotonic dispersion (unless $n_\lambda(k_\parallel)$ show sharp variations), but this may happen for the more complicated surface states of Bi(111). The present calculation suggests a minor role of the bulk states in IREE, which stems from their low density at E_F (semimetallic character of Bi). Moreover, both the polarization and the group velocity have the same sign for the bulk hole pocket at Γ and electron pocket at M , so a change of their occupation numbers does not explain the inversion of the induced current. In spite of the limitations of the present analysis (that arise from our lack of knowledge of the actual structure of the Cu/Bi interface and its k_\parallel - and spin-resolved transport properties), it suggests a microscopic mechanism of converting spin current into charge current via surface states, which possesses the property of changing the sign depending on occupation numbers.

6.4 Is it possible to have inverse spin Hall effect?

Despite the strong experimental and theoretical evidence supporting IREE as the spin-to-charge current conversion mechanism, one could still argue that the ISHE, and not the IREE, is the responsible mechanism for the conversion. This would be the case if the spin current diffusing along the Cu channel were absorbed by the bulk Bi, instead of the interface. In such scenario, however, the spin diffusion length obtained from the SA experiment should be much longer, similar to the lengths obtained from WAL [9] or spin pumping [14–16] measurements (which we assume here to be the bulk value, λ_{Bi}). Since this is not the case, the observed discrepancy could only be compatible with spin absorption in the bulk Bi by assuming a large spin-flip scattering at the interface, leading to spin memory loss (SML), as explained in Section 5.3.1.

The main difference compared to Cu/Pt and Au/Pt interfaces (Chapter 5.3.1), is that for Cu/Bi interface the only unknown parameter in Eq. 5.1 is δ . Note that in this case we know R_{series} because we have measured it in SA experiments, we know R_M (with $M = Bi$) because it is the value that we obtain using the real spin diffusion

length from WAL measurements and we also know R_I , which in this case is $R_I > 0$ and we measured it as shown in Figs. 6.1(e) and 6.1(f). From Eq. 5.1 we can obtain the only unknown parameter, $\delta = 26.95$ (4.54) at 10 K (300 K).

Once we know δ , we can calculate the SML parameter, which is given by Eq. 5.2, and we obtain $r_{SML} = 7.63 \times 10^{-15}$ (2.87×10^{-4}) at 10 K (300 K). If we take into account the SML ratio and we introduce it to calculate the spin Hall angle (Eq. 5.3), we obtain $\theta_{SH,Bi} = 3.6 \times 10^{13}$ % (2470 %) at 10 K (300 K). As $\theta_{SH,Bi}$ values are over 100 %, which is an unphysical value, we can rule out the possibility of ISHE as the spin-to-charge current conversion mechanism in our system.

6.5 Conclusions

In summary, we demonstrate that the Bi metallic surface acts as a strong spin absorber. We show that a conversion of 3D spin currents to 2D charge currents occurs at such metallic surface by means of the inverse Rashba-Edelstein effect. Moreover, the temperature dependence of the IREE features a sign crossover at ~ 125 K, which according to our theoretical analysis, arises from a spin structure with non-monotonic dispersion of the surface states at the Fermi level. This rich phenomenology of the complex electronic behavior of Bi could be further exploited to unveil yet unpredicted spin-dependent effects.

References

- [1] K. Shen, G. Vignale and R. Raimondi, *Phys. Rev. Lett.* **112**, 096601 (2014).
- [2] S. Xiao, D. Wei and X. Jin, *Phys. Rev. Lett.* **109**, 166805 (2012).
- [3] V. N. Lutskii, *JETP Lett.* **2**, 245 (1965).
- [4] J. I. Pascual, G. Bihlmayer, Y. M. Koroteev, H. P. Rust, G. Ceballos, M. Hansmann, K. Horn, E. V. Chulkov, S. Blügel, P. M. Echenique and Ph. Hofmann, *Phys. Rev. Lett.* **93**, 196802 (2004).
- [5] Y. M. Koroteev, G. Bihlmayer, J. E. Gayone, E. V. Chulkov, S. Blügel, P. M. Echenique and Ph. Hofmann, *Phys. Rev. Lett.* **93**, 046403 (2004).
- [6] C. R. Ast, J. Henk, A. Ernst, L. Moreschini, M. C. Falub, D. Pacilé, P. Bruno, K. Kern and M. Grioni, *Phys. Rev. Lett.* **98**, 186807 (2007).
- [7] H. Bentmann, F. Forster, G. Bihlmayer, E. V. Chulkov, L. Moreschini, M. Grioni and F. Reinert, *Europhys. Lett.* **87**, 37003 (2009).
- [8] N. Marcano, S. Sangiao, C. Magen, L. Morellón, M. R. Ibarra, M. Plaza, L. Perez and J. M. de Teresa, *Phys. Rev. B* **82**, 125326 (2010).
- [9] S. Sangiao, N. Marcano, J. Fan, L. Morellón, M. R. Ibarra, J. M. De Teresa, *Europhys. Lett.* **95**, 37002 (2011).
- [10] S. Sangiao, J. M. De Teresa, L. Morellón, I. Lucas, M. C. Martinez-Velarte, and M. Viret, *Appl. Phys. Lett* **106**, 172403 (2015).
- [11] H. Emoto, Y. Ando, E. Shikoh, Y. Fuseya, T. Shinjo and M. Shiraishi, *J. Appl. Phys.* **115**, 17C507 (2014).

- [12] D. Hou, Z. Qiu, K. Harii, Y. Kajiwara, K. Uchida, Y. Fujikawa, H. Nakayama, T. Yoshino, T. An, K. Ando, X. Jin and E. Saitoh, *Appl. Phys. Lett.* **101**, 042403 (2012).
- [13] P. Cucka and C. S. Barrett, *Acta Crystall.* **15**, 865 (1962).
- [14] J. C. Rojas-Sánchez, L. Vila, G. Desfonds, S. Gambarelli, J. P. Attané, J. M. De Teresa, C. Magén and A. Fert, *Nature Comms.* **4**, 2944 (2013).
- [15] K. Ando, S. Takahashi, J. Ieda, H. Kurebayashi, T. Tryponiotis, C. H. W. Barnes, S. Maekawa and E. Saitoh, *Nature Mater.* **10**, 655 (2011).
- [16] E. E. Krasovskii, F. Starrost, and W. Schattke, *Phys. Rev. B* **59**, 10504 (1999).

Chapter 7

Spin Hall magnetoresistance

As explained in Chapter 1, spin Hall magnetoresistance (SMR) is an alternative way to evaluate the magnitude of the spin Hall effect (SHE) in a non-magnetic (NM) metal using a NM/ferromagnetic insulating (FMI) system. However, the rich phenomenology of the effect enables to determine not only the properties of the NM but also the features of the other elements forming the system: the NM/FMI interface and the FMI. The information one can obtain of the FMI/NM interface is given by the spin-mixing conductance, G_r , and it determines the efficiency of the spin injection [1–3]. This concept is not only at the base of the SMR, but also of other spin-dependent phenomena such as the spin Seebeck effect [4–7], the spin pumping [4, 8–10] or the magnetic gating of pure spin currents [11, 12]. Regarding the FMI, one can acquire details of its surface magnetization from SMR measurements, otherwise not possible with standard magnetometric techniques.

In this chapter, instead of studying the SHE from SMR measurements, we will focus on the other two features: the NM/FMI interface and the surface magnetization of the FMI. For this purpose we are going to use a system formed by Pt/CoFe₂O₄ (CFO). On one hand, we have chosen Pt as the NM because its spin Hall angle is one of the largest among metals with strong SOC (see Table 1.1). On the other hand, we select CFO, a room-temperature ferrimagnetic insulating oxide whose surface magnetization differs from that of the bulk due to its complex atomic constitution [13, 14]. The presence of Co²⁺ ions anticipates a large magnetic anisotropy in CFO [13] and the competing nature of magnetic interactions in spinels may lead to different magnetic properties [14] at the surface. Therefore, CFO is especially suitable to explore the role of the surface

magnetic textures by using SMR. First, we will show that the nature of the NM/FMI interface strongly affects the spin-mixing conductance. For this purpose, the interface quality will be tuned using two different strategies: (i) growing the Pt layer using an *in-situ* or an *ex-situ* process and (ii) growing the CFO with a different crystallographic orientation, which can be (001) or (111). Afterwards, by studying the field-dependent magnetoresistance arising from SMR, we will resolve the distinct surface magnetization behavior of the CFO films, compared to its bulk magnetization.

7.1 Fabrication

Two types of Pt/CFO samples have been fabricated, which can be classified according to the way in which Pt was deposited during the fabrication process: (i) *ex-situ* and (ii) *in-situ* samples. In both type of samples, the CFO deposition is the common and first step of the fabrication process. CFO films are epitaxially grown on SrTiO₃ (STO) substrates using a CFO stoichiometric target by pulsed laser deposition [15]. The thickness of the CFO films ranged from 40 nm to 67 nm (see Table 7.1), as inferred from growth rate calibration by X-ray reflectometry.

In the *ex-situ* samples, the Hall bars (width $W=100\ \mu\text{m}$ and length $L=800\ \mu\text{m}$), which are essential for transport measurements, are patterned using eBL with positive resist after the CFO deposition. Afterwards, 7-nm-thick Pt is deposited by dc sputtering at room temperature and this is followed by the lift-off process.

In the *in-situ* samples, the Pt deposition is carried out right after the CFO deposition, without breaking the vacuum, by dc sputtering at a temperature of 400°C. Afterwards, the Hall bars (with the same geometry as the one used in the *ex-situ* samples) are patterned by eBL using negative resist, followed by Ar-ion milling and lift-off. In this case, different samples with Pt thicknesses of 6.5 nm, 4 nm and 2 nm have been fabricated.

A total of five pairs of Pt/CFO samples were prepared by using two substrate orientations: STO(001) and STO(111), and three distinct processes denoted: EX-1, EX-2 and IN. A list of all the different samples can be seen in Table 7.1. In process EX-1, the CFO layers on (001) and (111) substrates were grown in different runs and the Pt layer was grown *ex situ*. In samples prepared by processes EX-2 and IN, the CFO layers were grown simultaneously on (001) and (111) substrates in each run, whereas

the Pt layer was grown either *ex situ* (EX-2) or *in situ* (IN).

More details on the fabrication parameters are given in Appendix C.

7.2 Electrical characterization

Magnetization and magnetotransport measurements were performed at temperatures ranging from 300 K to 40 K and applying external magnetic fields (H) up to ± 9 T. All the samples have been electrically characterized by angle-dependent magnetoresistance (ADMR) and field-dependent magnetoresistance (FDMR) measurements. Two different configurations, longitudinal and transverse (see sketches in Fig. 7.1), have been used for the transport measurements.

ADMR measurements were carried out fixing the magnetic field at 9 T and varying it along the different H -rotation planes. Their corresponding angles are defined as α , β and γ and are schematically shown in Fig. 7.1.

FDMR measurements were carried out sweeping the magnetic field from -9 T to 9 T, but fixed in a given direction, which can be: (i) along the current direction (\hat{j} direction), (ii) in-plane and transverse to the current (\hat{t} direction) and (iii) out-of-plane (\hat{n} direction). In this case, only the longitudinal configuration was measured.

Apart from the electrical measurements, the magnetization of the CFO films have been characterized using a vibrating sample magnetometer (VSM). In these measurements, the magnetic field was also applied along the different directions: \hat{j} , \hat{t} and \hat{n} .

As we will see, from ADMR measurements we can establish the value of G_r at the Pt/CFO interface, whereas the FDMR measurements, together with magnetization measurements, enable to determine the surface magnetization of CFO.

7.3 Occurrence of SMR

In Fig. 7.1, we show, as illustrative examples, the longitudinal and transverse ADMR measured for (001)EX-1(7) and (111)EX-2(7) samples.

Based on the SMR scenario, the longitudinal resistance R_L of Pt should only change when the direction of the magnetization, \vec{M} , changes with respect to the spin

polarization, \vec{s} , *i.e.*, when the field is rotated along α and β angles (Eq. 2.26). As shown in Figs. 7.1(b-c) and 7.1(f-g), the measured resistance follows $R_L(\alpha) \propto \cos^2(\alpha)$ and $R_L(\beta) \propto \cos^2(\beta)$, respectively. The magnetoresistance value should be similar in both cases, $\Delta R_L(\beta) = \Delta R_L(\alpha)$ and from this amplitude, using Eq. 2.28, we extract G_r . Additionally, $R_L(\gamma)$ should not vary when H is rotated along γ , as in this case \vec{M} is always perpendicular to \vec{s} . This is exactly the behavior observed in Fig. 7.1(a) and 7.1(e).

Moreover, the transverse measurements, shown in Figs. 7.1(d) and 7.1(h), display a $\cos(\alpha)\sin(\alpha)$ dependence, fully consistent with Eq. 2.27. In addition, the amplitude of transverse magnetoresistance, ΔR_T , is smaller than ΔR_L by ~ 10 , in agreement with the difference on the geometrical factor ($L/W \sim 8$).

Therefore, the observed ADMR response of the (001)EX-1(7) and (111)EX-2(7) samples (Fig. 7.1) indicates the presence of SMR in Pt/CFO samples. This SMR prevalence occurs for all measured samples, listed in Table 7.1.

7.4 Spin-mixing conductance

As discussed in section 2.2, the magnitude of SMR (Eq. 2.28) is defined by parameters of the Pt layer (ρ_{Pt} , t_{Pt} , $\theta_{SH,Pt}$ and λ_{Pt}) and the spin-mixing conductance, G_r , at the Pt/CFO interface. Therefore, if all the parameters that define the Pt layer are known, G_r can be easily extracted from the ADMR measurements.

Although the resistivity and thickness of the Pt layer are well known from the electrical characterization and X-ray reflectivity measurements, respectively, there is a big discrepancy in the literature for the values of $\theta_{SH,Pt}$ and λ_{Pt} [16]. In a first approximation we can use the values obtained in Chapter 5. As $\rho_{Pt} \sim 20\text{-}30 \mu\Omega\text{cm}$ for the samples listed in Table 7.1, we can consider $\lambda_{Pt} = 3.4 \text{ nm}$ and $\theta_{SH,Pt} = 1.5 \%$ which we have obtained before for $\rho_{Pt} = 25 \mu\Omega\text{cm}$ (see Table 5.1). The G_r values that we obtain with these λ_{Pt} and $\theta_{SH,Pt}$ are negative ($G_r < 0$) for all the samples listed in Table 7.1, and this is not a realistic value, as it measures the efficiency of the spin injection and thus, should be $G_r > 0$. As mentioned in Chapter 5, there is a big controversy with λ_N and θ_{SH} values obtained from spin pumping and spin absorption experiments. Therefore, as the unifying values seem to be those reported by Ref. [18], where they take into account SML, these will be the values that we choose to study SMR ($\theta_{SH,Pt} = 5.6 \%$ and $\lambda_{Pt} = 3.4$

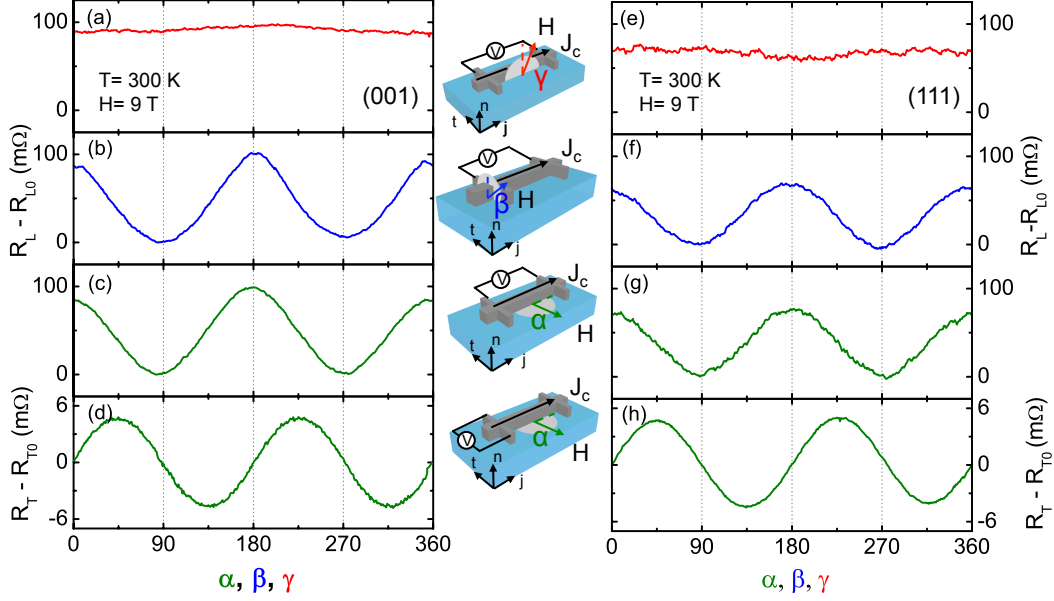


Figure 7.1: Angle-dependent magnetoresistance measurements at 9 T and 300 K for (001)EX-1(7) ((a)-(d)) and (111)EX-2(7) ((e)-(h)) samples. $R_{L,T}$ is the measured resistance and $R_{L0,T0}$ is the subtracted background. ((a)-(c)) and ((e)-(g)) Longitudinal resistance R_L as a function of the direction of the applied magnetic field, in three different rotation planes. ((d) and (h)) Transverse resistance, R_T , as a function of angle α . Central panel: sketches indicate the definition of the angles α, β and γ and the measurement configuration.

nm). Table 7.1 shows the spin Hall magnetoresistance values, at 9 T and 300 K, and the extracted G_r values for all our samples.

A general look at the values of the table reveals that, in general, the G_r values that we obtain are similar to those reported in literature for other NM/FMI systems: indeed, for Pt/YIG, it ranges from 1.2×10^{12} to $1.3 \times 10^{15} \Omega^{-1}m^{-2}$ [3, 4, 17, 19–25], $1.9 \times 10^{14} \Omega^{-1}m^{-2}$ for Au/YIG [2] or $2.6 \times 10^{14} \Omega^{-1}m^{-2}$ for Pt/Fe₃O₄ [26].

A more detailed inspection of data in Table 7.1 immediately reveals some remarkable trends: (i) although the CFO layers have been grown under nominally identical conditions in samples EX-2 and IN, the extracted spin-mixing conductance differs, being definitely larger for IN than for EX-2 samples and (ii) for all pair of 7-nm-thick Pt samples (IN, EX-2 and EX-1), G_r in (001) orientation ($G_r(001)$) is different and somewhat larger than the corresponding G_r in the (111) crystallographic orientation

Table 7.1: Summary of the relevant data corresponding to the five pairs of Pt/CFO samples used in this work: fabrication process, crystallographic orientation of the CFO film, thickness of CFO film (t_{CFO}), thickness of Pt film (t_{Pt}), resistivity of the Pt film (ρ_N), SMR effect ($\Delta\rho_1/\rho_N=\Delta R_L/R_{L0}$) and the real part of the spin-mixing conductance (G_r) calculated from Eq. 2.28 by using $\theta_{SH,Pt}=5.6\%$ and $\lambda_{Pt}=3.4$ nm.

Sample	Fabrication	Orientation	$t_{CFO}(nm)$	$t_{Pt}(nm)$	$\rho_N(\mu\Omega)cm$	$\Delta R_L/R_{L0}$	$G_r (\Omega^{-1}m^{-2})$
(001)EX-1(7)	EX-1	(001)	67	7	29.6	2.7×10^{-4}	2.4×10^{14}
(111)EX-1(7)	EX-1	(111)	56	7	19.5	0.2×10^{-4}	1.4×10^{13}
(001)EX-2(7)	EX-2	(001)	57	7	29.7	1.2×10^{-4}	7.4×10^{13}
(111)EX-2(7)	EX-2	(111)	57	7	66.8	0.9×10^{-4}	2.4×10^{13}
(001)IN(7)	IN	(001)	40	6.5	21.4	2.5×10^{-4}	2.4×10^{14}
(111)IN(7)	IN	(111)	40	6.5	18.2	1.8×10^{-4}	1.9×10^{14}
(001)IN(4)	IN	(001)	40	4	20.2	3.4×10^{-4}	2.6×10^{14}
(111)IN(4)	IN	(111)	40	4	23.3	2.5×10^{-4}	1.4×10^{14}
(001)IN(2)	IN	(001)	40	2	36.0	6.0×10^{-4}	2.4×10^{14}
(111)IN(2)	IN	(111)	40	2	34.5	4.3×10^{-4}	1.1×10^{14}

($G_r(111)$).

Therefore, we will analyze in more detail the role of the Pt growth (*ex situ* vs *in situ*) as well as the importance of the crystallographic orientation ((001) vs (111)).

7.4.1 *Ex situ* vs *in situ*

It is well known that G_r is very sensitive to the details of the interface between the FMI and the NM [2,3,20,24,27]. As the Pt layer is deposited differently in *ex-situ* and *in-situ* samples, the morphology, roughness and defects of the Pt film can be different for both deposition methods. Moreover, the interface is likely modified during the *ex-situ* Pt deposition, because it involves exposure of the free surface of the CFO to air and to the chemicals used for the lithography process. Consequently, if we look at the results that we get for the IN and EX-2 samples, it is not surprising to find a larger G_r value for IN samples and therefore $G_r(001)$ and $G_r(111)$ values for IN samples set upper bounds to the spin-mixing conductances of (001) and (111) interfaces in Pt/CFO.

7.4.2 (001) vs (111)

Another important conclusion that we can extract from Table 7.1 is that every pair of samples systematically shows $G_r(001) > G_r(111)$ which suggests that the spin-mixing conductance may depend on the interface orientation of the ferromagnetic insulator.

However, a quantitative comparison between crystallographic orientations can be

best done for IN samples due to the optimal interface preparation conditions. For this reason, we will now focus on the samples prepared with the same IN process and different Pt thicknesses: (001)IN(2,4,7) and (111)IN(2,4,7). We show in Fig. 7.2 the dependence of the magnetoresistance, at 9 T and 300 K, of the three pairs of IN samples when rotating the magnetic field in a plane perpendicular to the current (*i.e.*, as a function of β). In this geometry, the amplitude of the observed magnetoresistance ($\Delta\rho_1/\rho_N = \Delta R_L/R_{L0}$) is linked to G_r (Eq. 2.28) and it thus allows us a simple visualization of the changes of G_r and its evaluation. It can be appreciated in Table 7.1 that the extracted G_r values for these samples are radically different for both terminations ($G_r(001) = 2.5(1) \times 10^{14} \Omega^{-1}\text{m}^{-2}$ and $G_r(111) = 1.5(4) \times 10^{14} \Omega^{-1}\text{m}^{-2}$) and largely independent of the Pt thickness when considering the same crystallographic orientation. This last observation, which is expected as G_r is basically an interfacial property, demonstrates the good reproducibility of the Pt/CFO interface achieved in our IN fabrication process. Therefore, the G_r values are consistently different between orientations ($G_r(001) > G_r(111)$ for any Pt thickness), being a solid evidence of the anisotropy of the spin-mixing conductance.

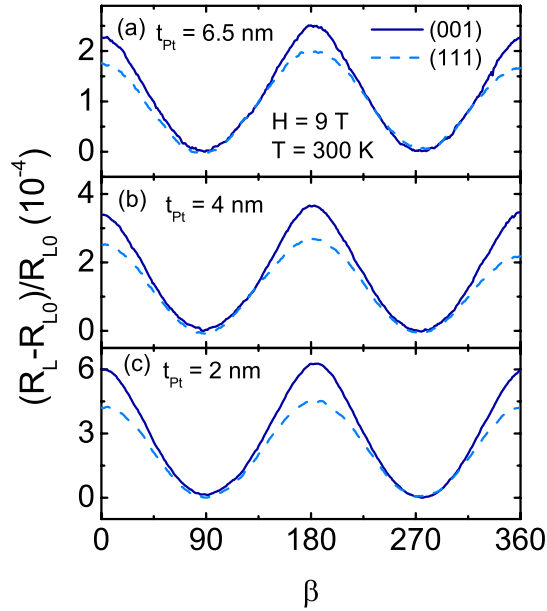


Figure 7.2: Angle-dependent longitudinal magnetoresistance measurements at 9 T and 300 K when rotating the magnetic field in a plane perpendicular to the current (*i.e.*, as a function of β) for epitaxial (001) and (111) Pt/CFO samples grown *in situ* with (a) 6.5 nm, (b) 4 nm and (c) 2 nm of Pt. R_L is the measured resistance and R_{L0} is the subtracted background.

Since the density of magnetic ions at the interface and their magnetic orienta-

tion determine the spin transfer, any detailed understanding for the observed difference $G_r(001) > G_r(111)$ should start by considering the microscopic nature of the atomic planes involved at the interface. This is far from obvious in spinel AB_2O_4 oxides; for instance in (111) there are 6 different atomic planes all of them being polar and, therefore, unstable. There are different mechanisms to solve this dipole-associated electrostatic energy divergence and, for this reason, the surface termination in (001) and (111) planes of spinel oxides is strongly dependent on the conditions used to prepare the surfaces. As a result, a definitive conclusion is still missing even for the most studied case of Fe_3O_4 (see Ref. [28] for a recent review). Nevertheless, theoretical and experimental trends indicate that in (001) surfaces the termination containing tetrahedrally coordinated Fe^{3+} ions is most commonly found, whereas in (111) surfaces both oxygen and tetrahedral terminations are more favorable [28]. A similar situation has been suggested for $MgAl_2O_4$ [29] and $CoFe_2O_4$ [30].

Recent first-principles calculations of G_r for different surfaces of $CoFe_2O_4$ [31] predict values of $2.82 \times 10^{14} \Omega^{-1} m^{-2}$ for the tetrahedral termination in the case of (001) orientation and $0.63 (1.15) \times 10^{14} \Omega^{-1} m^{-2}$ for the oxygen (tetrahedral) terminations in (111) orientation. The values for these stable (111) terminations are smaller than that predicted for the most stable (001) termination, which are similar to our experimental values and in agreement with the higher stability of the tetrahedrally coordinated Fe^{3+} planes in (001) and tetrahedrally coordinated Fe^{3+} and oxygen-terminated planes in (111) as argued above.

7.5 Ordinary magnetoresistance of Pt

Taking into account that the IN samples at the (001) orientation show the biggest amplitude of the magnetoresistance, we now analyze the full angular dependence ($R_L(\alpha)$, $R_L(\beta)$ and $R_L(\gamma)$) of the 6.5-nm, 4-nm and 2-nm-thick Pt *in-situ* samples. As we can see in Fig. 7.3, the observed behavior is quite different to the one observed in the *ex-situ* ones (Fig. 7.1). There are two puzzling points, which are not consistent with the current understanding of the SMR (Section 7.3): (i) there is a clear modulation in $R_L(\gamma)$ (Fig. 7.3(a)) and (ii) the change in $R_L(\beta)$ (Fig. 7.3(b)) is different to the change in $R_L(\alpha)$ (Fig. 7.3(c)).

A very controversial issue when placing Pt next to a FMI is the magnetization that can be induced in Pt by proximity effect, since Pt is close to the Stoner ferro-

magnetic instability [32–35]. If this was the case, $R_L(\gamma)$ measurements, which follow $R_L(\gamma) \propto \cos^2(\gamma)$, could be a signature of the anisotropic magnetoresistance (AMR) of the magnetized Pt. As AMR is sensitive to the variation of the magnetization with respect to the charge current direction, it would also be contributing to the $R_L(\alpha)$ measurements, being this configuration sensitive to both AMR and SMR.

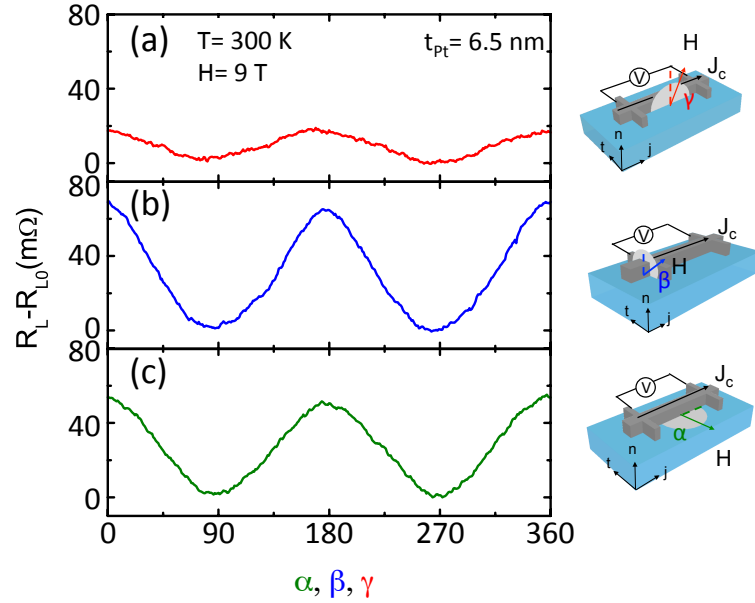


Figure 7.3: Angle-dependent longitudinal magnetoresistance measurements at 9 T and 300 K for the (001)IN(7) sample along (a) γ , (b) β and (c) α rotation planes. R_L is the measured longitudinal resistance and R_{L0} the subtracted background. The sketches in the right define the Hall bar geometry, the longitudinal measurement set-up and the angles α , β and γ .

The modulation that we observe in $R_L(\gamma)$ is present in all *in-situ* samples, irrespective of the Pt thickness. Thus, to further understand this behavior, we perform the same measurements at different temperatures, ranging from 40 to 300 K (Fig. 7.4). As observed, the normalized magnetoresistance in $R_L(\gamma)$, $\Delta R_L(\gamma)/R_{L0}$, is present for different Pt thicknesses and for all temperatures, being largest for the case of the thickest Pt. The fact that this contribution decreases when reducing thickness rules out that it arises from a proximity effect, which should be more relevant for thinner films [36]. Additionally, Fig. 7.4 shows that $\Delta R_L(\beta)/R_{L0}$, the purely SMR signal, becomes more important at low thicknesses, as expected [20, 23].

Another strategy to rule out the possibility of having AMR in a magnetized Pt is by performing FDMR measurements (Fig. 7.5). If AMR was present in our samples, we should obtain a distinct trend of the magnetoresistance when the field is applied

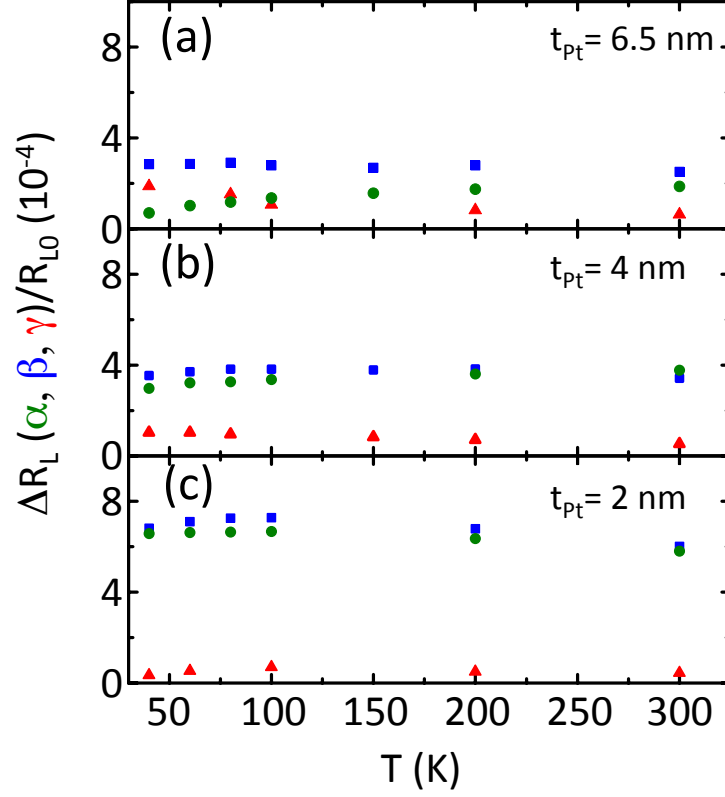


Figure 7.4: The amplitude of the ADMR at 9T as a function of temperature for the three different angles: α (green circles), β (blue squares) and γ (red triangles) for (a) (001)IN(7), (b) (001)IN(4) and (c) (001)IN(2) samples.

perpendicular to the charge current ($\vec{H} \parallel \hat{t}$ and $\vec{H} \parallel \hat{n}$) and when it is applied parallel to the charge current ($\vec{H} \parallel \hat{j}$). However, this is not what Fig. 7.5 shows, since the $\vec{H} \parallel \hat{n}$ curves have the same magnetoresistance trend as the $\vec{H} \parallel \hat{j}$ curves and the opposite from the one observed with $\vec{H} \parallel \hat{t}$, irrespective of the Pt thickness. Therefore, the AMR contribution should be discarded. This conclusion is in agreement with recent atomic selective magnetic measurements in similar Pt/CFO layers where, within the experimental resolution, no magnetic moment has been found in Pt [37].

It is worth noting the different resistance values measured for $\vec{H} \parallel \hat{j}$ and $\vec{H} \parallel \hat{n}$ at high fields, which accounts for the modulation in $R_L(\gamma)$ and it strongly depends on the Pt thickness, being more pronounced for the thickest sample. A possible explanation to this behavior is related to the ordinary magnetoresistance (OMR) in Pt. This magnetoresistance effect appears in metals and semiconductors and it occurs because conduction electrons are displaced from their trajectories by the Lorenz force

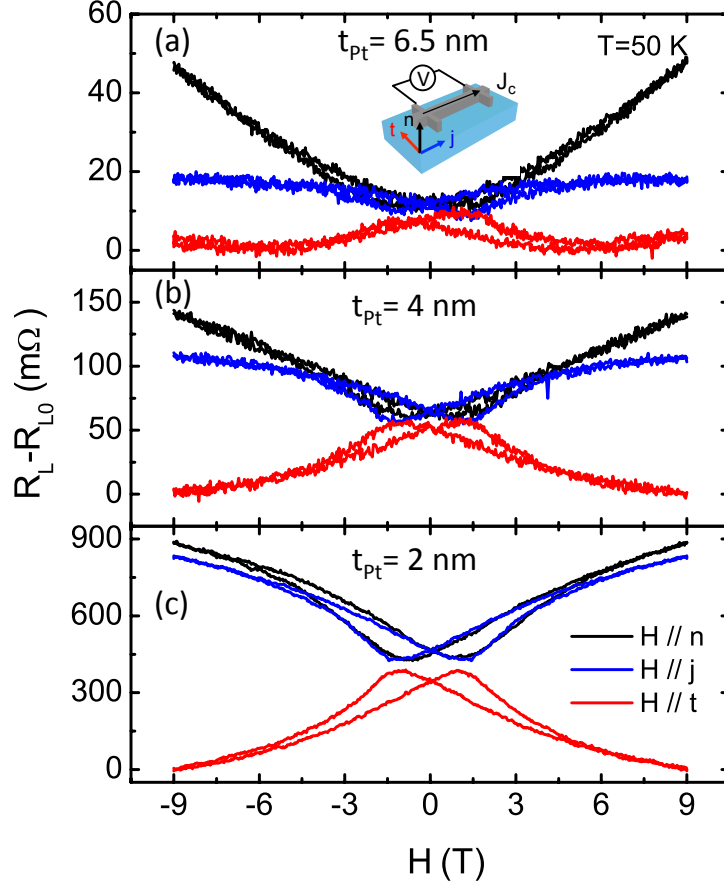


Figure 7.5: Longitudinal resistance R_L for (a) (001)IN(7), (b) (001)IN(4) and (c) (001)IN(7) as a function of the applied magnetic field, H , along \hat{t} (red curves), \hat{j} (blue curves) and \hat{n} (black curves). R_{L0} is the subtracted background. The orientations of the applied magnetic field and the measurement configuration are sketched in the inset. All measurements are done at 50 K.

exerted by an externally applied magnetic field. The magnetoresistance due to the OMR ($\Delta R_{OMR}/R_{L0}$) can be described by Kohler's rule, which depends on the applied field and resistivity in the form of [38, 39]:

$$\frac{\Delta R_{OMR}}{R_{L0}} = a \left(\frac{H}{\rho} \right)^n \quad (7.1)$$

where a and n are material dependent constants, with n between 1 and 2. This magnetoresistance should be characteristic of the Pt, but independent of the Pt thickness as far as its scattering length is not affected by size effects. To verify this, we subtract $R_L(\vec{H} \parallel \hat{n}) - R_L(\vec{H} \parallel \hat{j})$ to obtain ΔR_{OMR} and normalize it to R_{L0} , which

should correspond to the extra magnetoresistance present in the system. Subsequently, we plot the extra magnetoresistance as a function of H/ρ (see Fig. 7.6). As expected, all curves collapse into a parabola, with $n=1.8$, confirming that this extra effect is OMR. OMR has not been detected in previous studies on Pt/FMI [23, 40], due the large resistivity usually obtained in Pt thin films ($\sim 41\text{-}60 \mu\Omega\text{cm}$). Our Pt, grown *in situ* at 400°C on top of epitaxial (001) CFO, is fully textured in the (001) direction, leading to lower resistivity and therefore to a non-negligible OMR contribution.

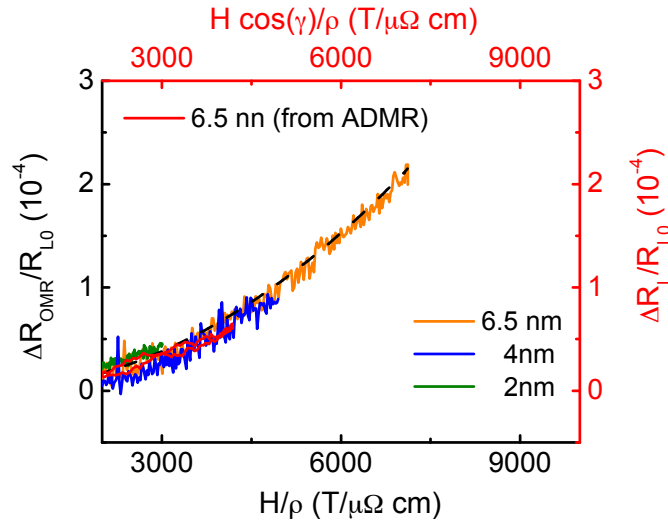


Figure 7.6: Orange, blue and green curves are the additional magnetoresistance observed for out-of-plane magnetic field, $(R_L(\vec{H} \parallel \hat{n}) - R_L(\vec{H} \parallel \hat{j}))/R_{L0}$, as a function of H/ρ for the three Pt/CFO samples with different Pt thicknesses at 50 K. The red curve is the longitudinal magnetoresistance $(R_L(\gamma) - R_{L0})/R_{L0}$ as a function of $H \cos(\gamma)/\rho$ for the 6.5-nm-thick Pt, at 300 K. The dashed black line is a guide for the eye.

Note that, once the OMR contribution is identified in $R_L(\vec{H} \parallel \hat{n})$, the curves arising solely from the SMR contribution are $R_L(\vec{H} \parallel \hat{t})$ and $R_L(\vec{H} \parallel \hat{j})$. As expected (see Fig. 7.5), the curves show a mirror symmetry, have the same shape with the Pt thickness and the SMR magnitude decreases with increasing thickness [17, 20, 23].

Now we can safely ascribe the behavior observed in Fig. 7.3(a) to OMR, where the angular dependence comes from the out-of plane component of the field ($H \cos(\gamma)$). If we plot the measured $R_L(\gamma)$ as a function of $H \cos(\gamma)/\rho$ we can see that it nicely follows Kohler's curve (red curve in Fig. 7.6). Note that the curves in Fig. 7.6 correspond to different temperatures, where FDMR measurements are done at 50 K and ADMR at 300 K. The fact that they all lie over the same curve is a clear evidence that OMR is temperature independent.

7.6 Sensing CFO surface magnetization

Once we have identified the coexistence of SMR and OMR in our system, we move now to the comparison between the magnetic properties of the CFO thin films and the spin Hall magnetoresistance of the Pt/CFO bilayers. Figure 7.7(a) shows the hysteresis loops $M(H)$ of the (001)IN(2) sample obtained by applying the magnetic field H along \hat{t} and \hat{n} directions at 50 K. As can be seen from the hysteresis loop when the field is applied in plane, $M(\vec{H} \parallel \hat{t})$, the large coercive fields $H_c(\hat{t}) \approx \pm 1.2$ T and the fact that hysteresis only disappears at ≈ 5 T are signatures of the strong magnetic anisotropy typical of CFO thin films [41, 42]. The shape of the hysteresis loop when the field is applied out of plane, $M(\vec{H} \parallel \hat{n})$, indicates a harder magnetization axis and, correspondingly, the coercive field $H_c(\hat{n}) \approx \pm 0.44$ T and the magnetic remanence are smaller. The saturation magnetization ($M_s = 230$ emu/cm³) is lower than the corresponding bulk value as commonly observed in spinel thin films [43–46] and attributed to the presence of antiphase boundaries (APB) [43, 44] or to surface anisotropy effects [14]. The diamagnetic background, arising mainly from the STO substrate, has been corrected by subtracting a linear term $\chi_d H$, where χ_d is the high-field slope of the raw data. The χ_d values are practically identical for all H orientations, as expected for the cubic STO substrate (not shown). Note that the presence of such background, however, would conceal any possible contribution from non-saturating behavior of the CFO film at high fields, as commonly observed in these systems [15, 41, 46, 47].

Figure 7.7(b) shows the longitudinal resistance of the (001)IN(2) sample measured at different orthogonal H orientations ($R_L(\vec{H} \parallel \hat{j})$, $R_L(\vec{H} \parallel \hat{t})$ and $R_L(\vec{H} \parallel \hat{n})$), after subtracting the background resistance. When applying a field $\vec{H} \parallel \hat{n}$, the transverse component of the magnetization m_t should be reduced and, following Eq. 2.26, $R_L(\vec{H} \parallel \hat{n})$ should increase with H . A similar behavior is expected for $R_L(\vec{H} \parallel \hat{j})$ when applying a field $\vec{H} \parallel \hat{j}$. Accordingly, $R_L(\vec{H} \parallel \hat{t})$ should decrease with increasing H . The experimental data in Fig. 7.7(b) confirms these trends. As expected, this behavior shares similarities and is reminiscent of the $M(H)$ curves in Fig. 7.7(a) because, as shown by Eq. 2.26, the field evolution of $M(H)$ should translate into $R_L(H)$. However, detailed inspection of $R_L(H)$ curves reveals substantial differences. First, of the highest relevance is the observation that, for $H > 5$ T, $R_L(\vec{H} \parallel \hat{n})$ and $R_L(\vec{H} \parallel \hat{j})$ keep increasing (decreasing for $\vec{H} \parallel \hat{t}$) almost linearly with H up to the highest field (9 T), while bulk CFO appears to be magnetically saturated. In addition, the fact that

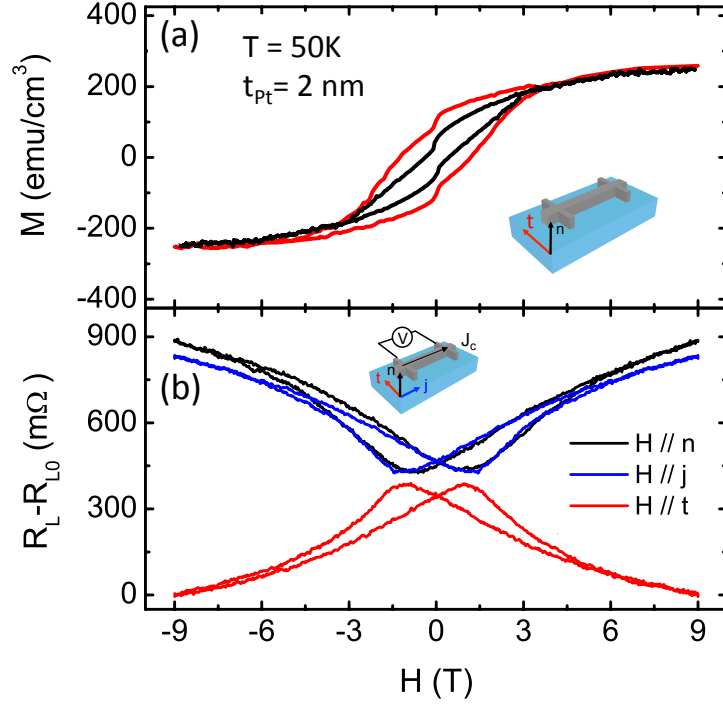


Figure 7.7: (a) Magnetic hysteresis loops for the 40-nm-thick (001) CFO sample with the 2-nm-thick Pt bar on top. The magnetic field H is applied along \hat{t} (red curve) and \hat{n} (black curve), as defined in the inset. Longitudinal resistance R_L for the same sample as a function of H , applied along \hat{t} (red curve), \hat{n} (black curve) and \hat{j} (blue curve). R_{L0} is the subtracted background. The orientations of the applied field and the measurement configuration are sketched in the inset. All measurements are done at 50 K.

$R_L(\vec{H} \parallel \hat{n})$ and $R_L(\vec{H} \parallel \hat{j})$ are almost identical (except for the OMR contribution at high fields) also indicates similar in-plane and out-of-plane magnetization responses, a property which cannot be extracted from the $M(H)$ dependence.

In order to rationalize these observations, we start noticing that the field dependence of $R_L(H)$ is consistent with Eq. 2.26 if one assumes a magnetization at the surface with a very hard magnetic response. Such a behavior has been commonly observed in spinel oxides, and assigned to large surface magnetic anisotropy [14], to the presence of APB [43, 44, 46] or to distinct magnetic phases [41, 45, 47]. Whereas a significant contribution of surface magnetic anisotropy is unlikely, because it would give a distinct contribution when measuring the $R_L(H)$ with in-plane or out-of-plane fields, which is not observed, APB or the presence of a distinct surface magnetic phase could explain the overall observed behavior. Indeed, at APBs, as the field increases and approaches saturation, the magnetization at the center of the antiphase gradually develops a com-

ponent perpendicular to the field and the corresponding domain wall shrinks [44, 48]. Ultimately, they produce an isotropic high-field magnetic susceptibility, as observed in Fig. 7.7(b), and the magnetization does not reach its full saturation value. Finally, the presence of a distinct magnetic phase at the surface of CFO thin films, either resulting from the growth mechanism [41] or induced by extrinsic surface defects [47], with magnetic properties different from the bulk, closely resembles our prediction of the surface magnetization from the SMR measurements. Discrimination between those scenarios cannot be safely done on the basis of the available data. We conclude that SMR is extremely sensitive to fine details of the magnetic ordering at the NM/FMI interface and $R_L(H)$ data are thus fingerprints of a distinct surface magnetization which, although not discernible in the bulk-sensitive magnetization experiments, largely dominates the longitudinal SMR.

7.7 Conclusions

From this systematic analysis, where different crystallographic orientations and fabrication procedures have been studied, we can conclude that SMR is at the origin of the magnetoresistance of Pt films in all samples. Although the observed SMR is a robust phenomenon, its magnitude depends on the interface preparation conditions, being optimal when the samples are prepared *in situ*. The spin-mixing conductance at Pt/CFO is found to be similar to those reported for other NM/FMI heterostructures. Most importantly, the observation that (001) and (111) CFO films have clearly different SMR illustrates that atomic configuration of the magnetic atoms at NM/FMI interfaces have an important effect in the spin-mixing conductance, as predicted theoretically [1, 31].

Moreover, we have shown that for the particular case of the *in-situ* grown Pt/CFO films, an additional feature appears at high magnetic fields. This additional effect originates from the ordinary magnetoresistance of Pt. Finally, we have compared the field-dependent longitudinal resistance arising from the SMR to the bulk magnetization of the CFO. This analysis reveals important differences that we attribute to the significant role of surface/interface magnetism in systems such as spinels where strong competition of magnetic interactions takes place. This shows the tremendous potential of SMR to probe the surface magnetization of insulating ferromagnets, which cannot be detected by other magnetometric techniques.

All these results might have important implications for the design of future spin-

tronic devices based on insulators.

References

- [1] X. Jia, K. Lui, K. Xia, and G. E. W. Bauer, *Europhys. Lett.* **96**, 17005 (2011).
- [2] C. Burrowes, B. Heinrich, B. Kardasz, E. A. Montoya, E. Girt, Yiyun Sun, Youngyeal Song, and Mingzhong Wu, *Appl. Phys. Lett.* **100**, 092403 (2012).
- [3] M. B. Jungfleisch, V. Lauer, R. Neb, A. V. Chmak, and B. Hillebrands, *Appl. Phys. Lett.* **103**, 022411 (2013).
- [4] M. Weiler, M. Althammer, M. Schreier, J. Lotze, M. Pernpeintner, S. Meyer, H. Huebl, R. Gross, A. Kamra, J. Xiao, Y.-T. Chen, H. Jiao, G. E. W. Bauer, and S. T. B. Goennenwein, *Phys. Rev. Lett.* **111**, 176601 (2013).
- [5] M. Schreier, N. Roschewsky, E. Dobler, S. Meyer, H. Huebl, R. Gross, and S. T. B. Goennenwein, *Appl. Phys. Lett.* **103**, 242404 (2013).
- [6] N. Vlietstra, J. Shan, B. J. van Wees, M. Isasa, F. Casanova, and J. Ben Youssef, and S. T. B. Goennenwein, *Phys. Rev. B* **90**, 174436 (2014).
- [7] K. Uchida, J. Xiao, H. Adachi, J. Ohe, S. Takahashi, J. Ieda, T. Ota, Y. Kajiwara, H. Umezawa, H. Kawai, G. E. W. Bauer, S. Maekawa, and E. Saitoh, *Nature Materials* **9**, 894 (2010).
- [8] E. Saitoh, M. Ueda, H. Miyajima, and G. Tatara, *Appl. Phys. Lett.* **88**, 182509 (2006).
- [9] K. Ando, S. Takahashi, K. Harii, K. Sasage, J. Ieda, S. Maekawa, and E. Saitoh, *Phys. Rev. Lett.* **101**, 036601 (2008).
- [10] Y. Kajiwara, K. Harii, S. Takahashi, J. Ohe, K. Uchida, M. Mizuguchi, H. Umezawa, H. Kawai, K. Ando, K. Takanashi, S. Maekawa, and E. Saitoh, *Nature* **464**, 262 (2010).

- [11] E. Villamor, M. Isasa, S. Velez, A. Bedoya-Pinto, P. Vavassori, L. E. Hueso, F. S. Bergeret, and F. Casanova, *Phys. Rev. B* **91**, 020403 (R) (2015).
- [12] F. K. Dejene, N. Vlietstra, D. Luc, X. Waintal, J. Ben Youssef, and B. J. van Wees, *Phys. Rev. B* **91**, 100404 (R) (2015).
- [13] J. C. Slonczewski, *Phys. Rev.* **110**, 1341 (1958).
- [14] R. H. Kodama, A. E. Berkowitz, E. J. McNiff, Jr., and S. Foner, *Phys. Rev. Lett.* **77**, 394 (1996).
- [15] N. Dix, I. Fina, R. Bachelet, L. Fàbrega, C. Kanamadi, J. Fontcuberta, and F. Sánchez, *Appl. Phys. Lett.* **102**, 172907 (2013).
- [16] L. Liu, R. A. Buhrman and D. C. Ralph, *arXiv*: 1111.3702.
- [17] H. Nakayama, M. Althammer, Y.-T. Chen, K. Uchida, Y. Kajiwara, D. Kikuchi, T. Ohtani, S. Geprägs, M. Opel, S. Takahashi, R. Gross, G. E. W. Bauer, S. T. B. Goennenwein, and E. Saitoh, *Phys. Rev. Lett.* **110**, 206601 (2013).
- [18] J. C. Rojas-Sánchez, N. Reyren, P. Laczkowski, W. Savero, J. P. Attané, C. Deranlot, M. Jamet, J. M. George, L. Vila and H. Jaffrès, *Phys. Rev. Lett.* **112**, 106602 (2014).
- [19] Y. Kajiwara, K. Harii, S. Takahashi, J. Ohe, K. Uchida, M. Mizuguchi, H. Umezawa, H. Kawai, K. Ando, K. Takanashi, S. Maekawa, and E. Saitoh, *Nature* **464**, 262 (2010).
- [20] N. Vlietstra, J. Shan, V. Castel, B. J. van Wees and J. Ben Youssef, *Phys. Rev. B* **87**, 184421 (2013).
- [21] C. Hahn, G. de Loubens, O. Klein, M. Viret, V. V. Naletov, and J. Ben Youssef, *Phys. Rev. B* **87**, 174417 (2013).
- [22] N. Vlietstra, J. Shan, V. Castel, J. Ben Youssef, G. E. W. Bauer, and B. J. van Wees, *Appl. Phys. Lett.* **103**, 032401 (2013).
- [23] M. Althammer, S. Meyer, H. Nakayama, M. Schreier, S. Altmannshofer, M. Weiler, H. Huebl, S. Geprägs, M. Opel, R. Gross, D. Meier C. Klewe, T. Kuschel, J.-M. Schmalhorst, G. Reiss, L. Shen, A. Gupta, Y.-T. Chen, G. E. W. Bauer, E. Saitoh, and S. T. B. Goennenwein, *Phys. Rev. B* **87**, 224401 (2013).

- [24] Z. Qiu, K. Ando, K. Uchida, Y. Kajiwara, R. Takahashi, H. Nakayama, T. An, Y. Fujikawa, and E. Saitoh, *Appl. Phys. Lett.* **103**, 092404 (2013).
- [25] V. Castel, N. Vlietstra, B. J. van Wees and J. B. Youssef, *Appl. Phys. Lett.* **101**, 132414 (2012).
- [26] F. D. Czeschka, L. Dreher, M. S. Brandt, M. Weiler, M. Althammer, I.-M. Imort, G. Reiss, A. Thomas, W. Schoch, W. Limmer, H. Huebl, R. Gross, and S. T. B. Goennenwein, *Phys. Rev. Lett.* **107**, 046601 (2011).
- [27] Y. Ando, K. Ichiba, S. Yamada, E. Shikoh, T. Shinjo, K. Hamaya, and M. Shiraishi, *Phys. Rev. B* **88**, 140406(R) (2013).
- [28] H. Kuhlenbeck, S. Shaikhutdinov and H.-J. Freund, *Chem. Rev.* **113**, 3986 (2013).
- [29] W.-Z. Li, L. Kovarik, D. Mei, J. Liu, Y. Wang and C. H. F. Peden, *Nature Comm.* **4**, 2481 (2013).
- [30] N. Ballarini, F. Cavani, S. Passeri, L. Pesaresi, A.F. Lee, and K. Wilson, *Appl. Catalysis A* **366**, 184 (2009).
- [31] L. Wang, K. Xia and G. E. W. Bauer, *private communication*.
- [32] J. J. Hauser, *Phys. Rev.* **187**, 580 (1969).
- [33] W. J. Antel, Jr, M. M. Schwickert, T. Lin, W. L. O'Brien, and G. R. Harp, *Phys. Rev. B* **60**, 12933 (1999).
- [34] M. Weiler, M. Althammer, F. D. Czeschka, H. Huebl, M. S. Wagner, M. Opel, I. Imort, G. Reiss, A. Thomas, R. Gross, and S. T. B. Goennenwein, *Phys. Rev. Lett.* **108**, 106602 (2012).
- [35] S. Y. Huang, X. Fan, D. Qu, Y. P. Chen, W. G. Wang, J. Wu, T. Y. Chen, J. Q. Xiao, and C. L. Chien, *Phys. Rev. Lett.* **109**, 107204 (2012).
- [36] J. X. Li, M. W. Jia, Z. Ding, J. H. Liang, Y. M. Luo, and Y. Z. Wu, *Phys. Rev. B* **90**, 214415 (2014).
- [37] M. Valvidares, N. Dix, M. Isasa, K. Ollefs, W. Wilhelm, F. Sanchez, E. Pellegrin, A. Bedoya-Pinto, P. Gargiani, L. E. Hueso, F. Casanova and J. Fontcuberta, *arXiv:1510.01080*.

- [38] N. Cusack, *The electrical and magnetic properties of solids*, Chapter 6, pg 132, Longmans (1958).
- [39] A. B. Pippard, *Magnetoresistance in metals* (Cambridge University Press, 1989).
- [40] S. Velez, V. N. Golovach, A. Bedoya-Pinto, M. Isasa, E. Sagasta, L. E. Hueso, F. S. Bergeret and F. Casanova, *arXiv:1502.04624*.
- [41] F. Rigato, J. Geshev, V. Skumryev, and J. Fontcuberta, *J. Appl. Phys.* **106**, 113924 (2009).
- [42] A. Lisfi, C. M. Williams, L. T. Nguyen, J. C. Lodder, A. Coleman, H. Corcoran, A. Johnson, P. Chang, A. Kumar, and W. Morgan, *Phys. Rev. B* **76**, 054405 (2007).
- [43] D. T. Margulies, F. T. Parker, M. L. Rudee, F. E. Spada, J. N. Chapman, P. R. Aitchison, and A. E. Berkowitz, *Phys. Rev. Lett.* **79**, 5162 (1997).
- [44] W. Eerenstein, T. T. M. Palstra, S. S. Saxena, and T. Hibma, *Phys. Rev. Lett.* **88**, 247204 (2002).
- [45] M. Foerster, J.M. Rebled, S. Estradé, F. Sánchez, F. Peiró, and J. Fontcuberta, *Phys. Rev. B* **84**, 144422 (2011).
- [46] J.-B. Moussy, S. Gota, A. Bataille, M.-J. Guittet, M. Gautier-Soyer, F. Delille, B. Dieny, F. Ott, T. D. Doan, P. Warin, P. Bayle-Guillemaud, C. Gatel and E. Snoeck, *Phys. Rev. B* **70**, 17448 (2004).
- [47] C. Jin, H. Liu, P. Li, D. F. Kuang and H. L. Bai, *J. Appl. Phys.* **110**, 013917 (2011).
- [48] R. G. S. Sofin, S. K. Arora, and I. V. Shvets, *Phys. Rev. B* **83**, 134436 (2011).

Chapter 8

Conclusions and future perspectives

This thesis presents a complete research work mainly devoted to the spin-to-charge current conversion in metals which is central to the new field of spin orbitronics. In this comprehensive study, we analyze: (i) the spin transport properties of different metals; (ii) the spin-to-charge conversion in bulk metals, due to the inverse spin Hall effect (ISHE); (iii) the spin-to-charge conversion in a two-dimensional electron gas, due to inverse Rashba-Edelstein effect (IREE); (iv) the newly discovered spin Hall magnetoresistance (SMR).

First, the spin transport properties of Ag, Pt and Au have been studied. For the case of Ag, as it has a relatively long spin diffusion length (> 100 nm), we have used a conventional lateral spin valve. Here we prove that controlling the Ag growth is of outmost importance to enhance the spin transport properties. If we are able to grow epitaxial Ag, the grain boundary scattering is largely suppressed, and thus, the decrease in the resistivity leads to an increase in the spin diffusion length. For Au and Pt, since they have shorter spin diffusion lengths (< 100 nm) we use spin absorption devices. The values that we obtain are in good agreement with literature values and, therefore, we conclude that spin absorption is a reliable technique to obtain the spin diffusion length of heavy metals.

Moreover, using the same devices, we are able to measure the spin Hall effect in Au and Pt. To quantify the spin-to-charge current conversion in the bulk metals, we define the spin Hall angle, which determines the efficiency of the conversion. From our results, we systematically observe a smaller spin Hall angle value compared to values estimated with other techniques. We believe that this might be due to a partial depolarization of

the spin current at the interface in our devices. However, the estimation of this partial depolarization is not trivial as it strongly depends on the interface quality. Analyzing the evolution of the spin Hall effect as a function of temperature, we study the different mechanisms contributing to the effect. Whereas the intrinsic mechanism is dominant for the case of Pt, Au seems to be controlled by the extrinsic contributions. More importantly, we observe a clear evidence of the phonon skew scattering contribution in Au. Our results, suggest that the phonon skew scattering, ignored until now, should be taken into account specially in metals with a low resistivity.

Using spin absorption devices, spin-to-charge conversion experiments were performed in a more exotic material, Bi. Unlike in the case of Au and Pt, for Bi we observe a very strong spin absorption at the metallic surface state. Therefore, the spin-to-charge current conversion will not occur at the bulk any longer, but it will happen at the Bi metallic surface due to the inverse Rashba-Edelstein effect. By analyzing its temperature dependence we observe a clear sign crossover, which according to our theoretical analysis arises from the complex structure of the surface states of Bi.

Finally, we explore the SMR in Pt/CFO bilayers where the CFO layer is grown in (001) or (111) orientation and Pt is *in-situ* or *ex-situ* grown on top of CFO. From a systematic analysis we observe that the magnitude of the SMR strongly depends on the growing conditions of Pt, being optimal when it is grown *in-situ*. Moreover, the spin-mixing conductance is found to be different for (001) or (111) orientations, which means that it depends on the atomic configuration of the magnetic atoms at the Pt/CFO interface. Last but not least, we proved that SMR can be a very powerful tool to sense the surface magnetization of ferromagnetic insulators, other ways not possible with other magnetometric techniques.

We believe that all these findings are timely and of interest for the fields of spintronics and magnetism and offer an appropriate platform to investigate deeper all the effects presented in this thesis as well as to unveil yet unpredicted spin-dependent phenomena.

In a next stage, taking advantage of the acquired knowledge, some particular steps can be taken in order to improve the spin-to-charge conversion efficiency. For example, for the case of the spin Hall effect in Au, additional work would be needed to better quantify the phonon-induced skew scattering by systematically varying the residual resistivity. Moreover, a similar experiment to the one shown by Onoda *et al.* for the

anomalous Hall effect (AHE) [1] is still missing for the spin Hall effect (SHE). If this experiment was performed, we would observe a transition from an intrinsic contributions dominating situation (moderately dirty limit) into a skew scattering dominating situation (ultra clean limit) by decreasing the resistivity. This brings us to the idea that, by controlling the resistivity, the different contributions acting on the SHE can be controlled. This might be a key point to tune the spin Hall angle and, thus, improve the spin-to-charge conversion efficiency.

Regarding the IREE experiments, other systems showing a strong Rashba spin-splitting can be studied, as the IREE is expected to be more efficient than the ISHE for the spin-to-charge current conversion.

Last, the acquired expertise of the SMR experiments can be applied to sense the surface magnetization of complex materials such as paramagnetic insulators (such as LaCoO_3) or antiferromagnetic oxides (such as Cr_2O_3). Moreover, SMR can also be used as a powerful tool to read the information stored in a ferromagnetic insulator, just passing a current through a NM metal. The resistance of the metal will change depending on the orientation of the FMI and thus, two distinct resistance states (*i.e.* ON state and OFF state) should be distinguishable. Finally, the interpretation of the SMR may not be unique. Since this is an effect happening at the interface, some authors [2] have suggested that the broken inversion symmetry at the FMI/NM surface might also be the responsible for the observed magnetoresistance and, therefore, we would have Rashba-induced magnetoresistance instead of SMR. This controversy is similar to the one generated by the spin-orbit torques discussed in Section 1.2.3. Therefore, understanding the origin of this magnetoresistance, which might also help to understand the origin of spin-orbit torques, might be an important direction to follow in the SMR field in particular and in spin orbitronics in general.

References

- [1] S. Onoda, N. Sugimoto, and N. Nagaosa, *Phys. Rev. B* **77**, 165103 (2008).
- [2] V. L. Grigoryan, W. Guo, G. E. W. Bauer and J. Xiao, *Phys. Rev. B* **90**, 161412(R) (2014).

Appendix A

Fabrication parameters for LSVs

Throughout this thesis we have fabricated Ag/Py (Chapter 4) LSVs. This process is divided in two main steps which are explained below.

A.1 First step: NM channel

- Metal deposition:

40-nm-thick Ag films are deposited into a Si substrate with a crystallographic orientation of (110) using a plasma sputtering system. If the Si substrate is etched with hydrofluoric (HF) acid before the Ag deposition, the native Si-oxide is removed, enabling the growth of epitaxial Ag. If the substrate is not treated with HF, the native oxide remains, leading to a polycrystalline Ag film. The deposition conditions for Ag are listed below:

- $P_{base} = 7 \times 10^{-7}$ mbar
- $Power_{plasma} = 40$ W
- $P_{plasma} = 4 \times 10^{-7}$ mbar
- $rate = 1.5 \text{ \AA/s}$

where, P_{base} is the base pressure, $Power_{plasma}$ and P_{plasma} are the power and pressure to create the plasma, respectively, and $rate$ is the deposition rate.

- Spin coating conditions:

1. Spin coating of ma N-2403 negative resist at 6000 rpm for 30 seconds to obtain an homogeneous layer around 175 nm thick.
 2. Baking on the hot plate at 90°C for 60 seconds.
- E-beam lithography parameters: In this step we transfer the pattern of the NM channel.
 - Acceleration voltage: 20 kV
 - Aperture: 10 μm
 - Write field: $100 \times 100 \mu\text{m}^2$
 - Dose: 40 $\mu\text{C}/\text{cm}^2$

- Developing:

The sample is immersed in D-525 developer for 60 seconds and then rinsed in deionized water.

- Ar-ion milling:

As seen in Chapter 4, two consecutive Ar-ion milling processes are needed: one to take out the Ag which is not protected under the negative resist and the other one to remove the redeposited material from the edges of the remaining Ag. The first etching is done at $\alpha = 80^\circ$ for $t=175$ seconds and the other one at $\alpha = 10^\circ$ for $t=88$ seconds, both with the same Ar-ion beam power and acceleration voltage:

- $V_{beam} = 300 \text{ V}$
- $I_{beam} = 50 \text{ mA}$
- $V_{acceleration} = 50 \text{ V}$

where V_{beam} and I_{beam} are the voltage and the current of the Ar-ion beam, respectively, $V_{acceleration}$ is the voltage to accelerate the Ar plasma against the surface, t is the milling time and α is the angle between the Ar-ion beam and the substrate plane.

- Lift-off:

After these milling processes, the sample is immersed in acetone so that the negative resist is removed. Now the sample is ready for a second lithography process (See Fig. A.1(a)).

A.2 Second step: FM electrodes

- Spin coating conditions:
 1. Spin coating of 495K PMMA A4 resist at 4000 rpm for 60 seconds to obtain an homogeneous layer around 180 nm thick.
 2. Baking on the hot plate at 195°C for 60 seconds.
 3. Spin coating of 950K PMMA A2 resist at 4000 rpm for 60 seconds to obtain an homogeneous layer around 40 nm thick.
 4. Baking on the hot plate at 195°C for 60 seconds.
- E-beam lithography parameters: In this step we transfer the pattern of the FM electrodes.
 - Acceleration voltage: 10 kV
 - Aperture: 10 μm
 - Write field: 100 \times 100 μm^2
 - Dose: 175 $\mu\text{C}/\text{cm}^2$
- Developing:

The sample is immersed in MIPK: IPA 1:3 for 30 seconds and then rinsed in IPA.
- Ar-ion milling:

An Ar-ion milling removes all the resist left overs or possible oxide formation from the NM/FM interface. Thus, this is essential to obtain transparent interfaces. The deposition conditions are listed below:

 - $V_{beam} = 300 \text{ V}$
 - $I_{beam} = 50 \text{ mA}$
 - $V_{acceleration} = 50 \text{ V}$
 - $\alpha = 10^\circ$
 - $t = 30 \text{ s}$
- Metal deposition:

45 nm of Py are deposited in an ultrahigh vacuum evaporator with the following parameters:

- $P_{base} = 7 \times 10^{-9}$ mbar
- $P_{deposition} = 4 \times 10^{-8}$ mbar
- Rate = 0.5 \AA/s

- Lift off:

The lift-off process is done by immersing the sample in acetone for several hours. At this point the sample is ready to be measured (See Fig. A.1(b)).

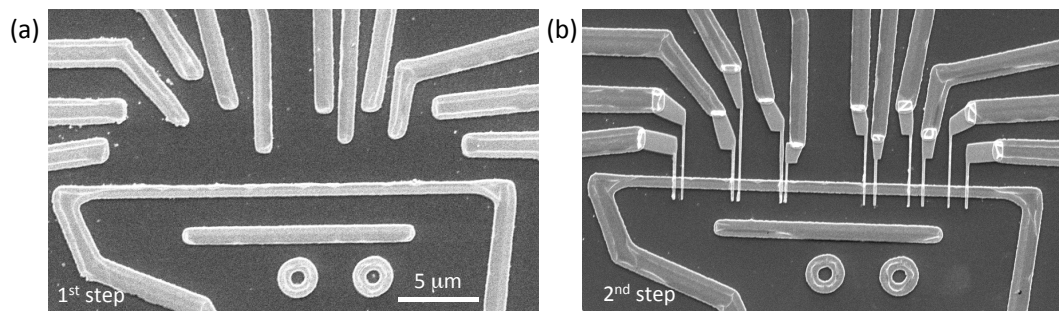


Figure A.1: (a) First step of the fabrication process where the NM channel is defined. (b) Second step of the fabrication process, where the FM electrodes are deposited on top of the NM channel.

Appendix B

Fabrication parameters for SA devices

The spin coating conditions and e-beam lithography parameters are summarized as follows:

B.1 First step: FM electrodes

- Spin coating:
 1. Spin coating of ZEP-520A7 resist at 4000 rpm for 60 seconds to obtain an homogeneous layer around 200 nm thick.
 2. Baking on the hot plate at 180°C for 300 seconds.
- E-beam lithography parameters: In this step we transfer the pattern of the FM electrodes.
 - Acceleration voltage: 10 kV
 - Aperture: 10 μm
 - Write field: 100 \times 100 μm^2
 - Dose: 35 $\mu\text{C}/\text{cm}^2$
- Developing:

The sample is immersed in ZED-N50 for 30 seconds and then rinsed in IPA.

- Metal deposition:

35 nm of Py are deposited in an ultrahigh vacuum evaporator with the following parameters:

- $P_{base} = 7 \times 10^{-9}$ mbar
- $P_{deposition} = 4 \times 10^{-8}$ mbar
- Rate = 0.5 Å/s

- Lift-off:

The lift-off process is done immersing the sample in ZD-MAC for several hours. Now the sample is ready for a second lithography step (See Fig. B.1(a))

B.2 Second step: MS wire

- Spin coating:

1. Spin coating of 495K PMMA A4 resist at 4000 rpm for 60 seconds to obtain an homogeneous layer around 180 nm thick.
2. Baking on the hot plate at 195°C for 60 seconds.
3. Spin coating of 950K PMMA A2 resist at 4000 rpm for 60 seconds to obtain an homogeneous layer around 40 nm thick.
4. Baking on the hot plate at 195°C for 60 seconds.

- E-beam lithography parameters: In this step we transfer the pattern of the MS wire.

- Acceleration voltage: 10 kV
- Aperture: 10 μm
- Write field: 100 \times 100 μm^2
- Dose: 150 $\mu\text{C}/\text{cm}^2$

- Developing:

The sample is immersed in MIPK: IPA 1:3 for 30 seconds and then rinsed in IPA.

- Metal deposition:

As it has been shown in Chapter 5 and Chapter 6 three different metals has been tested as MS wire: Pt, Au and Bi. All of them have been evaporated in different chambers. Below we list the deposition parameters for each metal.

- **Pt** is deposited in a magnetron sputtering system under the following conditions:

- * $P_{base} = 7 \times 10^{-7}$ mbar
- * $Power_{plasma} = 80$ W
- * $P_{plasma} = 4 \times 10^{-7}$ mbar
- * $rate = 1.3 \text{ \AA/s}$

- **Au** is evaporated in an ultrahigh vacuum chamber by e-beam evaporation. For adhesion purposes, a thin Ti layer was evaporated before Au in the same chamber. The deposition conditions for both metals are listed below:

- * $P_{base} = 7 \times 10^{-9}$ mbar
- * $P_{deposition} = 4 \times 10^{-8}$ mbar
- * Ti rate = 0.5 \AA/s
- * Au rate = 2.5 \AA/s

- **Bi** is evaporated by e-beam evaporation under the following conditions:

- * $P_{base} = 1 \times 10^{-7}$ mbar
- * $P_{deposition} = 1 \times 10^{-6}$ mbar
- * Bi rate = 0.67 \AA/s

Bi was deposited in Instituto de Nanociencia de Aragón (INA) in Zaragoza.

- Lift-off:

The lift-off process is done immersing the sample in acetone for several hours. Now the sample is ready for the last lithography step (See Fig. B.1(b))

B.3 Third step: NM channel

- Spin coating

1. Spin coating of 495K PMMA A4 resist at 4000 rpm for 60 seconds to obtain an homogeneous layer around 180 nm thick.

2. Baking on the hot plate at 195°C for 60 seconds.
 3. Spin coating of 950K PMMA A2 resist at 4000 rpm for 60 seconds to obtain an homogeneous layer around 40 nm thick.
 4. Baking on the hot plate at 195°C for 60 seconds.
- E-beam lithography parameters: In this step we transfer the pattern of the NM channel.
 - Acceleration voltage: 10 kV
 - Aperture: 10 μm
 - Write field: $100 \times 100 \mu\text{m}^2$
 - Dose: 145 $\mu\text{C}/\text{cm}^2$

- Developing:

The sample is immersed in MIPK: IPA 1:3 for 30 seconds and then rinsed in IPA.

- Ar-ion milling

To obtain clean interfaces between the NM channel on the one hand and the FM electrodes and the MS wire on the other hand, an Ar-ion milling is performed. In this way all the possible resist left overs or oxide formation is removed from the interface. The Ar-ion milling is done under the following conditions:

- $V_{beam} = 300 \text{ V}$
- $I_{beam} = 50 \text{ mA}$
- $V_{acceleration} = 50 \text{ V}$
- $\alpha = 10^\circ$
- $t = 20 \text{ s}$

- Metal deposition:

Cu is thermally evaporated in an ultrahigh vacuum chamber under the following conditions:

- $P_{base} = 7 \times 10^{-9} \text{ mbar}$
- $P_{deposition} = 4 \times 10^{-8} \text{ mbar}$

- $T_{melt} = 1300^{\circ}\text{C}$
- Cu rate = 1.4 \AA/s

- Lift-off:

The lift-off process is done immersing the sample in acetone for several hours.

Now the sample is ready for the electrical characterization (See Fig. B.1(c)).

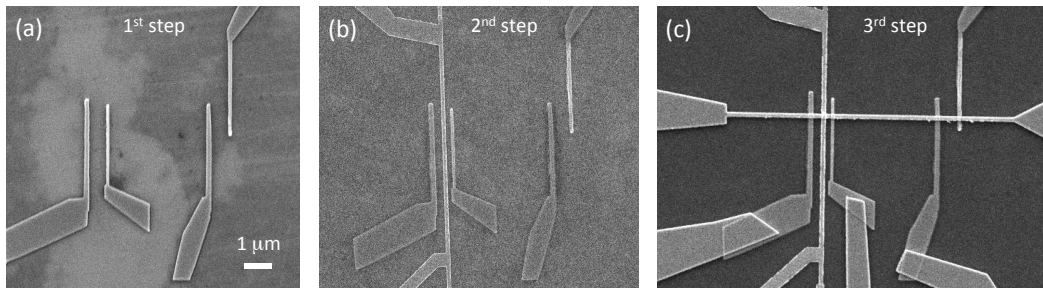


Figure B.1: (a) First step of the fabrication process where the FM electrodes are defined. (b) Second step of the fabrication process, where the MS is inserted in the middle of one of the pairs of the FM electrodes. (c) Third step where the NM channel is patterned, bridging the FM electrodes and the middle MS wire.

Appendix C

Fabrication parameters for FMI/NM bilayers

The spin coating conditions and e-beam lithography parameters are summarized below for the two types of Pt/CFO samples that have been used through this thesis.

C.1 Ex-situ samples

- FMI deposition:

The CoFe_2O_4 is deposited using a KrF laser with fluence of 1.5(3) J/cm² and a repetition rate of 5 Hz at a temperature of about 550 °C and oxygen pressure P_{O_2} = 0.1 mbar. This CFO layers are grown in Institut de Ciència de Materials de Barcelona (ICMAB).

- Spin coating:

1. Spin coating of 950K PMMA A2 resist at 4000 rpm for 60 seconds to obtain an homogeneous layer of 40 nm thickness.
2. Bake it on the hot plate at 195°C for 60 seconds.

- eBL exposure:

In this step we pattern the Hall bar.

- Acceleration voltage: 10 kV
- Aperture: 10 μm
- Write field: $100 \times 100 \mu\text{m}^2$
- Dose: 35 $\mu\text{C}/\text{cm}^2$

- Developing:

The sample is immersed in MIBK: IPA 1:3 for 30 seconds and then rinsed in IPA.

- Metal deposition:

Pt is deposited in a magnetron sputtering system under the following conditions:

- $P_{base} = 7 \times 10^{-7}$ mbar
- $\text{Power}_{plasma} = 80$ W
- $P_{plasma} = 4 \times 10^{-7}$ mbar
- rate = 1.3 $\text{\AA}/\text{s}$

- Lift-off:

The samples are immersed in acetone to remove the resist. Now the samples are ready to measure.

C.2 In-situ samples

- FMI/NM deposition:

The CoFe_2O_4 is deposited in the same way as in the ex-situ samples. The only difference is that the Pt is also deposited in the same chamber, without exposing the CFO to air. The Pt is deposited in a sputter under the following conditions:

- $P_{base} = 1 \times 10^{-8}$ mbar
- $\text{Power}_{plasma} = 20$ W
- $P_{plasma} = 5 \times 10^{-3}$ mbar
- $T_{substrate} = 400^\circ\text{C}$
- rate = 3.57 $\text{\AA}/\text{s}$

These bilayers are grown in ICMAB in Barcelona.

- Spin coating:
 1. Spin coating of ma N-2403 negative resist at 6000 rpm for 30 seconds to obtain an homogeneous layer around 250 nm thick.
 2. Baking on the hot plate at 90°C for 60 seconds.
- eBL exposure: In this eBL exposure we pattern the Hall bar.
 - Acceleration voltage: 20 kV
 - Aperture: 10 μm
 - Write field: 100 \times 100 μm^2
 - Dose: 40 $\mu\text{C}/\text{cm}^2$
- Developing:

The sample is immersed in D-525 developer for 60 s and then rinsed in deionized water.
- Ar-ion milling:

An Ar-ion milling is needed to remove the Pt which is not protected under the negative resist.

 - $V_{beam} = 300 \text{ V}$
 - $I_{beam} = 50 \text{ mA}$
 - $V_{acceleration} = 50 \text{ V}$
 - $\alpha = 80^\circ$
 - milling rate = 8.4 nm/min

In this case the milling time varies depending on the Pt thickness (6.5 nm, 4 nm or 2 nm) that we want to mill.
- Lift-off:

The samples are immersed in acetone to remove the resist. Now the samples are ready to be measured.

List of publications

This thesis is based on the following publications:

1. *Spin transport enhancement by controlling the Ag growth in lateral spin valves*
Miren Isasa, Estitxu Villamor, Lorenzo Fallarino, Olatz Idigoras, Anna K. Suszka, Christopher Tollan, Andreas Berger, Luis E. Hueso and Felix Casanova, *J. Phys. D: Appl. Phys.* **48**, 215003 (2015).
(Chapter 4)
2. *Temperature dependence of spin diffusion length and spin Hall angle in Au and Pt*
Miren Isasa, Estitxu Villamor, Luis E. Hueso, Martin Gradhand and Felix Casanova, *Phys. Rev. B* **91**, 024402 (2015).
(Chapter 5)
3. *Detection and origin of inverse Rashba-Edelstein effect at Cu/Bi interface using lateral spin valves*
Miren Isasa, M. Carmen Martinez-Velarte, Estitxu Villamor, Cesar Magen, Luis Morellon, Jose M. De Teresa, M. Ricardo Ibarra, Giovanni Vignale, Evgueni V. Chulkov, Eugene E. Krasovskii, Luis E. Hueso and Felix Casanova, submitted to *Phys. Rev. Lett.*, *arXiv*: 1409.8540.
(Chapter 6)
4. *Spin Hall magnetoresistance at Pt/CoFe₂O₄ interfaces and texture effects*
Miren Isasa, Amilcar Bedoya-Pinto, Saül Velez, Federico Golmar, Florencio Sanchez, Luis E. Hueso, Josep Fontcuberta and Felix Casanova, *Appl. Phys. Lett.* **105**, 142402 (2014).
(Chapter 7)
5. *Spin Hall magnetoresistance as a probe for surface magnetization in Pt/CoFe₂O₄ bilayers*

Miren Isasa, Edurne Sagasta, Amilcar Bedoya-Pinto, Saül Velez, Florencio Sanchez, Nico Dix, Luis E. Hueso, Josep Fontcuberta and Felix Casanova, submitted to *Phys. Rev. Appl.*, *arXiv:1510.01449*
(Chapter 7)

Other publications:

1. *Contribution of defects to the spin relaxation in copper nano wires*
Estitxu Villamor, Miren Isasa, Luis E. Hueso and Felix Casanova, *Phys. Rev. B* **87**, 094417 (2013).
2. *Temperature dependence of spin polarization in ferromagnetic metals using lateral spin valves*
Estitxu Villamor, Miren Isasa, Luis E. Hueso and Felix Casanova, *Phys. Rev. B* **88**, 184411 (2013).
3. *Modulation of pure spin currents with a ferromagnetic insulator*
Estitxu Villamor, Miren Isasa, Saül Velez, Amilcar Bedoya-Pinto, Paolo Vavassori, Luis E. Hueso, F. Sebastian Bergeret and Felix Casanova, *Phys. Rev. B* **91**, 020403(R) (2015).
4. *Simultaneous detection of the spin-Hall magnetoresistance and the spin-Seebeck effect in platinum and tantalum on yttrium iron garnet*
Nynke Vlietstra, Juan Shan, Bart J. van Wees, Miren Isasa, Felix Casanova and J. Ben Youssef, *Phys. Rev. B* **90**, 174436 (2014).
5. *Hanle-Induced magnetoresistance in Pt thin films*
Saül Velez, Vitaly N. Golovach, Miren Isasa, Amilcar Bedoya-Pinto, Edurne Sagasta, Luca Pietrobon, Luis E. Hueso, F. Sebastian Bergeret, and Felix Casanova, *arXiv:1502.04624*.
6. *Searching for mantic proximity effects in magnetoresistive Pt/CoFe₂O₄ interfaces*
M. Valvidares, N. Dix, M. Isasa, K. Ollefs, F. Wilhelm, F. Sanchez, E. Pellegrin, A. Bedoya-Pinto, P. Gargiani, L. E. Hueso, F. Casanova and J. Fontcuberta, *arXiv:1510.01080*.

Acknowledgements

This thesis is the result of a journey I started four years ago. Although, I am the one reaching at the finishing line, I would like to take the opportunity to thank all the people that has supported me along the way.

First, I would like to express my deepest gratitude to my supervisor, Fèlix, who enthusiastically teach me all I know about spintronics. Your unlimited patience, your constant good mood and the ease to reach you make of you a great supervisor. I wish you all the best in the future with your research! Moltes gracies, benetan!

Luis Hueso also deserves a special mention, if you were not interviewed in the radio four years ago, now I was not writing this words. Thanks for introducing me to the research world and giving me the nice opportunity to join nanoGUNE. Thanks also for the many chances you gave me to present my work at international conferences where I learnt a lot and had so much fun.

My most sincere gratitude to Prof. Txema Pitarke for allowing me to carry out and complete my education in nanoGUNE. I also acknowledge the financial support from the Basque Government during my PhD.

I would like to thank all the former and present members of the nanodevices group, for contributing to such a nice working atmosphere and for being always ready to help. My special thanks to *Angels + 1*. Estitxu you have been a good teacher and a better team mate, Oihana (my twin *nanobaby*) it was a pleasure being always so close to you and Edurne you have been like fresh air at the end. Neskak ez dakit Felix edo Xiangnanen aingeruak izan garen, baina argi dut zuek behientzat nire aingeruak izan zaretela! Mila esker benetan! This group of course is nothing without you Roger! You have saved my day or at least my research on numerous occasions over these years. Thank you so much for being always ready to help, for opening once and again the

Createc, for your unconditional help and advice with blender... and for all the work you make always with a smile in your face and with so many jokes that makes even cleanroom a nice place!

Speaking about cleanroom I cannot forget about Ralph. Thanks for teaching me all the lithography tricks, for coming with me to the eBL when my skills were "oxidized" or for showing me all these routes in the mountains of Gipuzkoa in Google Earth!

Speacial thanks also to the people in nanomag. Not only we have a nice collaboration (and many other ideas!) but we had great time in all the conferences we went.

In general, I want to thank all the nanopeople in the *hamaiketako* and at lunch time because your old and new stories, your jokes and your good humor is what makes of nanoGUNE such a nice place to work! Eskerrik asko!

Besides nanoGUNE, I am very grateful to some other people. First, to Pep and Florencio, the people in Zaragoza, Martin, Giovanni, Eugene and Evgueni, each of you have contributed to enrich the work I am showing here. Of course I cannot forget the people from Groningen, Martijn, Roald, Nynke, Juan, Kumar, Ewout, Saurabh, Joost.. The borrels, the Christmas dinner and Sinterklaas made me fill as if I was one more in the FND group! My special thanks to Charly, for making of Groningen such a sweet city! Last, I am extremely thankful to Laurent Vila and Martin Gradhand who undoubtedly accepted reading the thesis and giving me their feedback for the international PhD mention.

Etxera itzuliz nire eskerrik beroena kuadrilakoei, askotan zertan nabilen jakin gabe ere emandako animo inkondizionalagatik!

Nola ez, aita, ama, Inge, Iñigo eta Ierari. Ez duelako importa itsaso barea edo zakarra dagoen, korrontea alde ala kontra daukagun, badakit beti batera arraun egingo degula. Mila esker, bihotzez!

Eta amaitzeko, daukazun pazientzia guztiagatik, momenturik zailenetan ere nere barrea eragiten jakiteagatik eta idatzi ezin den dana izateagatik, eskerrik asko Paulo.

Miren Isasa

Donostian, 2015eko urrian